DESIGN, SIMULATION AND DEVELOPMENT OF MICROELECTRONIC DEVICES AND MATERIALS FOR H_2S SENSING APPLICATIONS

By

K.G. GIRIJA

Enrol. No. : ENGG01201304049

Bhabha Atomic Research Centre, Mumbai

A thesis submitted to the

Board of Studies in Engineering Sciences

In partial fulfillment of requirements

for the Degree of

DOCTOR OF PHILOSOPHY

of

HOMI BHABHA NATIONAL INSTITUTE

June, 2019

Homi Bhabha National Institute

Recommendations of the Viva Voce Committee

As members of the Viva Voce Committee, we certify that we have read the dissertation prepared by **Smt. K.G. Girija** entitled "**Design, Simulation and Development of Microelectronic Devices and Materials for H_2S Sensing Applications**" and recommend that it may be accepted as fulfilling the thesis requirement for the award of Degree of Doctor of Philosophy.

Chairman – Dr. Archana Sharma	Archana	**Date:**	21-6-19
Guide / Convener – Dr. Anita Topkar		**Date:**	21/6/19
Co-guide - Dr. R.K. Vatsa		**Date:**	21/6/2019
Examiner – Prof. Prem Pal	Prem Pal	**Date:**	21-6-2019
Member 1- Dr. Gopika Vinod		**Date:**	21/6/2019
Member 2- Dr. V. H. Patankar	V.H.	**Date:**	21.06.19
Member 3- Dr. B. Dikshit	B Dikshit	**Date:**	21/6/19
Invitee – Dr. C.A. Betty	Betty	**Date:**	21/06/2019

Final approval and acceptance of this thesis is contingent upon the candidate's submission of the final copies of the thesis to HBNI.

We hereby certify that we have read this thesis prepared under our direction and recommend that it may be accepted as fulfilling the thesis requirement.

Date: 21/6/19
Place: BARC, Trombay

Guide
Dr. Anita Topkar

Co-guide
Dr. R.K. Vatsa

STATEMENT BY AUTHOR

This dissertation has been submitted in partial fulfillment of requirements for an advanced degree at Homi Bhabha National Institute (HBNI) and is deposited in the Library to be made available to borrowers under rules of the HBNI.

Brief quotations from this dissertation are allowable without special permission, provided that accurate acknowledgement of source is made. Requests for permission for extended quotation from or reproduction of this manuscript in whole or in part may be granted by the Competent Authority of HBNI when in his or her judgment the proposed use of the material is in the interests of scholarship. In all other instances, however, permission must be obtained from the author.

K.G. Girija

DECLARATION

I, hereby declare that the investigation presented in the thesis has been carried out by me. The work is original and has not been submitted earlier as a whole or in part for a degree / diploma at this or any other Institution / University.

K.G. Girija

List of Publications arising from the thesis

Journals

1. "Enhanced H_2S sensing properties of Gallium doped ZnO nanocrystalline films as investigated by DC conductivity and impedance spectroscopy", K.G. Girija, K. Somasundaram, A.K. Debnath A. Topkar and R.K. Vatsa, *J. Mater. Chem. Phys.*, **2018,** *214*, 297 – 305.

2. "Low-cost surface micromachined microhotplates for chemiresistive gas sensors", K.G. Girija, S. Chakraborty, M. Menaka, R.K. Vatsa and A. Topkar, *Microsyst. Technol.*, **2018,** *24*, 3291 – 3297.

3. "Design, simulation and fabrication of piezoresistive microcantilevers using standard multi user MEMS process", K.G. Girija, Indu Tushir, R.K. Vatsa and A. Topkar, *ISSS J. Micro Smart Syst.*, **2017**, *6*, 83 - 89.

4. "Highly selective H_2S gas sensor based on Cu-doped ZnO nanocrystalline films deposited by RF magnetron sputtering of powder target", K.G. Girija, K. Somasundaram, A. Topkar and R.K. Vatsa, *J. Alloys compd.*, **2016,** *684*, 15 - 20.

Conferences

1. "H_2S sensing properties of ZnO:N thin films prepared by RF magnetron sputtering", K.G. Girija, Abith Murali, R.K. Vatsa and A. Topkar, Conf. on Mater. & Technol. for Energy Conversion and Storage, DAE Convention Centre, Anushakthi Nagar, Mumbai, **2018**, 42.

2. "Modeling, design and simulation of piezoresistive microcantilevers using standard multi user MEMS Process", K.G. Girija, Indu Tushir, V. Belwanshi, R.K. Vatsa and A. Topkar, Int. Symp. Phys and Tech of Sensors (ISPTS-2), CMET, Pune, **2015,** 129 - 130.

3. "Design and electro-thermal analysis of micro hotplates for chemical sensors using standard multi user MEMS process", K.G. Girija, D. Kaur, V. Belwanshi, J. Mehta, R.K. Vatsa and A. Topkar, IEEE Xplore Proc., Int. Symp. Phys. & Tech. Sensors (ISPTS-2), CMET, Pune, **2015**, 7220075, 27 - 29.

K.G.Girija

DEDICATED

TO MY FAMILY

ACKNOWLEDGEMENTS

I take this opportunity to sincerely thank all the people who have been instrumental in the successful completion of this thesis work. First and foremost, I am grateful to the Almighty God for his guidance and blessings throughout the course of the research work.

Words are not enough to thank my guide Dr. Anita Topkar who gave me the opportunity to rejuvenate my passion for microelectronics. Her valuable suggestions, constructive criticisms and constant support have shaped and fine tuned this research work.

I am truly grateful to my co-guide Dr. R.K. Vatsa without whose support I couldn’t have registered for PhD. He always believed in me, supported my endeavours and gave me complete freedom in doing the work.

I express my heartfelt gratitude to Dr. C.A. Betty for her unconditional support, constant encouragement and useful discussions.

I would like to thank my doctoral committee members - Dr. Archana Sharma, Dr. Gopika Vinod, Dr. V.H. Patankar and Dr. B. Dikshit – for periodic evaluation of the progress of my Ph.D work, important suggestions during the research period and for conducting the final viva voce. I owe my special thanks to Dr. Archana Sharma, who consistently motivated me for completing the research work.

I acknowledge my students – Somasundaram, Shaheera and Abith for their help in synthesis. I owe a lot to Somasundaram, who was always ready to help especially during the optimization of sputtering process.

Without the help of Indu, Daman and Vinod, I couldn’t have been successful in the design and simulation of microstructures. My special thanks to Vinod for always helping out with the FEM simulations. I sincerely acknowledge Arvind Kumar, Soumyajit, Sebin and Bharati for their help during the characterization of microstructures.

I am grateful to Prof. R.O. Dussane, IITB and Prof. Mandar Deshmukh, TIFR for allowing me to use their wirebonding facilities. I am also thankful to Head, QAD and Smt. Menaka, IGCAR for their help in IR imaging.

I couldn't have completed this doctoral work without the encouragement, motivation and emotional support from my dear friends Betty, Sasikala, Dhanya, Pushpa, Sulekha, Shashikala and Padma. They were always there to share my ups and downs during the course of this work.

I thank my colleagues Mishra, Manimaran, Jayakumar, Sudarsan and my workshop colleagues for extending support and help at various stages of the thesis work. I also thank all my well - wishers and friends who have directly or indirectly helped me.

Last but not the least, I am sincerely grateful to my all family members, especially my husband, Sankaran for his unconditional support and great patience during this dissertation work. And I thank my loving son Karthik, who was always amused at the thought of his mother doing PhD.

CONTENTS

SYNOPSIS

Due to stringent safety regulations worldwide, there is an ever increasing demand for inexpensive, reliable and portable gas sensors for the detection of hazardous and toxic gases such as CO, NO_x, H_2S, NH_3, SO_2, etc. Solid State sensors based on metal oxides (MOX) present great advantages in this respect due to their small size, low cost, low-power consumption and compatibility with microelectronic processing. Chemical modulation of the surface conductivity is the basic principle of operation of MOX gas sensors. In order to improve the selectivity, response time and reversibility, MOX sensors are usually operated in the temperature range of 200 °C - 600 °C, which leads to increased power consumption of the sensor system. Reducing the power consumption is one of the prime objectives for a sensor system to achieve acceptable battery lifetime, especially for portable and field applications. Micro Electro Mechanical System (MEMS) based technology offers benefits like reduced thermal mass, miniaturization, low power consumption, reproducibility and low unit cost. The motivation behind this thesis work was to develop microelectronic devices and highly selective metal oxide materials using CMOS compatible post processing methods for realizing hydrogen sulphide (H_2S) sensors.

Zinc Oxide (ZnO) was chosen as the sensing material for realizing H_2S sensors as it is one of the most promising gas sensor materials owing to its easy synthesis procedure, good electrical properties and compatibility with silicon, leading to MEMS based chemical sensors. Multi User MEMS Process (MUMPs) was adapted for the design and fabrication of the MEMS structures. Based on this process, design and simulations studies were carried out on various types of microhotplates (MHP) and microcantilevers using commercial Finite Element Simulations (FEM) software. Based on the simulation results the design of the microstructures was optimized and these were subsequently fabricated. Optical Microscopy, Scanning Electron Microscopy and White Light Interference measurements on the fabricated microstructures verified that the geometries matched very well with the designed X-Y-Z dimensions. Thermal imaging by IR camera confirmed temperature homogeneity of the suspended membrane of MHP (300 µm × 300 µm) and the thermal efficiency of the MHPs was experimentally estimated as ~10 °C / mW.

Undoped and doped (Cu, Ga and N_2) ZnO films were synthesized in a customized RF magnetron sputtering system using powder targets. XRD studies confirmed the hexagonal wurtzite crystal structure with a strong Bragg reflection corresponding to (002) orientation for all the films. AFM showed fully coalesced, uniformly distributed columnar ZnO grains for all the films. XPS measurements confirmed the existence of +2 oxidation valence state of Cu in CZO (Cu doped ZnO) films, +3 in case of GZO (Ga doped ZnO) films and formation of N-Zn bonds in NZO (N doped ZnO) films. O 1s spectra showed enhancement in the number of oxygen vacancies for all doped films. Gas sensors were fabricated by depositing interdigitated gold electrodes on the sputtered films by thermal evaporation. Gas sensing studies were carried out in a home-made automated gas sensing setup by measuring the conductance of the films with time as a function of temperature and gas concentration. Gas sensitivity, S, was computed as the % change in conductance when the sensor is exposed to air and H_2S. It was observed that among the doped films, 2% CZO gave the highest sensitivity (70% for 5 ppm) at an operating temperature of 250 °C, while 3% GZO and NZO exhibited the highest sensitivity (200% and 1200% respectively for 5 ppm) for H_2S at 300 °C. All the sensors showed high selectivity towards H_2S with fast response (< 50 s) and recovery (< 200 s) characteristics. It was observed that among the three doped systems, GZO showed the optimum sensor performance in terms of sensitivity, response time and stability.

The important contributions of this thesis work are summarized below:

(i) Design, simulation, fabrication and characterization of MetalMUMPs based MHPs and microcantilevers were carried out for gas sensor applications.

(ii) Structural and optical characterizations confirmed that the geometry for all the structures was as per the design. Electro-thermal characterisations of the smallest MHP affirmed the temperature homogeneity of the suspended membrane and the thermal efficiency was estimated as ~ 10 ºC / mW.

(iii) Deposition of highly oriented, nanocrystalline films of undoped and doped ZnO films could be achieved by RF magnetron sputtering technique using powder targets.

(iv) While all three doped systems (CZO, GZO and NZO) exhibited high sensitivity and selectivity towards H_2S, GZO showed the optimum sensor performance with respect to sensitivity, speed and stability.

LIST OF FIGURES

LIST OF TABLES

LIST OF FREQUENTLY USED ABBREVIATIONS

AFM	Atomic Force Microscopy
CCD	Charge Coupled Device
CMOS	Complementary Metal Oxide Semiconductor
CVD	Chemical Vapor Deposition
CZO	Cu doped ZnO
EDX	Energy Dispersive X-ray
FEM	Finite Element Method
FWHM	Full Width Half Maximum
GZO	Gallium Doped ZnO
HMI	Human Machine Interface
IDE	Inter Digitated Electrodes
IDLH	Immediately Dangerous to Life or Health
IR	Infra Red
KOH	Potassium Hydroxide
LEL	Lower Explosive Limit
MEMS	Micro Electro Mechanical Systems
MFC	Mass Flow Controller
MHP	Micro Hot Plate
MOX	Metal Oxide
MPW	Multi Product Wafer
MUMPs	Multi User MEMS processes
NIOSH	National Institute of Occupational Safety and Health

NZO	Nitrogen doped ZnO
OSHA	Occupational Safety and Health Administration
PCB	Printed Circuit Board
PEL	Permissible Exposure Limit
PLC	Programmable Logic Controller
PMS	Pulsed Magnetron Sputtering
PVD	Physical Vapor Deposition
REL	Recommended Exposure Limit
SAW	Surface Acoustic Wave
SEM	Scanning Electron Microscope
STEL	Short Term Exposure Limit
TCR	Temperature Co-efficient of Resistance
TWA	Time Weighted Average
UEL	Upper Explosive Limit
VOC	Volatile Organic Compounds
WLI	White Light Interferometer
XPS	X-ray Photoelectron Spectroscopy
XRD	X-ray diffraction
ZnO	Zinc Oxide

CHAPTER 1: INTRODUCTION

1.1 Introduction

Gas sensor technology has become more significant in many important areas such as environmental monitoring for toxic and hazardous gases, safety and public security (explosives, explosive gases/compounds), industrial and automotive applications (process control, exhaust emission), disease diagnosis in human health sector, etc. Typical gases of interest for such applications include CO, NO_x, H_2S, NH_3, SO_2, CO_2, CH_4 and other hydrocarbons. These gases adversely affect human health, if present beyond a threshold concentration. Gas sensors were first primarily used in coal mines, where continuous monitoring of hazardous gases is essential. With the advent in gas sensor technology, these sensors are widely used in automobile, chemical and petrochemical industries, agriculture and food processing sectors, environmental monitoring, hospitals, scientific and engineering research laboratories, semiconductor manufacturing, telecommunications and a variety of other applications.

Owing to the myriad applications, the demand is ever growing that necessitates the development of miniaturized, robust and cost-effective gas sensors with high selectivity as well as sensitivity and stability. Solid State sensors present great advantages in this respect due to their small size, low cost and relative simplicity. Among various solid state sensor technologies, chemiresistive sensors, based on metal oxides (MOX) are best suited for portable sensors and compact sensor arrays because of their simple transduction mechanism and readout interface circuit. Metal oxides have been used nearly for four decades for gas sensing applications. The fundamental principle behind the gas sensing mechanism by metal oxides is the change in their electrical conductivity due to the reaction between adsorbed oxygen and the analyte gas. Global companies like Figaro Engineering, Applied Sensors, Membrapor AG, General Monitors and UST offer semiconducting metal oxide gas sensors for various applications such as explosive gas alarms, monitoring of toxic gases concentrations, industrial process control, automotive cabin air intake and so on. Due to rising number of industries worldwide and the environmental concerns regarding air quality, the demand for affordable gas sensors will always remain strong and significantly bolster the market growth.

1.2 Objective of the work

The impetus of this thesis work is to develop highly selective materials using Complementary Metal Oxide Semiconductor (CMOS) compatible post processing methods for realizing microelectronic devices based H_2S sensors. It is well known that H_2S is a highly toxic and flammable gas and its exposure adversely affects human health even at low concentrations. Hence it is important to monitor H_2S using highly selective and sensitive sensors wherever it is encountered. Over the past few decades, a great deal of research effort has been directed towards the miniaturization of the sensors and integration of electronics for practical applications, ranging from toxic gas detection to manufacturing process monitoring. Among the solid state gas sensors, metal oxide (MOX) based sensors are the best candidates for miniaturization since they are cost effective, easy to fabricate, compatible with silicon technology and have the ability to detect a broad range of gases.

The main objective of this research work is to develop and study Microelectronic Devices and Materials for H_2S Sensing Applications. This involves:

a) Design and simulation of appropriate device structures such as microhotplates, microcantilevers, etc.

b) Fabrication of designed structures and characterization of the structures.

c) Deposition and characterization of suitable MOX materials on suitable substrates to fabricate thin film gas sensors.

d) Evaluation of sensor parameters such as sensitivity, specificity, stability, temperature response, etc., in a gas sensor testing setup.

1.3 Structure of the report

The research work carried out for the present doctoral thesis is summarized in the following chapters. Chapter 2 gives a review on the literature survey of solid state gas sensors, MOX for gas sensing, Micro Electro Mechanical Systems (MEMS) structures for gas sensors, Multi-User MEMS Process (MUMPs) which is adapted for fabrication and the Finite Element Method (FEM) software used for simulation studies. Chapter 3 elaborates on the design and simulation studies on microhotplates and microcantilevers. Electro-thermal, thermo-mechanical and piezo electric simulations results of various micro structures are discussed. Chapter 4 focuses on the fabrication and characterization of microstructures. Optical microscopy, surface topography, IR thermal imaging results are presented in this Chapter. Chapter 5 outlines the deposition and characterization of metal oxide films. Installation and process optimization of RF magnetron sputtering and thermal evaporation systems are described in this Chapter. Synthesis and material characterization of doped ZnO films are summarized in Chapter 6. Chapter 7 compiles the H_2S sensing studies on doped ZnO films. Comparison of various dopants on the gas sensing properties is also discussed in this Chapter. Chapter 8 concludes the report and discusses the future scope of the research work.

CHAPTER 2: LITERATURE SURVEY

Metal oxide (MOX) based gas sensor are widely used for a variety of applications due to their numerous advantages, like small size, high sensitivity (ppm / ppb) to a wide range of gases, low cost, etc. To facilitate portable and field applications, a great deal of research is directed towards the miniaturization of MOX based sensors. In this context, MEMS based technology offers benefits like miniaturization, low power consumption, reproducibility etc. This chapter gives the literature survey of various topics involved in the thesis work, which include a brief review of solid-state gas sensor technologies, detailed discussion on MOX based gas sensors, a survey of MEMS based structures for MOX sensors and an overview of the MUMPs process and MEMS design tool.

2.1 Solid state gas sensors

2.1.1 Introduction

Rapid developments in science and technology in the recent decades have elevated our living standards. However, these great developments also led to a host of environmental problems which have increased worldwide environmental concerns. Gaseous pollutants released from industries and automobiles can lead to human health issues, acid rain, ozone depletion and the greenhouse effect. Thus reliable detection of flammable, hazardous and toxic gases has become a major issue worldwide due to more stringent safety regulations [1-4]. The requirements of gas monitoring systems can be broadly classified in to the following four categories:

(i) Oxygen monitoring for health and industries viz. mining, hospitals, etc.

(ii) Inflammable gases like methane, LPG, hydrogen monitoring etc., to prevent accidents.

(iii) Monitoring of toxic gases (CO, H_2S, NH_3, Cl, etc.) and automobile exhaust pollutants like SO_x, NO_x, etc.

(iv) Relative humidity monitoring which is an important parameter in weather monitoring and climate control. In addition, it affects the sensing parameters of gas sensors.

Table 2.1 shows the environmental safety standards for some important Volatile Organic Compounds (VOC) and pollutant gases. It is imperative that these gases must be detected in ppm levels in air by selective and sensitive sensors, especially when they are encountered in the presence of other gases, usually prevalent in industrial and environmental situations. Spectroscopic methods are employed in the detection and identification of gases, where precise quantification and control are required. In these methods, samples are taken from air and fed into the spectrometer, where they are ionized. The resultant ions are separated via electrical and magnetic fields according to their mass-charge ratio and are subsequently detected and quantified. These spectroscopic methods include Ion mobility, Raman, Infra-red, Terahertz spectroscopic systems, etc. They are typically highly selective and sensitive, but suffer from high turnover rates, large equipment and operating costs and low portability. Environmental monitoring for toxic and hazardous gases, safety and public security, indoor air quality monitoring, etc., cannot afford such expensive and bulky systems. Moreover, these systems require sample preparation because of which on-line monitoring or real-time analysis is difficult. Hence, there is an ever increasing demand for portable, inexpensive, accurate, and reliable gas

Table 2.1. Environmental safety standards for toxic gases and VOC vapors [5].

Gas/Vapor	**NIOSH**	**OSHA**	**IDLH**	**Properties**
Benzene (C_6H_6)	0.1 ppm (REL) 1 ppm (STEL)	1 ppm 5 ppm (STEL)	500 ppm	Colorless liquid, easily vaporized, dissolves fats
Ethanol (C_2H_5OH)	1000 ppm (REL)	1000 ppm	3300 ppm	Ordinary alcohol as in wine
Methane (CH_4)	90000 ppm (9%)	90000 ppm (9%)	—	Component of natural gas. Gas causing mine explosions
Methanol (CH_3OH)	200 ppm (REL) 250 ppm (STEL)	200 ppm	6000 ppm	An important organic solvent
Propanol (C_3H_7OH)	200 ppm (REL) 250 ppm (STEL)	200 ppm	800 ppm	Alcohol. Clear colorless liquid
Ammonia (NH_3)	25 ppm (REL) 35 ppm (STEL)	50ppm (PEL)	300 ppm	A colorless gas having a pungent odor
Carbon dioxide (CO_2)	5000 ppm (REL) 3% (STEL)	5000 ppm (PEL)	30000 ppm (3%)	Nonflammable, colorless, odorless, slightly acid gas
Carbon monoxide (CO)	35 ppm (REL) 200 ppm (ceiling)	50 ppm (PEL)	1200 ppm	Toxic, flammable, colorless, and odorless gas
Hydrogen sulfide (H_2S)	10 ppm (ceiling) for 10min	20 ppm (ceiling) 50 ppm (10min)	100 ppm	Colorless, highly flammable, offensive odor (rotten eggs)
Nitrogen compounds (NO, NO_2, NO_x)	25 ppm (REL)	25 ppm (PEL)	100 ppm	NO, N_2O_3, NO_2 (N_2O_4) are extremely toxic gases
Sulfur dioxide (SO_2)	2 ppm (REL) 5 ppm (STEL)	5 ppm (STEL)	100 ppm	Highly irritating, Non-flammable, colorless gas

VOC - Volatile Organic Compounds; REL - Recommended Exposure Limit; STEL - Short-Term Exposure Limit; PEL - Permissible Exposure Limit; IDLH - Immediately Dangerous to Life or Health; NIOSH - National Institute of Occupational Safety and Health; OSHA - Occupational Safety and Health Administration.

sensors that can detect low concentration of gases of interest. Solid State sensors present great advantages in this respect due to their fast sensing response, low cost, low power consumption and small size. In addition, solid state sensors have the capability of performing continuous, real-time environmental monitoring and require fewer resources to manufacture, operate and maintain

[6, 7]. Due to their small size, multiple sensors can also be networked and operated simultaneously to scan for several analytes at a time, with the feasibility of making a portable system.

2.1.2 Characteristics of gas sensors

In order to characterize a gas sensor performance, a set of parameters is used [8]. The most important parameters and their definitions are listed below:

(i) *Sensitivity* is the magnitude of change of measured signal with respect to analyte concentration, i.e., the slope of a calibration graph. It refers to the ability of the sensor to detect the desired chemical species in the range of interest.

(ii) *Selectivity* of the sensor refers to the detection of the species of interest in the presence of other interfering gases, which also can produce a sensor response.

(iii) *Speed (Response time)* is the time required for a sensor to respond to a step concentration change from zero to a certain concentration value, often defined as 90% of the steady-state signal.

(iv) *Stability* refers to the degree to which the sensor response and baseline to a given environment drift with time. It is a measure of the ability of a sensor to provide reproducible data during the sensor's lifetime. This includes retaining the response and recovery times, sensitivity and selectivity.

(v) *Detection limit* is the lowest concentration of the analyte that can be reliably detected by the sensor.

(vi) *Dynamic range* is the analyte concentration range between the lowest detection limit and the concentration above which the sensor response saturates.

(vii) *Linearity* is the relative deviation of the experimental data from an ideal straight line.

(viii) *Resolution* is the lowest concentration difference of the analyte gas that can be discerned by the sensor.

(ix) *Recovery time* is the time the sensor signal takes to return to its initial value after the removal of analyte gas.

(x) *Working temperature* is usually the temperature at which maximum sensitivity for the analyte gas is achieved.

All these parameters are used to characterize the properties of a particular material or sensor. In the above list, the first four parameters —sensitivity, selectivity, speed and stability – often referred as *4S* parameters, determine the figure of merit of any gas sensor. An ideal gas sensor should possess high sensitivity, selectivity and stability; low detection limit; wide dynamic range and linearity; small hysteresis and response time. It is often impossible to achieve ideal sensor characteristics. Efforts are usually made to optimize the sensor parameters, depending on the application.

2.1.3 Gas sensor classification

According to the International Union of Pure and Applied Chemistry (IUPAC), a *gas sensor* is a device that can detect and signal the presence and / or quantify the concentration of a family of chemicals or a specific chemical to which the sensor is exposed. In other words, gas sensors are devices which convert a change in chemical state into an electrical signal. Depending on the transduction mechanism, solid state gas sensors can be broadly classified as [9]:

(i) Mass-sensitive gas sensors

(ii) Calorimetric or catalytic gas sensors

(iii) Optical gas sensors

(iv) Electrochemical gas sensors

(v) Chemiresistive or conductometric gas sensors

A brief description of each class of sensor is given below.

Mass-sensitive gas sensors are the simplest form of gravimetric sensors that respond to the mass of species attached to the sensing layer. In principle, any species that can be immobilized on the sensor surface can be detected. The mass changes can be monitored by either (i) deflecting a micromechanical structure due to stress changes or (ii) by evaluating the frequency characteristics of a resonating structure or a travelling acoustic wave upon mass loading. The sensitivity and selectivity of mass-sensitive gas sensors for the detection of particular analyte molecules are dependent on chemical sensing layer on the active surface. Surface acoustic wave (SAW) based sensors, Quartz crystal microbalance and microcantilever based devices are the most commonly used mass sensors [10].

Calorimetric sensors are widely known as “catalytic beads” or “pellistors” and can sense all combustible gases like ammonia, hydrocarbons, etc. The pellet or bead is coated with a suitable catalyst layer, which is heated by passing a current through the embedded platinum coil. In the presence of a flammable gas or vapour, the heated catalyst layer facilitates oxidation to occur in a chemical reaction similar to combustion. This catalytic reaction releases heat, thereby raising the temperature of the catalytic bead and the underlying platinum coil. This rise in temperature results in a change in the electrical resistance of the coil, which in turn is measured as the signal from the sensor. Major advantages of catalytic sensors are that they are stable, reliable, rugged, and have a long operating life [11].

Optical gas sensors detect the changes in optical phenomena that result from an interaction of the analyte with the sensor. These may exploit either linear optical phenomena such as absorption, fluorescence, phosphorescence, polarization, rotation, interference, etc., or non-linear phenomena, such as second harmonic generation. The choice of a particular optical method depends on the nature of the application and desired sensitivities. Most optical sensors are based on fiber optic technology, which are also known as optodes. These sensors offer immunity to electromagnetic interference, high selectivity and safety while working with flammable and explosive compounds. However, optical sensors suffer from ambient light interference with their operation and their long-term stability is limited due to indicator leaching or photobleaching. Also the detection system for optical sensors is complex and expensive. [12].

Electrochemical sensors constitute one of the largest and most developed groups of chemical sensors and have taken a leading position with respect to commercialization in the fields of industrial, clinical and environmental applications. Basically, electrochemical sensors produce an electrical signal proportional to the gas concentration due to the oxidation / reduction reaction with the gas of interest. Most electrochemical gas sensors are amperometric sensors, which generate a current that is linearly proportional to the gas concentration. Electrochemical sensors are accurate, require low power and mostly used for toxic gas detection. However, these sensors are relatively expensive and also suffer a short life span [13].

As the name implies, *chemiresistive sensors* measure the change in conductivity due to the interaction between the thin film surface and the target analyte molecules. Semiconducting metal oxides have emerged as the most common, diverse and probably, largest class of sensor materials due to their extensive structural, physical and chemical properties and functionalities. The most common metal oxides utilized as sensing layer in chemiresistive sensors are binary oxides such as SnO_2, ZnO, TiO_2, etc.; however, ternary and more complex oxides are also used in practical gas sensors [14]. The reactions at the heated MOX surface influence the concentration of electrons in the MOX film depletion layer, which in turn changes the conductance of these devices as a function of gas concentration. Metal oxide based sensors have been widely studied in literature and exploited at industries, laboratories and public places owing to their high sensitivity to a broad range of chemical compounds, the low cost methods of fabrication and the compatibility with silicon technology [15].

In the last fifty years, the field of solid gas sensors has seen a significant expansion and became one of the most sought-after research areas within the sensor community. The demand for high performance gas sensors with high sensitivity and selectivity, faster response, together with low power consumption and high device reliability, has generated intensive research efforts to improve the sensing characteristics.

The ccomparison of various solid state gas sensing technologies discussed above is given in Table 2.2. As can be seen, each type of sensor has its own merits and demerits. Therefore, while designing gas sensors, the requirements are chosen according to the planned application. For example, good sensitivity, high reliability, a low false-alarm rate and adequate long-term stability are the important parameters for industrial sensor users, whereas the size and cost of sensors are not crucial. Resistance to gamma / X - ray radiation during sterilization, drift-free performance and cost are the most essential requirements for disposable sensors in medical applications. Environmental monitoring in public places, industries etc., requires monitoring of

Table 2.2. Comparison of various solid state gas sensing technologies.

S. no.	Sensor type	Advantages	Disadvantages
1.	Electrochemical	Ambient temperature operation, low power consumption, very sensitive to various VOCs	Bulky size, poor sensitivity to simple or low molecular weight gases
2.	Mass sensitive	Good precision, diverse range of sensor coatings, high sensitivity, sensitive to virtually all gases	Complex circuitry, poor signal-to-noise ratio, sensitive to humidity and temperature
3.	Optical sensors	Very high sensitivity, quantification of individual compounds in mixtures, multi-parameter detection capabilities	Complex sensor-array systems, expensive, low portability due to delicate optics and electrical components
4.	Calorimetric or catalytic bead (CB)	Fast response and recovery time, high specificity for oxidizing compounds	High-temperature operation, sensitive only to oxygen-containing compounds
5.	Chemiresistive metal oxide	High sensitivity to wide range of gases, fast response and recovery times, low cost, ideal for integrated sensor and electronics	High-temperature operation, moderate selectivity, susceptible to humidity

toxic components under the conditions of constantly changing humidity and temperature with high sensitivity, though the response time is not an essential requirement. The demands for selectivity and sensitivity are very high for explosive detection. In case of improvised explosives, detection limit of the order of sub-ppb is required together with high selectivity in order to avoid false alarms. Thus, in practical applications, the parameters of an ideal gas sensor are often appraised differently depending on the application. Table 2.3 gives a list of commonly encountered toxic and flammable gases with their exposure limits (TWA and STEL) and the requirements such as sensitivity, response time, recovery time, detection limit, dynamic range, life cycle and preferred sensor type for each gas.

As seen from the table, electrochemical sensors are more commonly deployed for toxic gas detection, especially for the concentration level of the order of few tenths of ppm. Mass sensitive and optical sensors find applications, where sensitivity and selectivity are of importance. Catalytic sensors are ideal for flammable gases such as hydrogen, methane, etc., where % concentration sets the Lower Explosive Limit (LEL) and Upper Explosive Limit (UEL). Undoubtedly, MOX sensor dominates the application choice as they are suitable for almost all type of gases as listed in Table 2.3. Although chemiresistive sensors have poor selectivity, their low cost and fabrication simplicity are the main factors contributing to their widespread use. Specifically, MOX sensors are the simplest of the chemical sensor technologies available for miniaturization in field and portable instruments. The rapid growth of materials chemistry has made available a variety of new sensing materials for the development of high performance MOX sensors [16].

Table 2.3. Detection requirements for various toxic and flammable gases.

S. No.	Gas	TWA (8hrs), ppm	STEL (15min.) ppm	Sensitivity % change in conductance	Response time, s	Recovery time, min	Detection limit, ppm	Dynamic range, ppm	Resolution ppm	Life cycle, years	Sensor type preferred
1.	H_2S	10	15	10 – 100 (for 5 ppm)	< 10	1 – 5	0.5 – 5	0 – 25	1	2-5	Electrochemical, chemiresistive (MOX), optical
2.	CO	50	300	10 – 20 (for 10 ppm)	<50	<10	10 - 20	0 - 500	5 - 10	>3	Electrochemical, chemiresistive (MOX)
3.	NO_2	3	5	20 - 200 (for 1 ppm)	<10	1 – 5	0.2 – 1	0 – 10	0.1 – 0.5	2 - 5	Electrochemical, chemiresistive (MOX), mass sensitive, optical
4.	SO_2	2	5	20 - 200 (for 1 ppm)	<10	1 – 5	0.2 – 1	0 – 10	0.1 – 0.5	2 - 5	Electrochemical, chemiresistive (MOX), mass sensitive
5.	PH_3	–	0.3	20 - 200 (for 0.1 ppm)	<5	1 – 5	0.05 – 0.1	0 – 5	0.05	>2	Electrochemical, chemiresistive (MOX), mass sensitive, optical
6.	CH_3OH	200	250	20 - 100 (for 50 ppm)	20 - 100	5 – 15	20 - 50	0 – 500	20 - 50	2 - 5	chemiresistive (MOX), mass sensitive
7.	Cl_2	0.5	1	20 - 100 (for 0.1 ppm)	<5	1 – 5	0.05 – 0.1	0 – 5	0.05	>2	Electrochemical, chemiresistive (MOX), mass sensitive
8.	NH_3	25	35	10 – 100 (for 10 ppm)	< 10	1 – 5	1 – 5	0 – 50	2 - 5	2-5	chemiresistive (MOX), mass sensitive
9.	HCl	–	5	10 - 50 (for 1 ppm)	<10	1 – 5	0.2 – 1	0 – 10	0.1 – 0.5	>2	Electrochemical, chemiresistive (MOX)
10.	H_2	4%LEL	75% UEL	10 – 50 (for 1%)	5 – 25	1 – 5	0.1 – 0.5%	0 – 100%	0.1 – 0.5%	2 - 3	Catalytic, chemiresistive (MOX)
11.	CH_4	5%LEL	15% UEL	10 – 50 (for 1%)	<10	1 – 5	0.1 – 0.5%	0 – 25%	0.1 – 0.5%	2 - 3	Catalytic, chemiresistive (MOX)

TWA – Time weighted average; STEL – Short term exposure limit; LEL – Lower explosive limit; UEL – Upper explosive limit

2.2 Metal oxides for gas sensing

Gas sensing effect on metal oxides was first demonstrated by Seiyama *et al.* in 1962 [17], which was later marketed by Taguchi using an alumina ceramic tube mounted with thick metal oxide, heater and electrodes [18]. In the last few decades, due to their simplicity, low cost, small size and ability to be integrated into electronic devices, MOX sensors have dominated the gas sensing applications, including environmental monitoring, industrial emission control, household security, automobile, agriculture and biomedical industries, etc.

Among the popular metal oxides, SnO_2, ZnO, TiO_2 and WO_3 are n-type semiconductors, while CuO and Cr_2O_3 are p-type semiconductors. Fig. 2.1 shows the studies on metal oxides in terms of usage as gas sensor materials [19]. The n-type semiconductors show increase in conductivity when exposed to reducing gases (the gases deliver electrons to the material due to reactions on the surface) such as carbon monoxide, hydrogen sulfide or ethanol, as the main charge carriers are electrons. In contrast, the p-type materials show a decreased conductivity when exposed to reducing gases since their main charge carriers are holes.

As can be seen in Fig. 2.1, SnO_2 is the most extensively studied and widely deployed material for commercial devices. Tin dioxide is a wide-band gap (~3.6 eV) semiconductor with attractive electrical properties [20]. The dual valency of tin, along with tin preferably attaining oxidation states of +2 or +4, facilitates the variation of the surface oxygen composition. Thus SnO_2 sensors offer high sensitivities for different gas species with low detection limits, but unfortunately suffer from the lack of selectivity. Nevertheless, a variety of strategies are adopted to enhance the selectivity and sensitivity of SnO_2-based sensors (eg. synthesis and treatment conditions, micro and nano structures and addition of dopants) [21].

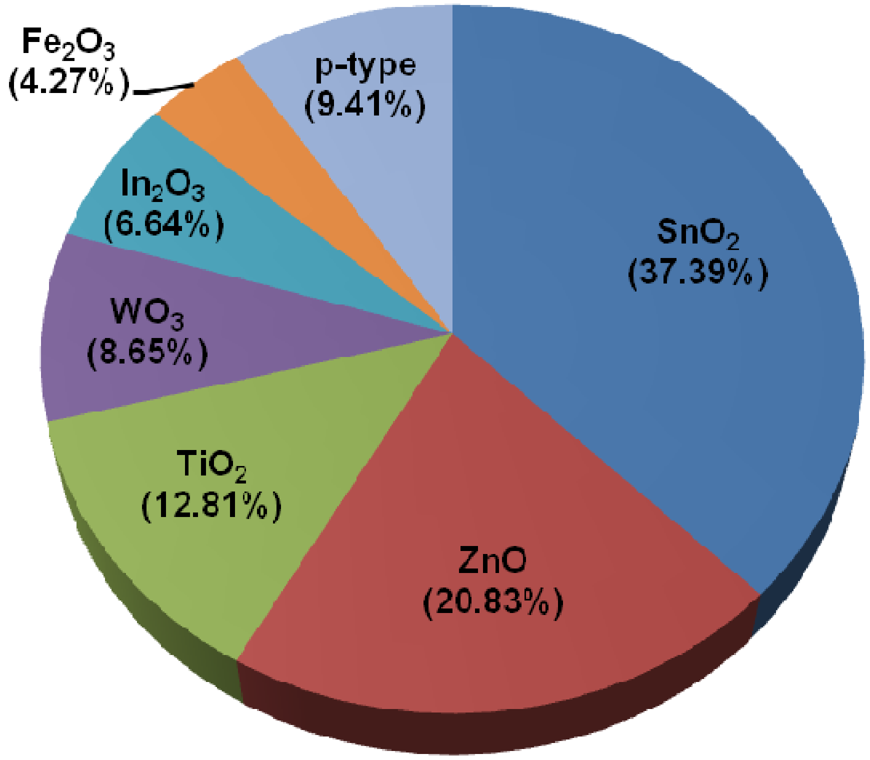

Fig. 2.1. Studies on n- and p-type oxide semiconductor gas sensors [19].

Zinc oxide (ZnO) is a II–VI semiconductor having a wide-band gap of 3.37 eV, with the dominant defects identified as O vacancies [22]. ZnO is identified as a promising gas sensor material because of its low cost, stable electrical and physical properties, suitability for doping and non-toxicity. The sensing property of ZnO is strongly affected by the microstructural features, such as grain size, geometry and interconnectivity between the grains. It is known as a potential sensing material to detect reducing gases such as H_2, CH_4, H_2S and CO.

Titania (TiO_2) has attracted attention for gas sensors because of its lower susceptibly to humidity compared to other metal oxides [23]. Among other applications, TiO_2 has been largely investigated as a sensing layer in resistive oxygen gas sensors operating at medium-high temperatures for automotive air/fuel ratio control. Sensing a variety of other gases is achieved by addition of catalytic noble metals such as Pt, Pd, or by addition of pentavalent dopants.

Tungsten oxide, WO_3 is an n-type semiconductor with tunable band gap in the range of approximately 2.6–3.2 eV, depending on the crystallinity and oxygen deficiency. It shows good response to H_2S, NH_3 and NO_x. In general, the surface of WO_3 is not sufficiently covered with adsorbed $O_{2;}$ hence it is usually incorporated with catalysts or promoters such as Au, Mo, Mg, Re etc., to selectively detect different toxic gases [24].

MOX gas sensors often need to be specifically designed or tailored to operate in a given environment. As mentioned earlier, four important parameters which determine whether a gas sensor can meet the requirements of an application are: sensitivity, selectivity, response time (speed) and stability. These four ‘S’ parameters determine the figure of merit of any gas sensor. Thus the requirement of a sensor is that it will reliably detect the species of interest in a given environment, with a response large and fast enough to be of use in the application without significant drift during its operational lifetime.The four S parameters can be tuned to achieve the desired sensing performance by controlling the synthesis procedure, crystal size and shape, the addition of foreign elements with the role of sensitizers or conductivity modifiers and operating temperature [25].

The grain-size reduction at nanometric level by suitable synthesis methods is one of the popular approaches for enhancing the detection properties of metal oxides. Nanostructures offer high surface area to bulk volume ratio and the comparability of their radii with their corresponding Debye lengths allow rapid transduction of surface interactions into measurable conductance variations. Furthermore, in nanometer size grains, a large fraction of the atoms (up to 50%) are present at the surface or the interface region which actively contribute to the improvement of sensing properties [26].

Doping of metal oxides with suitable additives or promoters (metal particles, foreign metal oxide, ions) is a common way of enhancing the sensing characteristics of chemiresistive gas sensors. They improve the selectivity either by catalytic effect (by dissociating the analyte gas and providing additional adsorbed reactants) or by Fermi energy control (controlling the surface conductivity by electronic coupling between the catalyst and the semiconductor) [5]. Most commonly used additives are noble metals like gold, platinum or palladium [27]. With the advent of nanotechnology, doping is further used to tailor the material properties like reduction in particle size, formation of p-n junctions which may increase the depletion barrier height, creation of core-shell structures, etc.

The chemisorption or redox reaction with the analyte gas at the sensor surface is a strong function of temperature; therefore selectivity for the desired gas can be tailored by operating the sensor at a particular temperature. High temperature operation results in enhanced sensing response due to the lowering of activation energy for gas adsorption and desorption. In addition to selectivity, higher operating temperature improves the response kinetics but it also affects the long term stability [28]. One of the major objectives in current research of MOX sensor is to decrease the operating temperature in order to lower the power consumption, extend the sensor life and also eliminate the safety concern.

2.3 Sensing mechanism of MOX sensors

Chemical modulation of the surface conductivity is the basic principle of operation of MOX gas sensors. Surface conductivity of MOX materials is greatly influenced by the non-stoichiometry in the metal oxide framework. The deviation in stoichiometry results in shallow states made up of oxygen vacancies, which act as n-type donors [29]. Atmospheric oxygen adsorbs on metal oxide surface by capturing an electron from conduction band (for n-type MOX), thereby decreasing the surface conductivity. To improve the selectivity, response time and reversibility in MOX sensors, the required operating temperature is usually between 200 °C and 600 °C. At these temperatures, chemisorption becomes more dominant than physisorption and chemisorption is by far the most selective process. Depending on the operating temperature, ionosorbed oxygen can exist as O_2^-, O^- or O^{2-}. Below 150 °C, molecular oxygen adsorption is dominant in MOX surface and it can be expressed as follows:

$$O_2\,\text{(atmosphere)} + e^-\,\text{(MOX surface)} \rightarrow O_2^-\,\text{(MOX surface)}$$

At temperatures above 150 °C, the superoxide ion O_2^- dissociates to the peroxide form O^-, which is the most reactive species among O_2^-, O^- and O^{2-} [30]. The gas sensing mechanism is mainly governed by the fact that the oxygen vacancies on the oxide surfaces are electrically and chemically active. Fig. 2.2 shows the schematic of gas sensing mechanism for n-type MOX sensor, when exposed to CO.

In General, n-type MOX sensor exhibits two types of sensing responses:

(i) In the presence of oxidizing or charge-accepting molecules such as NO_2 and O_2, the electrons are withdrawn and effectively depleted from the conduction band, leading to a reduction of conductivity.

(ii) When exposed to reducing or electron-donating molecules such as H_2S, CO and H_2, the reaction with surface-adsorbed oxygen releases the captured electrons back to the conduction band, resulting in an increase in conductance.

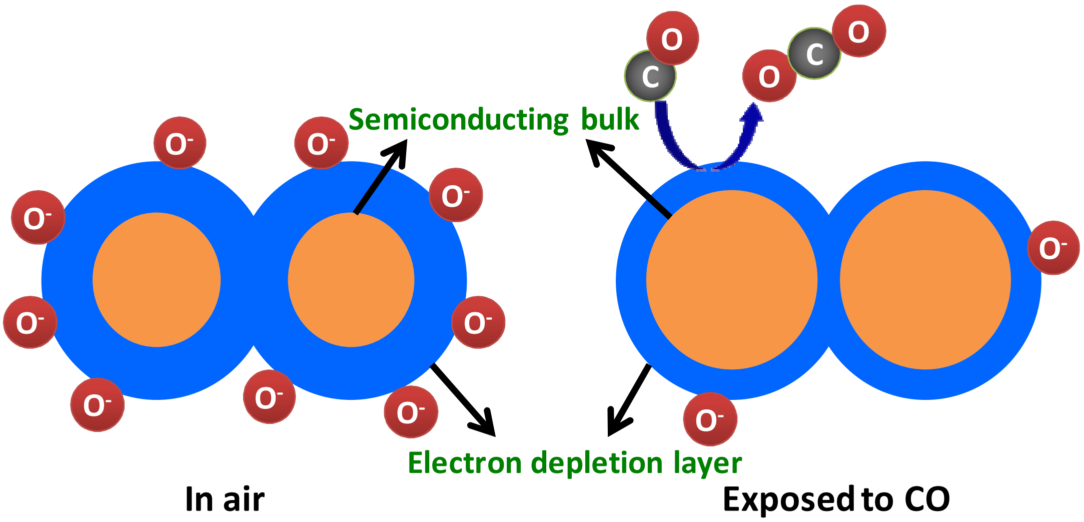

Fig. 2.2. Gas sensing mechanism of n-type MOX sensor when exposed to CO.

The sensitivity of the sensor conductivity to the coverage of adsorbed oxygen on MOX surface leads to a direct relation between the conductivity and the partial pressure of the oxidizing / reducing agents in air [29]. This change strongly depends on the chemical composition and grain size of interconnected particles of the MOX film. Furthermore, the working temperature influences the reaction rate of all surface processes as well as the interpenetration of the gas molecules into the porous sensing layer. Every analyte gas exhibits a specific temperature of maximum sensitivity, which depends on its surface coverage and the conversion rate of ionosorbed oxygen. At this favourable temperature the relative cross sensitivity towards other gases is suppressed to its lowest level, thereby improving the selectivity [30].

2.4 MEMS based gas sensors

Over the past few decades, there has been an increasing interest and development efforts in miniaturizing gas sensors and integration of detection electronics on the same chip. As discussed earlier, among the solid state sensors, MOX gas sensors are the best candidates for miniaturization since they are easy to fabricate, cost effective, compatible with silicon technology and are the most stable among other chemiresistive materials such as polymers and organic films. MOX sensors usually operate between 200 °C and 600 °C in order to achieve the desired sensing performance. This temperature requirement is the basis for surface chemical reactions induced gas sensitivity as well as is the main reason for the power consumption in MOX sensors. In an optimized gas sensor design, the power consumption can be minimized by reducing the size of both the heater and the sensor. In this context, MEMS based techniques have been gathering a strong focus in the field of gas sensors, especially for the purpose of realizing micro heaters with excellent thermal insulation [31]. A variety of MEMS based structures viz. microhotplates, microcantilevers, microbeams, etc., are available for sensor applications [32 - 36]. MEMS based sensors yield many advantages which make them an ideal platform for repeatability and mass production. Due to the relatively small dimension, integrated circuit fabrication techniques allow thousands of identical devices to be built simultaneously on a single silicon wafer. Compared to building up a device from individual components, the simplicity of batch fabrication greatly reduces the cost and improves the reliability. In addition, MEMS can be packaged into arrays and integrated with electronics that require much less power, which often find applications where weight, power and space requirements are critical.

2.4.1 MEMS technology based structures for gas sensors

Any engineering system that performs electrical and mechanical functions and whose components are in micrometer dimensions is a MEMS. MEMS requires multidisciplinary approach to design including knowledge of fabrication technology, mechanics, electro-mechanics and electronics. MEMS offers several advantages namely:

(i) Due to low mechanical inertia, small systems tend to respond faster hence they are ideal for precision movements and for rapid actuation.
(ii) Due to low mass, miniaturized systems encounter less mechanical vibration and thermal distortion.
(iii) Small systems have better dimensional stability at high temperatures due to low thermal expansion.
(iv) Small systems occupy less space thus allowing the packaging of more functional components in a single device. This can further lead to low cost of production and transportation.

Typical MEMS production process is shown in Fig. 2.3. The fabrication process starts with a substrate (in this case silicon) which undergoes a succession of processes that add, modify or remove materials in precise patterns in order to get the desired microstructures. Releasing of the mechanical parts is done either before or after the wafer is diced into individual chips. This is followed by assembling, packaging and final testing [37]. Despite the fact that MEMS uses most of the same processes as those used with ICs, the major challenge remains in the system integration between the miniature mechanical structures and the electronic interface.

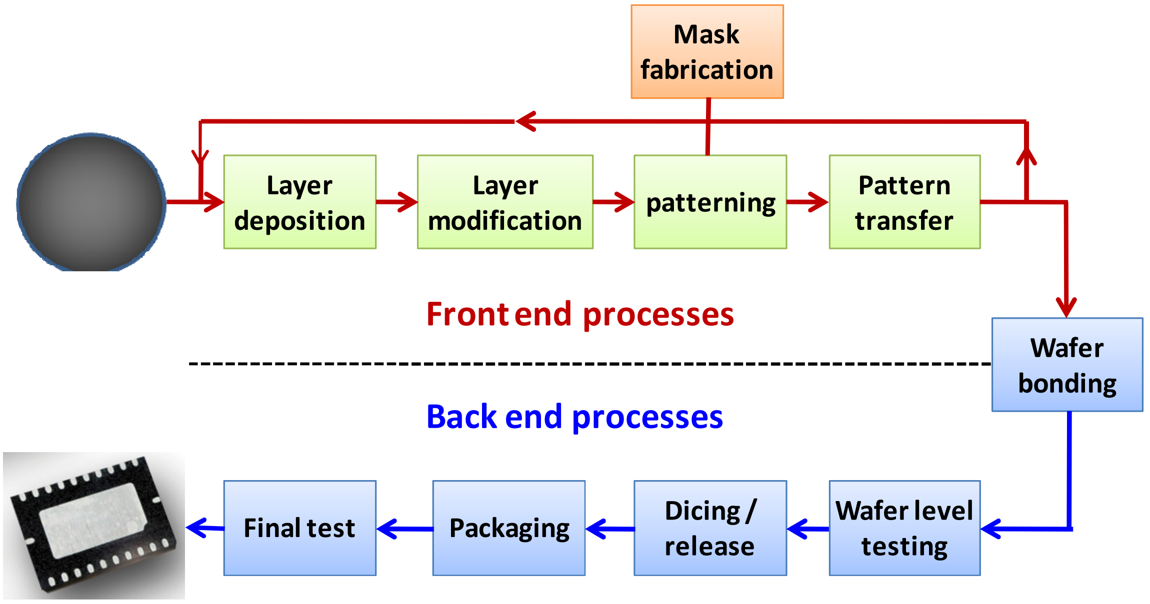

Fig. 2.3. Typical MEMS production process [37].

In general, MEMS devices and structures are fabricated using conventional integrated circuit processes, such as deposition, lithography and etching, together with specially developed micromachining techniques. These techniques can be broadly categorized as bulk micromachining, surface micromachining and LIGA. Bulk micromachining technique builds mechanical elements by starting with a silicon wafer and then, selectively etching the unwanted parts to achieve the desired mechanical structures. Surface micromachining provides a complementary technique, in which layers of suitable materials are deposited above the substrate surface. These layers are used as structural or sacrificial layers to be removed at a later stage to produce freestanding structures and moveable parts. LIGA, a German acronym for lithography (LIthographie), electroforming (Galvanoformung), and molding (Abformung) is a technology which combines collimated X-ray lithography with electroplating and molding techniques to create high aspect ratio (tall and thin) structures or deep cavities.

One of the objectives of this research work is to study MEMS based devices for gas sensing applications, which involve design, simulation, fabrication and testing of suitable MEMS structures. After extensive literature survey, it was concluded to explore the following structures based on standard Multi User MEMS Processes (MUMPs) for fabrication in a multi product wafer run (MPW) [38].

(i) Microhotplates with different membrane size and embedded heater

(ii) Microcantilever of various shapes, sizes with or without heater and piezo resistor

The following sections describe the technology and thermal analysis of micro hotplates, theory and operation of micro cantilevers, overview of the MUMPs process and MEMS design tool used for the design and simulation studies.

2.4.2 Microhotplate (MHP) concept and technologies

As seen earlier, MOX gas sensors operate in the temperature range between 200 °C – 600 °C in order to enhance the chemisorptions process, which in turn improves the selectivity. Higher operating temperature also aids the speed of response, sensitivity and reversibility. Most of the commercially available MOX sensors are nowadays manufactured using screen printing technique on small and thin ceramic substrates. However, screen-printed ceramic gas sensors are still in need of improvements with respect to power consumption, mounting technology and selectivity. The power consumption of screen-printed devices is typically in the range of hundreds of mW to about few watts, making them unsuitable for hand held applications [39]. Also, packaging of the hot ceramic substrate is difficult. Thus the main focus of gas sensor design is to reduce the power consumption and minimize the heat losses owing to conduction, convection or radiation by the heater. This can be accomplished by reducing the mass of both the heater and sensor element and by optimizing the heater design for uniform heating [40].

Research on micromachined gas sensors over the last few decades has enabled to overcome most of the above challenges. The sensitive layer of micromachined gas sensors is deposited on thin dielectric membrane of low thermal conductivity, which offers excellent thermal isolation between the substrate and the gas-sensitive heated area on the membrane (Fig. 2.4). Thus the power consumption can be kept very low (30 - 150 mW) while the substrate stays nearly at ambient temperature [41 - 44]. The mounting of the sensor element is much easier unlike the hot ceramic sensor element, making it viable for the integration of control and signal-processing electronics on the same substrate. Thus the requirements of a MHP for sensing platform can be summarized as below:

(i) Well-controlled homogeneous temperature distribution over the gas sensing layer because the sensing properties of metal oxides are strongly influenced by temperature.

(ii) Lowest possible heat losses to minimize the power requirements.

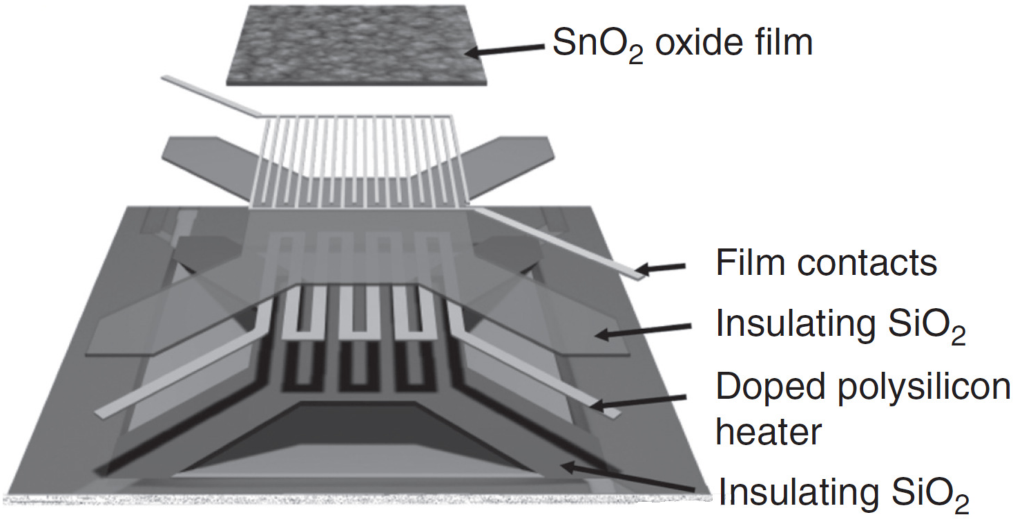

Fig. 2.4. Cross-sectional view of a micromachined MOX gas sensor [46].

(iii) High mechanical strength in order to withstand all the processing steps used to form the micromachined structures.

(iv) Stability during the deposition of the sensing film and subsequent processing.

(v) Good thermal isolation to facilitate the integration of signal processing electronics in the same housing.

There are two main types of MHP structures available for micromachined gas sensors using metal oxide as the sensing material. First one is the closed-membrane MHP and the other is the suspended-membrane or the spider-type MHP. Schematic and cross-sectional views of these structures are presented in Fig. 2.5. The closed-membrane type sensor is formed by anisotropic etching of silicon substrate from the backside. The suspended-membrane type is completely processed and released from the front-side. Thickness of the membrane for both MHPs typically ranges from 0.5 µm to 2 µm. Closed-membranes have lateral dimensions of about 0.5 mm to 1 mm, out of which 50 to 60% can be used as the active area. Suspended membranes typically have a lateral dimension between 100 to 500 µm. Both types use SiO_2, Si_3N_4, SiO_2 / Si_3N_4 sandwich or SiON membranes. SiO_2 has the lowest thermal conductivity (~ 2 $Wm^{-1}K^{-1}$ at RT) [45] among the available CMOS materials, but tends to exhibit compressive stress on silicon substrates, thus not preferred for membranes. Si_3N_4 has a thermal conductivity which is about ten times than that of SiO_2 (~ 20 $Wm^{-1}K^{-1}$ at RT). Si_3N_4 tends to be under tensile stress when deposited on silicon substrates, thus making it an ideal material for the use as membrane or diaphragm. Suspended membrane exhibits lower power consumption due to better thermal isolation from the silicon substrate, while a closed membrane is more convenient for pattering the sensing element. As the suspended membrane is completely processed from the front side, it is considered to be more compatible with

CMOS process [46]. However, closed membrane type is a robust, well established technique, which allows large area membranes.

As shown in Fig. 2.5, the gas sensitive layer is deposited on the metal electrodes, which are formed on the top surface of the membrane. Common electrode materials are gold and platinum in combination with an adhesion metal like Titanium or Chromium. The heater and thermometer can be integrated in the same layer as the electrodes (coplanar) or in different layers (embedded) as shown in Fig. 2.6. A coplanar heater has the advantage of reduced process steps but obtaining temperature homogeneity may pose a challenge. Though embedded heater requires additional layers, it allows well controlled temperature

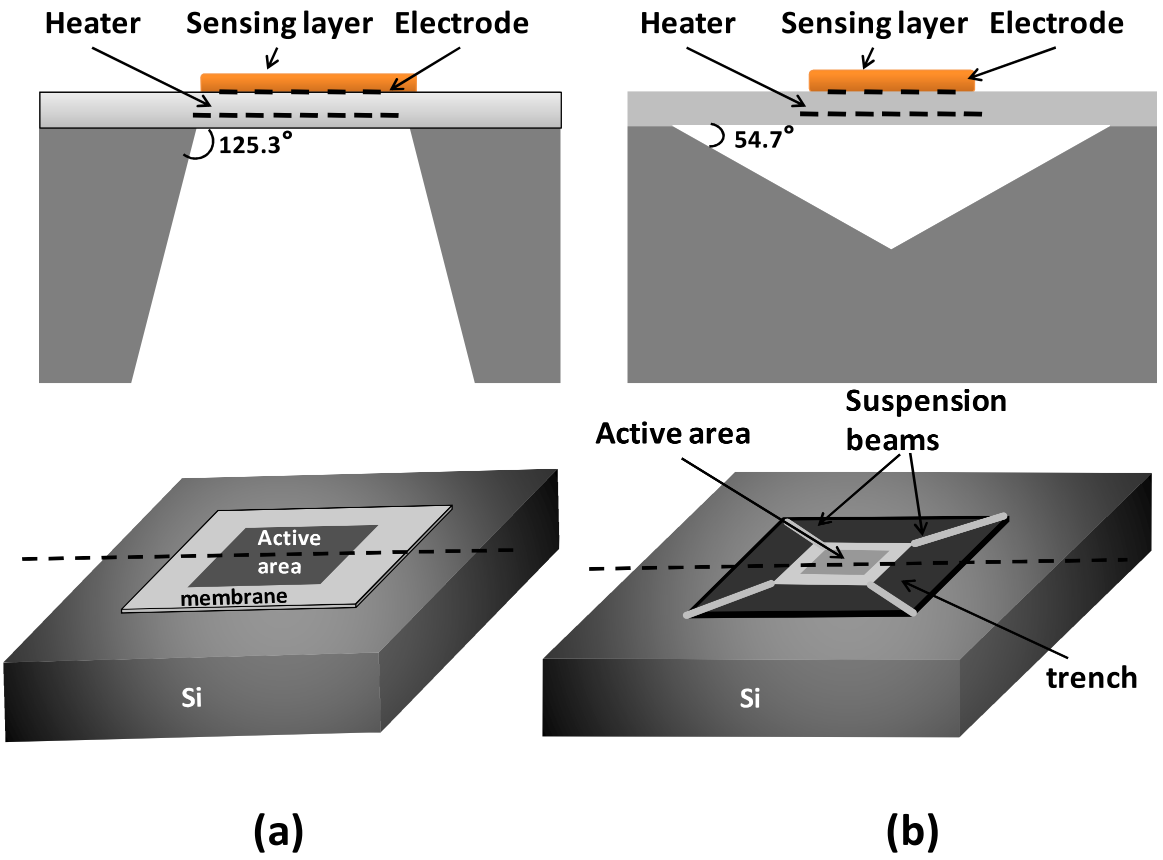

Fig. 2.5. Schematic and cross sectional views of (a) closed-membrane and (b) suspended-membrane type MHPs.

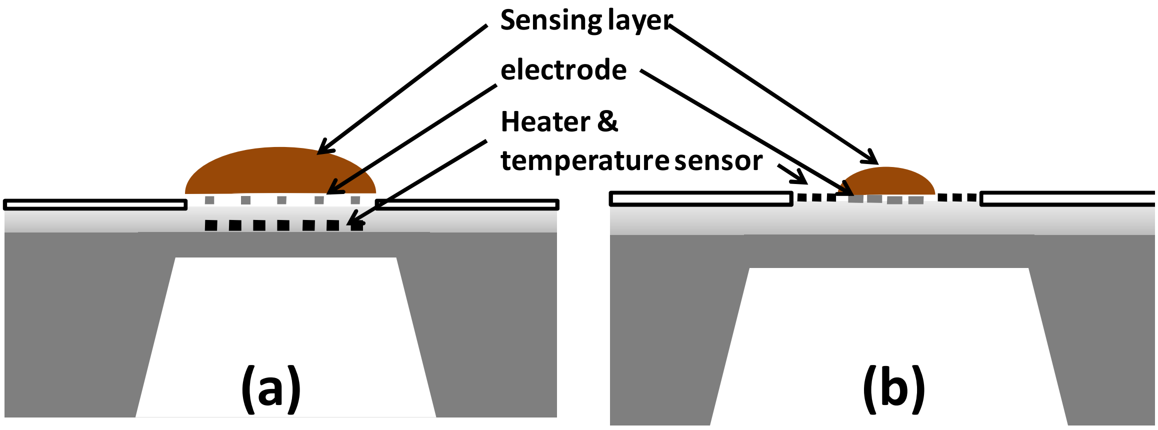

Fig. 2.6. (a) Embedded and (b) coplanar heater / thermometer structures.

distributions over the active area. Commonly used materials for heater and temperature sensor are poly silicon, platinum or P^{++} doped silicon. Many times the same structure is used for both heater and temperature sensor [40].

2.4.3 Thermal analysis of MHPs

MHPs generate heat by Joule heating of the resistive heater element. The thermal energy, Q, generated by the Joule effect is given by [46]:

$$\Delta Q = R\, I^2\, \Delta t \tag{2.1}$$

where I is the current flowing through the heater resistance R during Δt time. This heat is dissipated in the device and in the surrounding environment by three means as shown in Fig. 2.7. Along the membrane, heat flow is through conduction. Above and below the membrane, heat transfer occurs due to heat conduction and heat convection through the surrounding atmosphere. Additionally, radiative heat transfer takes place due to emission of electromagnetic waves from the hot surface. Assuming that the different components of heat

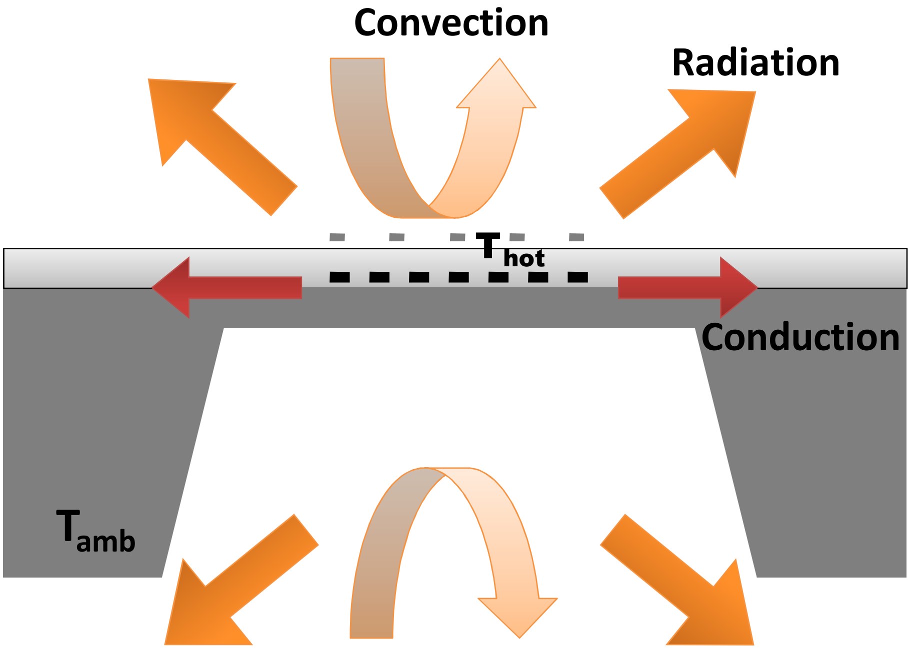

Fig. 2.7. Heat losses in MHPs – Conduction, convection and radiation [46].

losses through / from the membrane are additive, the total heat loss can be expressed as [40]:

Q_{tot} = Conduction through membrane + conduction through air

+ radiation loss + convection and other losses

$$Q_{tot} = G_m \lambda_m (T_{hot} - T_{amb}) + G_{air} \lambda_{air} (T_{hot} - T_{amb}) + G_{rad} \sigma \varepsilon (T_{hot}^4 - T_{amb}^4) + \Delta x \tag{2.2}$$

The first term describes the heat conduction through the closed membrane, the second term accounts for heat conduction through the ambient air, the third term ascribes the heat losses due to radiation and the last term represents unknown heat losses including free convection. G_m, G_{air} and G_{rad} are the geometry factors, which are mainly dependent on the membrane / device design. T_{hot} and T_{amb} are the temperatures of the heated active area and the ambient, respectively. λ_m, λ_{air} are the thermal conductivity of the membrane and the surrounding atmosphere, ε is the emissivity and σ is the Stefan-Boltzmann constant.

For modeling the conduction component through the membrane, only lateral conduction from heater to membrane needs to be considered because vertical conduction from heater to membrane is negligible as the thickness of membrane is usually small compared to the lateral dimensions. For the suspended membrane structures used in this research work, the conduction can be modeled as 1-D structure compared to 3-D modeling of closed membrane counterpart. In case of four suspension arms, heat conduction through membrane is given by:

$$Q_{membrane} = \frac{4(\lambda_m A_{beam})(T_{hot} - T_{amb})}{l} \tag{2.3}$$

and

$$G_m = \frac{4A_{beam}}{l} \tag{2.4}$$

where l is the length of the suspension arm and A_{beam} is the cross sectional area. Eq. (2.3) shows that the membrane should be made of low thermal conductivity material. Also, the length to width ratio of the suspension beams and thickness of the membrane should be chosen to minimize the heat losses.

Generally, heat losses to the surrounding air occur because of (i) forced convection due to fluid motion and (ii) free or natural convection. In case of microhotplates, convection through air can be neglected due to the small size of the microhotplate and restricted fluid (air) motion within the packaged sensors with perforated encapsulation [40, 47, 48]. Assuming that the heat transfer to air is only by heat conduction, the second term in eq. (2.2) can be approximated as:

$$Q_{conduction} \approx 4\pi r_i \lambda_{air}(T_{hot} - T_{amb}) \tag{2.5}$$

and

$$G_{air} = 4\pi r_i \tag{2.6}$$

where r_i is the radius of the concentric sphere of the hot surface of the membrane. Eq. (2.5) suggests that the heat losses to the air can be best minimized by minimizing the heated area, maximizing the distance between the cold substrate and the hot membrane and by choosing low operation temperature.

Power losses by radiation Q_{rad} can be obtained by using Stefan-Boltzmann law [42]:

$$Q_{rad} = G_{rad}\sigma\varepsilon(T_{hot}^4 - T_{amb}^4) \tag{2.7}$$

where σ (= 5.67e-8 $Wm^{-2}K^{-4}$) is the Stefan-Boltzmann constant and ε (emissivity) has a value between 0 and 1, depending on the composition of the MHP surface. Heat losses due to radiation can be neglected, if the heater is designed to operate in the moderate temperature regime (<500 °C) as the radiation loss contributes to < 1% of total heat loss [11]. However, due to the T^4 dependency, radiation losses cannot be ignored if the operation temperature exceeds 700 °C. As radiation linearly depends on material emissivity, it is a common practice to coat low emissivity materials (e g. gold) on the backside of the membrane in order to reduce radiation loss at high temperatures [48].

From the above discussions, it can be concluded that at low temperatures, the heat loss can be completely attributed to heat conduction through the membrane, the heater material and air. At higher temperatures the convection heat losses through surrounding air and radiation heat losses cannot be neglected [49 - 51]. The heat losses can be minimized by using low thermal conductivity material for membrane, small heater area, suitable metal coating at the backside of the membrane, suspension beams with high length-to-width ratio and a deep trench below the membrane.

2.4.4 Theory and operation of microcantilevers

Basically, microcantilever is a single supported beam, which exhibits strain and bending characteristics due to surface stresses. These two aspects - strain and bending, are exploited for most of the static sensing applications, where the cantilever bends due to an attached mass or force acting upon it [52]. A cantilever can be also be described as a second-order system with distinct resonance characteristics dependent on the cantilever mass and spring constant as well as on the ambient conditions. Any changes in these parameters will be reflected as a variation in the resonance characteristics, which is the base for dynamic sensing applications [53, 54]. In gas sensor applications the microcantilever surface is coated with a thin layer of a material that shows affinity to the specific gases of interest. The resulting surface stress due to the preferential adsorption of gas species is monitored, which results in the bending and mass change of the microcantilever. The two main modes of microcantilever operation are - adsorption-induced deflection or static mode and the resonant frequency shift induced by mass change or dynamic mode.

2.4.4.1 Static mode operation

Static deflection is used to quantitatively determine the amount of material adsorbed onto the microcantilever and the magnitude of deflection is proportional to the adsorbed material [55, 56]. Deflection results due to two mechanisms: added mass and surface stress from adsorbed species [57, 58]. However, the surface stress need not necessarily correlate with the amount of material adsorbed. The sources of surface stress can be the surface reconstruction [59], interactions between a surface and adsorbates [60, 61] or the expansion of a deposited thin film arising from temperature changes. Surface stresses will be either tensile or compressive depending on adsorbate - surface interactions.

In general, the adsorption of the molecules is modeled as a load or force acting on the surface of the microcantilever. The deflection of the free end of the cantilever depends on the type of loading to which the beam is subjected. If a concentrated load F is applied on the free end of the cantilever along z-axis (Fig. 2.8), then the vertical displacement $z(x)$, of the cantilever at a distance x from the fixed end is given by [62]:

$$z(x) = \frac{FL}{2EI} x^2 \left(1 - \frac{x}{3L}\right) \tag{2.8}$$

where E is the Young's elastic modulus of the beam material, L is the length of beam, and I is the area moment of inertia of the microcantilever cross-section about its neutral axis. I is a function of the beam width w, thickness t and is equal to $wt^3/12$ for rectangular microcantilevers [63]. Eq. (2.8) is valid as long as the beam deflection is negligible compared to its length (i.e., $\Delta z << L$). The spring constant k, which is the ratio of force to deflection of the free end, is given by [64]:

$$k = \frac{F}{\Delta z} = \frac{3EI}{L^3} \tag{2.9}$$

If the force is exerted at an arbitrary point, x_f on the cantilever, eq. (2.8) can be generalized as:

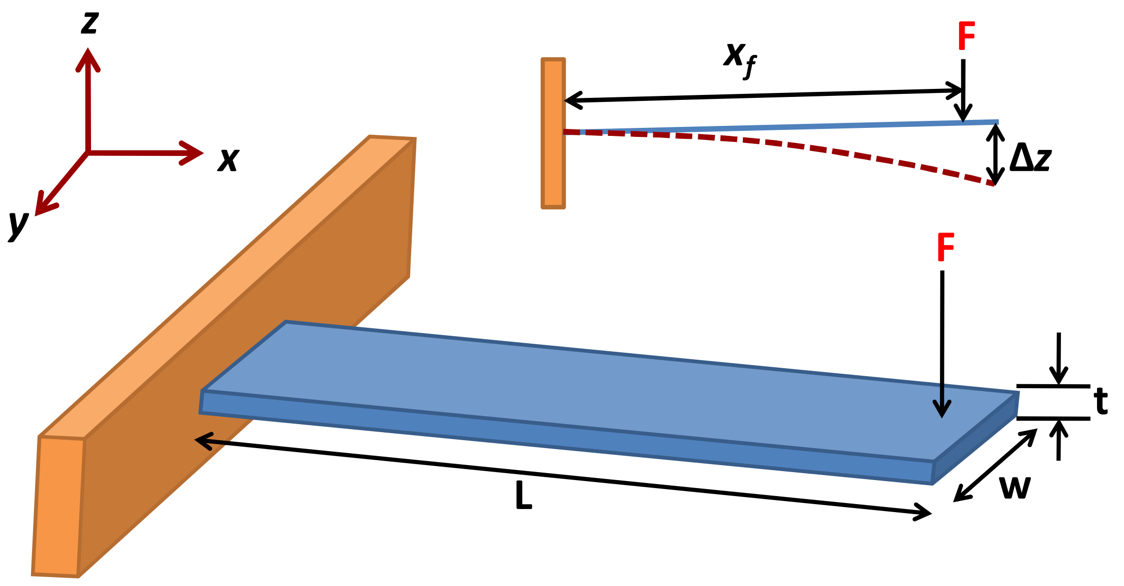

Fig. 2.8. Schematics of the cantilever geometry and nomenclature; F is the force exerted along z-axis at distance x_f and Δz is the resultant deflection at the free end.

$$z(x) = \frac{FL}{2EI} \times \begin{cases} \frac{x_f}{L} x^2 \left(1 - \frac{x}{3x_f}\right) & x \le x_f \\ 2\frac{x_f^2}{L}\left(\frac{x_f}{3} + \frac{x - x_f}{2}\right) & x_f \le x \le L \end{cases} \tag{2.10a}$$

Maximum deflection results when at x = L and x_f = L, which is given by:

$$\Delta z_{max} = \frac{FL^3}{3EI} \tag{2.10b}$$

When a point force F is applied at the tip of the cantilever, the stress of the cantilever at a distance x from the fixed end is given by:

$$\sigma_x(x) = \frac{12z(L-x)}{wt^3} F \tag{2.11}$$

Here z is the distance from the neutral axis to the cantilever top surface in the z direction. The neutral axis is an axis in the cross section of a cantilever beam, along which there are no longitudinal stresses or strains. If the cantilever geometry is symmetric and is not curved before a bending occurs, then the neutral axis lies at the geometric centroid. Therefore the maximum stress will be at the surface (i.e. $z = t/2$). If variation with distance x is considered, then the maximum stress is found to be at the fixed end (i.e. $x = 0$). In the case of a gas sensor, the deflection is the result of an isotropic surface stress, which acts over the entire surface of the microcantilever. It is difficult to solve this problem analytically and generally FEM is used find an effective solution. Nevertheless, adsorption-induced stress is often calculated using Stoney's equation as [65]:

$$\Delta\sigma = (\Delta\sigma_1 - \Delta\sigma_2) = \frac{Et^2}{6R(1-\upsilon)} \tag{2.12}$$

where, E is the modulus of elasticity, t is thickness of cantilever, R is bending radius of cantilever and v is Poisson's ratio, $\Delta\sigma_1$ and $\Delta\sigma_2$ are the stresses acting on the top and bottom surfaces of the beam. Only a difference in the adsorption between the top and bottom surfaces will cause deflection; equal adsorption to both top and bottom surfaces will counteract each other, resulting in no deflection. Surface stresses in solids are assumed to be analogous to the surface tension in liquids. The unit of surface stress measurement is different from that of bulk stress. For the bulk stress it is N/m^2, whereas for surface stress it is N/m [66].

Using the geometric relation, the bending radius and the beam end deflection can be expressed as [65]:

$$\frac{1}{R} = \frac{2\Delta z}{L^2} \tag{2.13}$$

From eqs. (2.12) and (2.13) the deflection and the differential stress can be related as:

$$\Delta z = \frac{3\,(1-v)}{E}\,\Delta\sigma\left(\frac{L^2}{t^2}\right) \tag{2.14}$$

Stoney's equations (eqs. (2.12) and (2.14)) predict the residual surface stresses in thin films by measuring the induced deflection. It assumes that the deflection is unrestrained at all edges and there is no interaction between adsorbed species. In practical applications however at least one edge of the plate must be constrained to get the desired action. Sader [67] has developed a more complete solution for the deflection of a fixed cantilever beam under the influence of a surface stress given as:

$$\Delta z = \frac{3K\,(1-v)L^2}{Et^2}\,\Delta\sigma \tag{2.15}$$

where K is a constant dependent on the material and geometric properties of the cantilever. For a cantilever having (l/w) ratio ≥ 5 and $v \leq 0.25$, the value of K lies between 1 and 1.05.

Stoney's and Sader's equations can be used to correlate the deflections of microcantilevers to the surface stresses resulting from adsorbed species. In general, the surface stress is calculated from the cantilever deflection, but it is difficult to determine surface stress from molecular adsorption as the physical parameter and the processes involved are rather complex and unknown [62].

2.4.4.2 Dynamic mode operation

Dynamic mode of microcantilever sensor exploits the fact that the resonant frequency of the cantilever is an inverse function of the mass of the cantilever. It is possible to make indirect mass change estimations in the atto to zepto gram range by measuring the resonant frequency shift of the cantilever [68]. For a thin beam as depicted in Fig 2.8, rotational inertia and shear deformation can be neglected. Assuming a linear elastic material and small deflections (Δz « L) the equation of motion is given by the Euler–Bernoulli beam equation [69]:

$$\frac{\partial^2 z(x,t)}{\partial t^2}\rho wt + \frac{\partial^4 z(x,t)}{\partial t^4}\,EI = 0 \tag{2.16}$$

where $z(x\ ,t)$ is the time dependent vertical displacement at a distance x and ρ is the mass density of the cantilever material. ρ is expressed as ($\rho = m/V$), where V is the volume of the cantilever given by ($V = L\ w\ t$). To find out the undamped natural frequency of oscillation of the microcantilever, the external force is assumed to be zero, i.e. $F = 0$. The solution to the above differential equation is a harmonic that can be separated into a position dependent and a time-dependent term as:

$$Z(x,t) = \ Z_n(x)e^{-j\omega_n t} \tag{2.17}$$

where ω_n is the frequency of motion and n denotes the modal number. By substituting this into eq. (2.16), the differential equation can be rewritten as:

$$\frac{\partial^4 z(x,t)}{\partial t^4} = \kappa^4\ z(x,t) \tag{2.18a}$$

where,

$$\kappa^4 = \frac{\omega^2 \rho w t}{EI} \tag{2.18b}$$

The solutions (Eigen functions) of the above simplified beam equation can be written in the form [59]:

$$z_n(x) = \ A_n(\cos\kappa_n x - \ \cosh\kappa_n x) + \ B_n(\sin\kappa_n x - \ \sinh\kappa_n x) \tag{2.19}$$

where A_n and B_n are arbitrary constants. The above equation is solved for the cantilever by applying the following boundary conditions:

For the clamped end (at $x = 0$) $\quad z = 0, \frac{\partial z}{\partial x} = 0$

For the free end (at $x = L$) $\quad \frac{\partial^3 z}{\partial x^3} = 0,\ \frac{\partial^4 z}{\partial x^4} = 0$

By applying the above boundary conditions, eq. (2.19) has a nontrivial solution only if

$$\cos(\alpha_n)\ cosh(\alpha_n) + 1 = 0 \tag{2.20}$$

where α_n = κ_nL. Through numerical solutions, the values of α_n for different modes can be found as $\alpha_1 = 1.8751$, $\alpha_2 = 4.6941$, $\alpha_3 = 7.8548$, $\alpha_4 = 10.9956$, for ($\alpha \gg 1$), $\alpha_n = (2n - 1)\ \pi/2$.

The above results imply that a beam will vibrate in certain vibrational modes, each with a distinct spatial shape. The first four such vibrational mode-shapes of a cantilever are shown in Fig. 2.9. It can be seen from the figure that certain areas of the cantilever have large vibrational amplitude and near the nodal points the amplitude is low. The number of nodal points increases with increasing mode number [69]. The frequency of vibration of each of the mode shapes is called the Eigen or natural frequency of

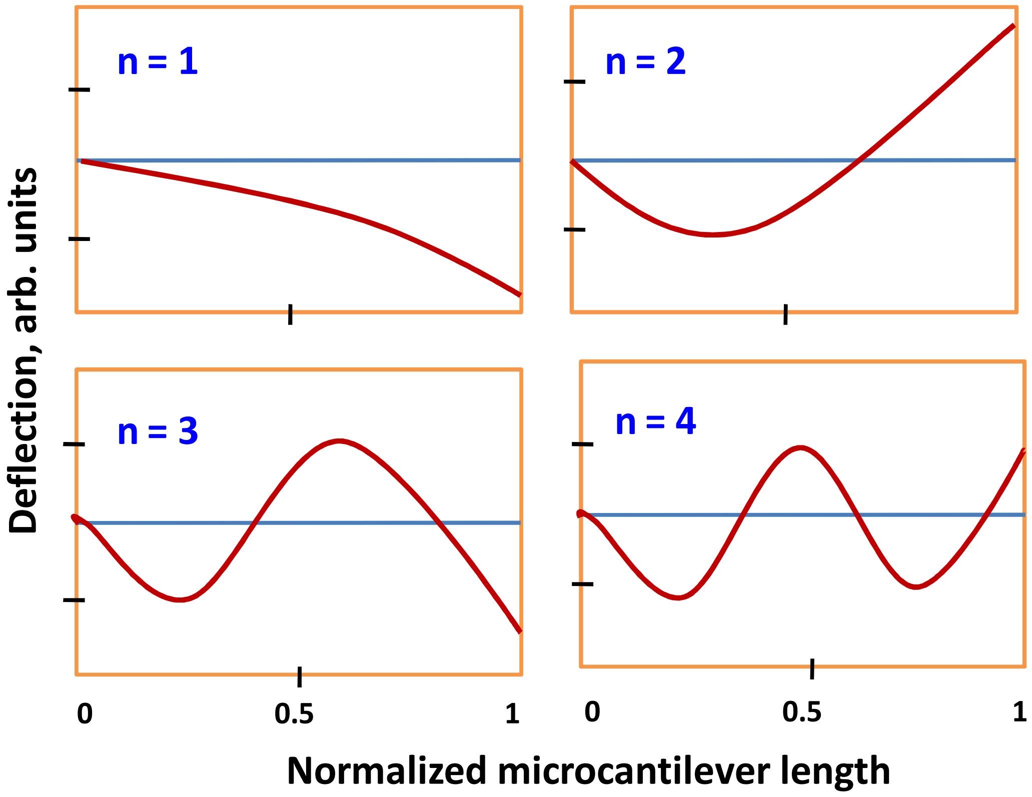

Fig. 2.9. The first four bending modes (n = 1,2,3,4) of a microcantilever; 0 is fixed end and 1 is free end (The cantilever is seen from the side).

the corresponding mode. Eq. (2.18), which is a fourth order differential equation, can be solved to find the n-th mode natural frequency of bending of the cantilever [56]:

$$f_n = \frac{\omega_n}{2\pi} = \frac{1}{4\pi}\left[\frac{\alpha_n}{L}\right]^2\sqrt{\frac{EI}{\rho wt}} = \frac{\alpha_n^2}{4\pi}\sqrt{\frac{E}{\rho}}\left(\frac{t}{L^2}\right) \qquad (2.21)$$

Also, by using equation (2.9),

$$f_n = \frac{\alpha_n^2}{2\pi\sqrt{3}}\sqrt{\frac{k}{m}} \qquad (2.22)$$

Thus the first natural frequency can be calculated by substituting $\alpha_1 = 1.8751$:

$$f_1 = \frac{1}{2\pi}\sqrt{\frac{k}{m_{eff}}} \qquad (2.23)$$

where $m_{eff} = 0.2427m$. Equation (2.23) is used to calculate the 1st resonant frequency of rectangular microcantilever. From eq. (2.23) it is evident that the resonant frequency depends on the vibrating mass. The shift in resonant frequency in response to a change in the mass is called the sensitivity S of a resonating microcantilever.

$$S = \frac{\Delta f}{\Delta m} \qquad (2.24)$$

where Δf is the change in resonant frequency caused by an added mass Δm. To achieve high sensitivity, a cantilever must have a high resonant frequency, which can be realized by having small dimensions and using a material with large Young's modulus and low mass density. In addition, a higher sensitivity can be obtained at higher vibrational modes due to a decreasing effective mass at higher modes [70]. In dynamic mode, a cantilever is oscillated mostly at or very near to the resonant frequency. Unlike static mode operation, the cantilever can be functionalized on both the surfaces in dynamic mode operation. As molecules get adsorbed on the cantilever surface(s), either the mass or spring constant or both can change [53, 71]. Additionally, adsorption induced surface stresses on the cantilever also changes the frequency of the cantilever [72, 73]. The cumulative effect results in change of resonant frequency, which in turn is used to quantify the adsorbate.

2.4.4.3 Detection techniques for microcantilever sensors

As discussed in the above sections, microcantilever sensors have two operational modes; cantilever bending due to differential adsorption and resonance frequency variation due to mass loading. Based on the method of operation, the detection schemes employed for microcantilever based sensors can be primarily categorized into optical and electrical schemes [74]. The former includes optical deflection and resonant frequency techniques and the latter includes piezoresistive, piezoelectric or capacitance measurements [75]. Owing to the simplicity and cost effectiveness, electrical detection is more widely used, especially in integrated sensor systems. This section highlights few of the widely used transduction schemes for microcantilever based sensors.

(i) Optical method

Optical transduction is the most widely used method for quantifying static and dynamic deflections. In this method, a laser beam is focussed on the free end of the microcantilever, which acts as a mirror (Fig. 2.10). The reflected laser light is detected by a position sensitive photo detector. In this method, the cantilever functions only as a light-reflecting super-soft spring, hence often referred as an optical lever. Optical transduction method is one of the most sensitive readout method for microcantilever sensors which can detect deflections as small as a few angstroms (= 10^{-10} m). Other advantages of the optical lever method are linearity of response, simplicity and reliability. However, optical transduction changes its response in different surrounding medium. The alignment of the system requires high precision and is expensive. Moreover, this technique is not suitable for developing miniaturized single or multiple sensors based sensing systems [53].

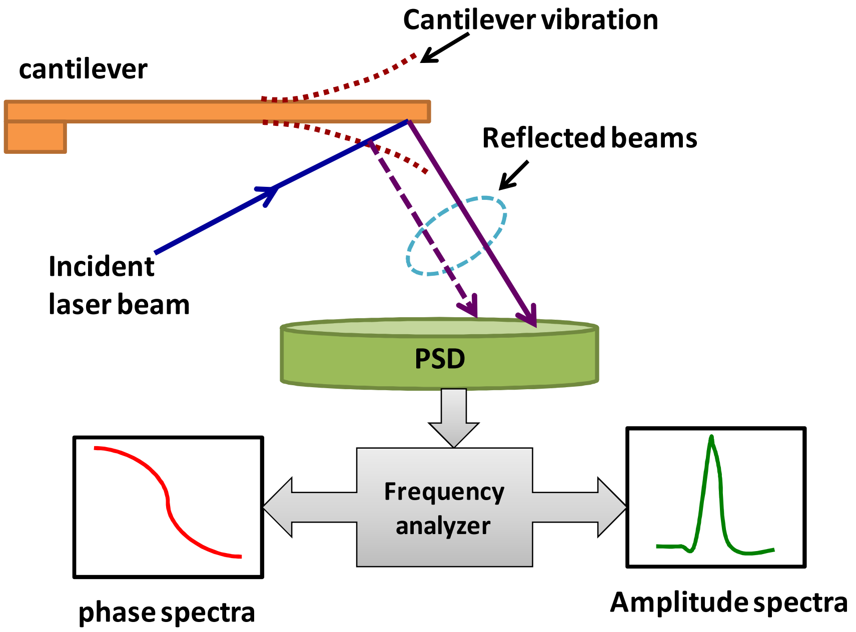

Fig. 2.10. Schematic diagram of optical transduction system.

(ii) Resonant frequency method

In this method the sensor is mounted on a resonator as shown in Fig. 2.11 and the shift in the resonant frequency in respect to the adsorbate is measured. A resonator is a mechanical structure that vibrates at a particular resonant frequency. Resonators can be fabricated from a range of single crystal materials with micron-sized dimensions using various micromachining processes. The resonant cantilever sensor outputs a frequency-shift signal that is induced by specific mass adsorption as governed by Hooke's law:

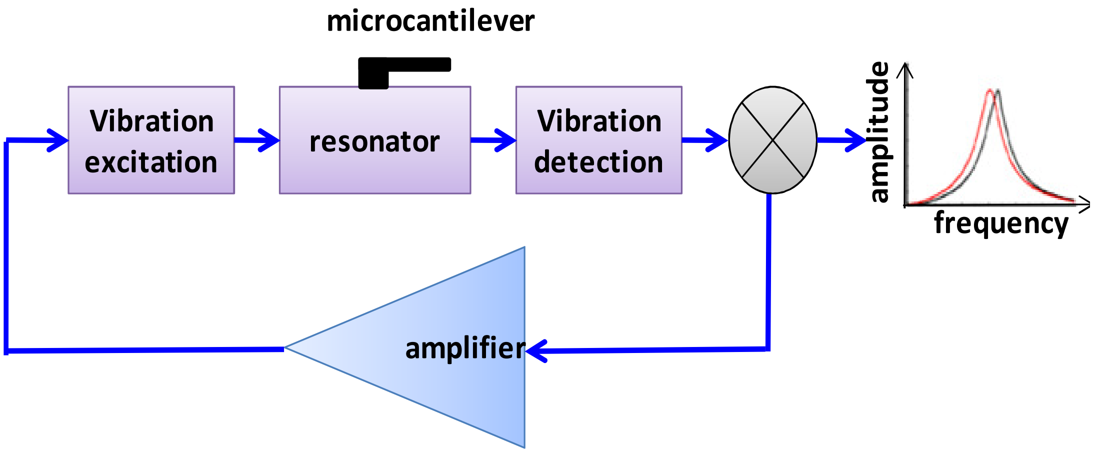

Fig. 2.11. Block diagram of a resonant mode cantilever sensor.

$$\frac{\Delta f}{f_0} \approx \frac{0.5\Delta m}{m_{eff}} \tag{2.25}$$

where the adsorbed mass of Δm is much smaller than the cantilever effective mass of m_{eff}, Δf and f_0 are the frequency shift and the original resonant frequency respectively [77]. From the above equation, it is clear that the smaller the detectable frequency shift, the finer the mass sensing resolution. The quality factor, Q of a microcantilever is defined as the ratio of the resonance frequency f_0 to the full width half-maximum (FWHM) of the resonance peak. The quality factor indicates the narrowness of a resonant peak. A higher Q value can resolve the peak shifts accurately. Considering the micron size dimensions of the cantilever and the kHz to MHz resonant-frequency range, air damping is the dominant factor in determining the Q value, when the cantilever vibrates in an atmospheric environment [78]. Similar to optical lever method, resonance method is also highly sensitive, reliable and has linear response but more complex and susceptible to the operating environmental conditions.

(iii) Piezoresistive method

The electrical conductivity of a piezoresistive material changes when stress is applied to it. The piezoresistive method involves embedding of a piezoresistive material near the fixed end of the cantilever to record the stress change occurring on the surface of the cantilever. As the microcantilever deflects due to applied force, the resultant strain in the piezo material causes a change in resistance, which can be measured by electronic means. To achieve high sensitivity, the piezoresistor is usually placed at the top or bottom surface of the cantilever beam near the base where the stress is maximum (Fig. 2.12).

The gauge factor (GF) of a material which is used to symbolize the strain sensitivity is given by:

$$G = \frac{\Delta R/R}{\Delta L/L} \tag{2.26}$$

where R is the initial resistance, ΔR is the change in resistance, L is the initial length of the piezoresistor and ΔL is the change in length. The numerator is also known as strain, ε. For thin metal films, the geometric effect dominates the piezoresistive effect. Semiconductors have excellent piezoresitivity due to their high gauge factor (G > 100), but their greater sensitivity to temperature variations and tendency to drift are disadvantages in comparison to metal film sensors [79]. Another disadvantage of semiconductor piezoresistor is that the resistance-to-strain relationship is nonlinear though this can be taken care by software compensation. The advantage of using a piezoresistive detection method is that neither additional optical components nor laser alignment is needed. This technique is applicable for static as well as dynamic measurements. In addition, the piezoresistive readout system can easily be integrated on the same chip using CMOS fabrication process.

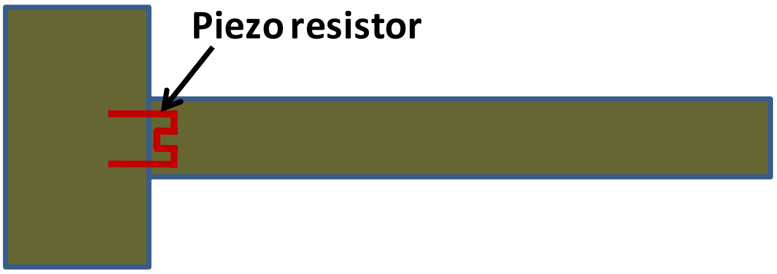

Fig. 2.12. Piezo resistor embedded near the fixed end of microcantilever sensor.

(iv) Piezoelectric method

Certain anisotropic materials exhibit piezoelectricity, which has been widely used in cantilever sensors for detection of deflection (Fig. 2.13). It is well known that, a mechanical stress generates an electrical potential across a piezoelectric material and vice versa. Piezoelectric read-out is primarily utilized in resonance mode operation. Piezoelectric read-out has the advantage of being easily scalable and has low power consumption. The disadvantage of this technique is that most piezoelectric materials are difficult to work with and they are not compatible with silicon processing technology [69].

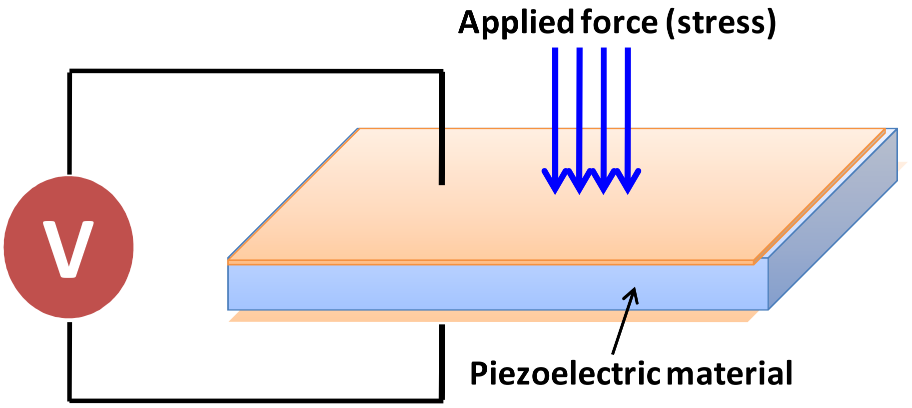

Fig. 2.13. An illustration of the piezoelectric effect; applied force generate a voltage across the electrodes.

(v) Capacitive method

In this detection method, the cantilever acts as one of the parallel plates of a capacitor as depicted in Fig. 2.14. As the cantilever deflects due to applied force or stress, the distance between the two plates changes, which in turn changes the capacitance of the system. If the length of the cantilever is much larger than its distance from the bottom plate, the capacitance is given by [81]:

$$C(z) = \frac{\epsilon_0 A}{d \Delta z} \tag{2.27}$$

where ϵ_0 is the permittivity in vacuum, A is the area of the plates, d is the gap between them and Δz is the vertical displacement of the cantilever from its initial position. The advantage of capacitive detection method is the simplicity of the associated electronics. This technique is not popular because the effective dielectric constant of the medium surrounding the electrodes is unstable, especially when the parallel electrode plates are in close proximity.

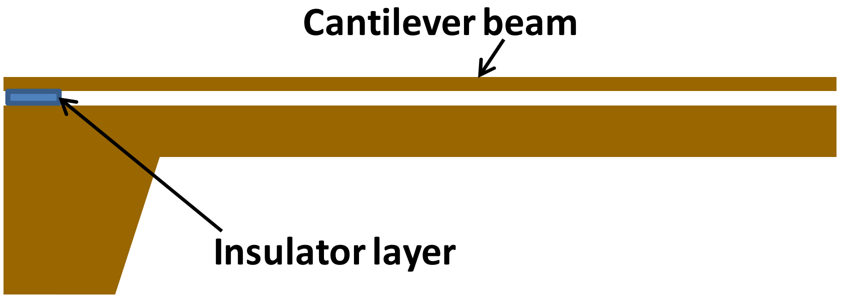

Fig. 2.14. Schematic of capacitive microcantilever.

2.5 Overview of the MUMPs process

MUMPs is a commercial program that provides cost-effective, proof-of-concept MEMS fabrication to research laboratories and industries. This process uses structural micromachining of multiple thin film layers. The MUMPs process which is adapted for the fabrication of microstructures, is an electroplated nickel micromachining process. The process was originally developed for the fabrication of MEMS micro-relay devices based on a thermal actuator technology [38]. Figure 2.15 depicts the cross section of a micro-relay fabricated with the MUMPs process. This process has the following general features:

(i) Electroplated nickel is utilized as the primary structural material and electrical interconnections.

(ii) Resistors, additional mechanical structures, and / or cross-over electrical routing are realized using doped poly silicon.

(iii) Silicon nitride is used as structural or electrical isolation layer.

(iv) Phospho-silicate glass (PSG) layer is employed as sacrificial layers.

(v) For additional thermal and electrical isolation, a trench layer in the silicon substrate can be incorporated.

(vi) Gold over-plate can be used to coat the sidewalls of nickel structures to achieve low resistance contacts.

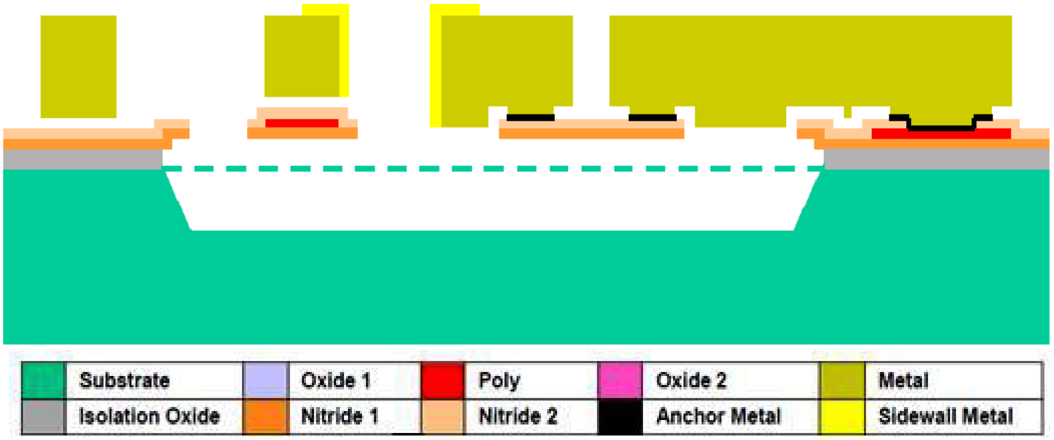

Fig. 2.15. Cross section of a micro-relay fabricated with the MUMPs process [38].

The process is designed to be as general as possible in order to support many different designs on a single silicon wafer. Since the process was not optimized for the fabrication of any one specific device, the thicknesses of the structural and sacrificial layers are chosen to suit most users and the layout design rules were chosen conservatively to guarantee the highest yield possible [38]. The electrical and mechanical parameters of various layers are given in Table 2.4. The process flow is listed in Table 2.5 and is described below using the naming convention for the various layers.

Table 2.4. Electrical and mechanical parameters of MUMPs process layers [38].

Film	**Thickness, nm**			**Residual Stress, MPa**			**Resistance, Ω/□**		
	Min.	**Typ.**	**Max.**	**Min.**	**Typ.**	**Max.**	**Min.**	**Typ.**	**Max.**
Isolation Oxide	1900	2000	2100		N/A			N/A	
Oxide 1	450	500	550		N/A			N/A	
Nitride 1	315	350	365	0	90	180		N/A	
Poly 1	630	700	770		N/A		19	22	25
Nitride 2	315	350	365	0	90	180		N/A	
Oxide 2	990	1100	1210		N/A			N/A	
Anchor Metal	32	35	38		N/A		--	7	--
Plating Base	495	550	605		N/A			N/A	
Metal	17000	20000	23000	--	100	--	--	8 µΩ	--
Sidewall Metal	1000	2000	3000		N/A			N/A	
Trench	N/A	25000	N/A		N/A			N/A	

(i) Substrate – The substrate is a high resistivity (> 4000 Ω-cm) n-type (100) silicon wafer.

(ii) Isolation oxide – A 2 µm thick silicon dioxide is deposited on the wafer surface which provides electrical isolation from the substrate.

(iii) Oxide 1 – This is a 0.5 µm thick PSG sacrificial layer, which is lithographically patterned with the first mask level, OXIDE1 and etched. Oxide 1 also defines the regions below which the silicon trench will be formed.

Table 2.5. Various processing steps of MUMPs [38].

S. No.	**Step name**	**Layer name**	**Material**	**Thickness, µm**	**Mask name**	**Photo-resist**	**Depth, µm**
1.	Substrate n-type (100) si	Substrate	Silicon	50	GND		
2.	KOH wet etch				Oxide 1	-	25
3.	Thermal oxidation	Isolation oxide	Thermal oxide	2			
4.	Release HF etch				Oxide 1	-	
5.	PDG deposition	Oxide 1	PSG	0.5			
6.	Wet etch				Oxide 1	+	
7.	LPCVD	Nitride 1	Si_xN_y	0.35			
8.	LPCVD	Poly	Polysilicon	0.7			
9.	RIE etch				Poly		
10.	RIE etch				HolePoly		
11.	LPCVD	Nitride 2	Si_xN_y	0.35			
12.	RIE etch				NitrHole	-	0.7
13.	PDG deposition	Oxide 2	PSG	1.1			
14.	Wet etch				MetAnch	-	
15.	Lift-off step 1	Anchor metal Cr	Chromium	0.01			
16.	Lift-off step 2				MetAnch	+	
17.	Lift-off step 1	Anchor metal Pt	Platinum	0.025			
18.	Lift-off step 2				MetAnch	+	
19.	Electroplating	Metal	Nickel	20			
20.	Stripping Resist Stencil				Metal	+	
21.	Stripping Resist Stencil				HoleMetal	-	
22.	Electroplating	Gold	Gold	0.5			
23.	Stripping Resist Stencil				Metal	+	
24.	Stripping Resist Stencil				HoleMetal	-	

(iv) Nitride 1 – This is a blanket layer of low-stress silicon nitride film (0.35 µm). The combination of Nitride 1 and Nitride 2 (deposited after Poly layer) provides protective encapsulation of the polysilicon, mechanical linkage between released metal structures, which should be electrically isolated and serves as a structural layer for beams, cantilevers, etc.

(v) Poly – This layer is 0.7 µm implant-doped polysilicon film. The Poly layer is patterned with the second mask level, POLY and etched. This layer can be used to form electrical cross-over routing, resistor elements or mechanical structures. .

(vi) Nitride 2 – This is a second layer of 0.35 µm thick low-stress silicon nitride. Nitride 1 together with Nitride 2 are lithographically patterned with the third mask level, NITRHOLE and etched.

(vii) Oxide 2 – This second sacrificial PSG oxide layer (1.1 µm) is removed at the final release step to free the metal mechanical layer. Oxide 2 is patterned with the fourth mask level, METANCH and is wet chemically etched.

(viii) Anchor Metal – The METANCH mask also provides the patterning for the metal structure anchors. A liftoff process leaves behind the layers of Chromium (Cr) and Platinum (Pt) only at the bottom of the Oxide 2 anchors.

(ix) Plating Base – A blanket layer of 500 nm of Copper (Cu) protected with a thin Titanium (Ti) layer serves as the 'Plating Base', which provides electrical continuity across the wafer for the subsequent metal electroplating step.

(x) Metal - The fifth mask level, METAL forms a patterned stencil for the electroplated metal layer. Metal layer consists of 20 µm of nickel followed by 0.5 µm gold layer. This bi-metal layer serves as the primary mechanical structure as well as the electrical interconnect layer.

(xi) Sidewall Metal – the sixth mask level, GOLDOVP is used for the electroplating of 1-3 µm gold layer on selected areas of the sidewall of the metal structures. This provides reliable low resistance electrical contact and helps to shrink the gaps between adjacent electroplated nickel structures.

(xii) The release of the microstructures involves a series of wet chemical etches to remove the Plating Base, sacrificial layers and the isolation oxide layer over the trench areas. Finally KOH is used to etch a 25 µm deep trench in the silicon substrate as defined by the OXIDE1 and NITRHOLE masks.

(xiii) Finally, the wafers are diced (sub-dicing is optional) in to 1 cm × 1 cm chips and shipped to the users.

A number of structures have been reported based on the above MUMPs process involving metal relays, gyroscopes, inductors, tunable capacitors, voltage doubler, etc. [82 - 86]. As on date, structures for gas sensing system have not been explored using this MUMPs process. This research work is exploiting the MUMPs process for the design and fabrication of micro-hotplates and microcantilevers for gas sensing applications.

2.6 Overview of MEMS design tool

Simulation prior to fabrication is becoming increasingly important due to the highly integrated and interdisciplinary nature of MEMS systems. Using MEMS design tools, one can virtually build the device and predict its behavior. There are a number of MEMS simulation software viz – ANSYS, IntelliSuite, COMSOL, Coventorware, which are commercially available. They provide a seamless integrated design environment that reduces design risk, speeds time to market and lowers development costs. Various parameters of a MEMS device can be investigated and optimized in this simulation environment before actual device fabrication is undertaken [80]. Major components which influence the MEMS design are the materials, processes and the layout design. Typical design sequence involves:

(i) Selection of materials for various structural and sacrificial layers.
(ii) Selection of fabrication process sequence for deposition, doping, patterning, etc.
(iii) Creation of two dimensional layouts for various layers and structures.
(iv) Generating a 3D model to visualize the complete structure.

(v) Meshing and FEM simulation by applying suitable boundary and loading conditions.

(vi) Repeating steps 3 to 5 till the desired results are achieved.

The software which is used for this research work is an integrated suite of software tools for designing and simulating MEMS and microfluidics devices. Typical design flow using the MEMS software is shown in Fig. 2.16. Usually the design cycle iteratively goes through two modules, namely the layout editor and the analyzer.

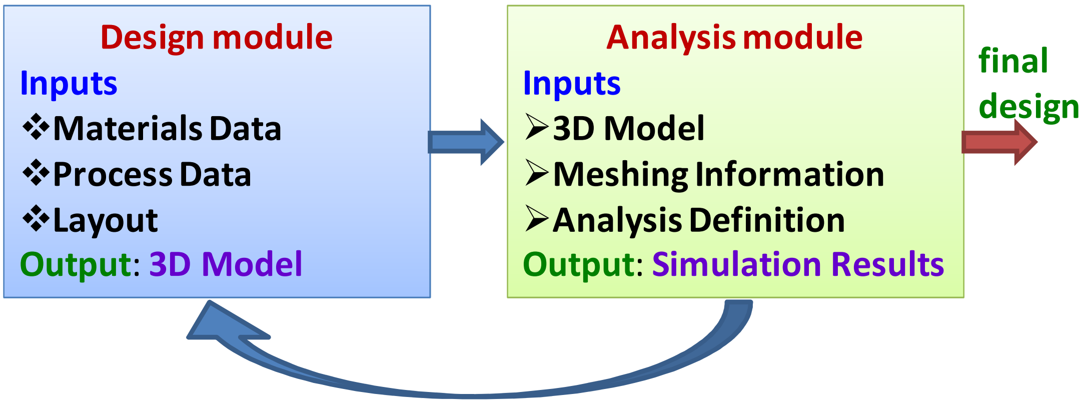

Fig. 2.16. Design and analysis cycle of MEMS system.

The design starts with the layout editor, which needs three inputs, namely (i) the properties of the materials to be used, (ii) the process sequence and (iii) the 2D layout. The material properties usually include dielectric strength, density, conductivity, thermal characteristics, etc., and are generally available as Material Properties Database (MPD). A material is selected for each of the deposit steps in the process. Simulation results depend on the physical and chemical properties of the materials that are used to build the model. The process sequence allows the users to create a flow, simulating the foundry process that will fabricate the MEMS design. Materials, layer names, mask names, actions (deposit or etch), thickness or etch depth, photoresist, etc., are defined in a series of steps in the process sequence. The choice of materials selected in the process flow is dependent on the MPD, which stores all the materials and their associated properties needed to fully characterize the process flow. In addition, the software can include several standard foundry design kits to facilitate the simulation of a design according to the specifications of the selected foundry. The kit contains parameters such as Poisson ratio, Young's modulus, layer thickness and stress gradient, which are defined within the tolerances of the specific manufacturing process. Thus the foundry kit automatically sets constraints for the materials and processes, which allow only those designs that are fully compatible with the manufacturing process. As the foundry process dictates the materials and the processes, the user has to design the 2-D mask layouts using the Layout Editor, which enables to create, import, view, and edit 2-D mask information. Using the layout, in conjunction with the layer stack information provided in the Process Editor, a 3-D solid model is built, which represents the MEMS structure.

The analyzer module has two major functions – meshing and analysis. Analyzer uses the 3-D model for mesh generation, where the geometry of the structure can be reduced to a group of simpler finite element bricks and presented to the solver for finite element analysis. According to the device geometry, various mesh elements such as tetrahedral, bricks and hexahedral can be chosen. Meshing must be refined enough to capture the details of stress and thermal gradients, current densities, displacement, etc of the MEMS structure. After a mesh has been generated, the a comprehensive suite of field solvers is used to simulate the physical behavior of MEMS devices using either the finite-element method (FEM) or boundary-element method (BEM) or, in the case of coupled electro-mechanics, a combination of the two methods. Various solvers available are electrostatic, mechanical, electromechanical, piezoelectric and thermo-mechanical solvers, including structural, modal, harmonic, stress and transient analyses. The outputs of the analyzer are examined for design and functional validation and the cycle is repeated to achieve the optimum results. Thus the MEMS design tool facilitates to explore the design concepts and perform detailed verification of device behavior.

CHAPTER 3: DESIGN AND SIMULATION OF MICROSTRUCTURES

This chapter describes the design and simulation studies carried out on the microhotplates and microcantilevers. Simulations results of electro-thermal, thermo-mechanical and piezo resistive analysis of various micro structures are discussed. The design of the microstructures is optimized based on the simulation results.

3.1 Microhotplates

Microhotplates are of one of the key components in MEMS based sensors for chemical, biological and environmental applications [87]. In chemical sensors, MHP is used to control the temperature of the sensing layer in order to optimize the sensitivity, selectivity and reversibility [88, 89]. Hotplates are the major power consuming elements apart from the readout electronics in sensor circuits. Thus, it is imperative that the MHPs need to be designed for low power consumption, good temperature uniformity and low thermal mass. MHPs usually consist of thermally isolated membrane with an integrated heater, contact electrodes for sensing layer and sometimes a temperature sensor to measure the hotplate temperature. Due to their small size, low power consumption, ease of packaging and possibility of integration with electronics, MHPs have attracted considerable attention in the field of gas sensors. This section covers the design and simulation studies of MHPs based on standard MUMPs for fabrication in a MPW run [38].

3.1.1 Design of MHPs using MUMPs process

Since the devices were being fabricated using MUMPs process, the layers and materials for the MHPs were dictated by the foundry. Using the available layer combinations, the following structures were designed.

(i) 3 different sizes of membrane –900 µm × 900 µm, 500 µm × 500 µm and 300 µm × 300 µm
(ii) 4 different geometries of embedded heater – serpentine, spiral, fan and S-shape

All the MHPs were suspended membrane type structures comprising of two nitride layers with a poly heater sandwiched in between. Each nitride layer was 0.35 µm thick and the poly layer was 0.7 µm thick. The membrane was suspended above the 25 µm deep trench. The anchoring layer of Chromium – Platinum (Cr-Pt) was used to form inter-digitated electrodes (IDE), on which the chemical sensing layer would be deposited. Figs. 3.1 to 3.3 show typical design layouts of various MHPs.

The heater dimensions were tailored to fulfill the following requirements:

(i) Operating temperature range from 350 - 750 K.
(ii) Maximum heater power consumption below 50 mW.
(iii) Heater efficiency better than 10 K / mW.
(iv) Good temperature uniformity on the active area ($\Delta T <= 10\%$ of T_{max}).

The schematic representation of the heater geometries used for the MHPs is shown in Fig. 3.1. The 2-D and 3-D model of the serpentine heater (900 µm × 900 µm) is shown in Fig. 3.2. The serpentine poly heater was embedded below the top nitride layer (top nitride layer is not shown). Fig 3.3 shows the 2-D and 3-D layouts of spiral and fan shape heaters (500 µm × 500 µm and 300 µm × 300 µm).

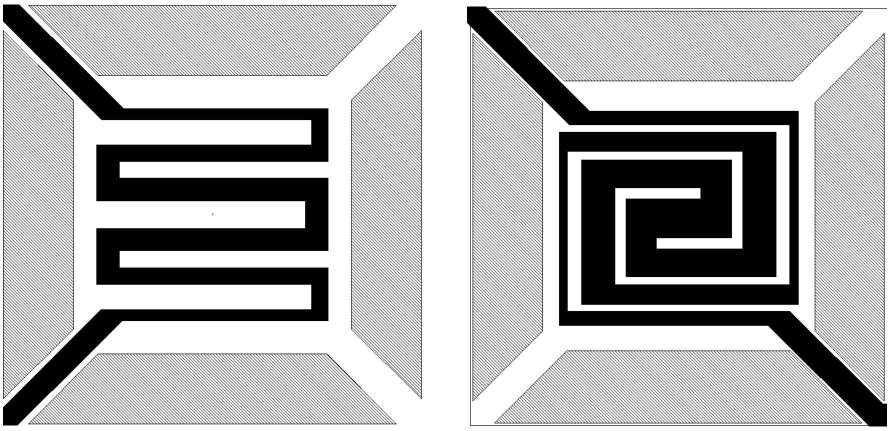

Serpentine **Spiral**

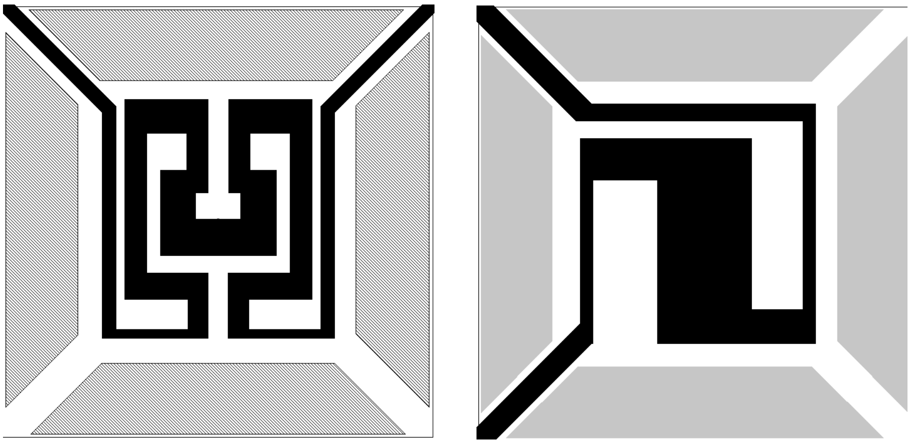

Fan **S-shape**

Fig. 3.1. Heater geometries used for the MHP design.

3.1.2 Electro-thermal simulation of MHPs

Spatial temperature uniformity is the most important requirement for any MHP. To achieve a desired temperature distribution, one needs to design the heater and membrane geometry carefully. Uniform temperature necessitates minimization of the heater “hot-spot”, which is a crucial requirement for heater reliability. The heated active area should be small with respect to power consumption, which contradicts the need for large active area to enable the

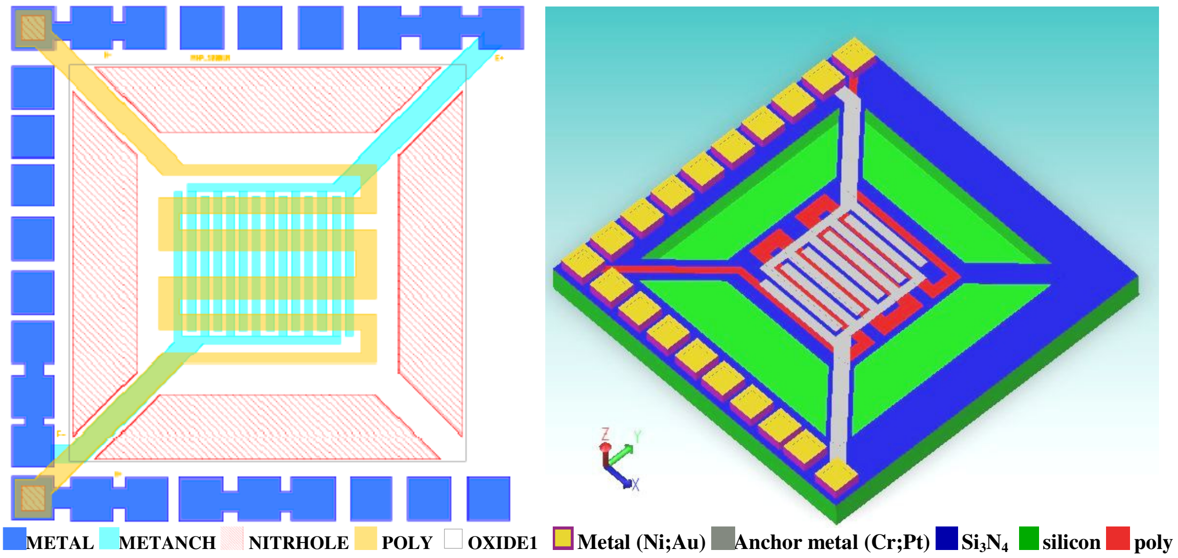

Fig. 3.2. 2-D layout and 3-D solid model of serpentine heater (900 µm × 900 µm); top nitride layer not shown in the 3-D model.

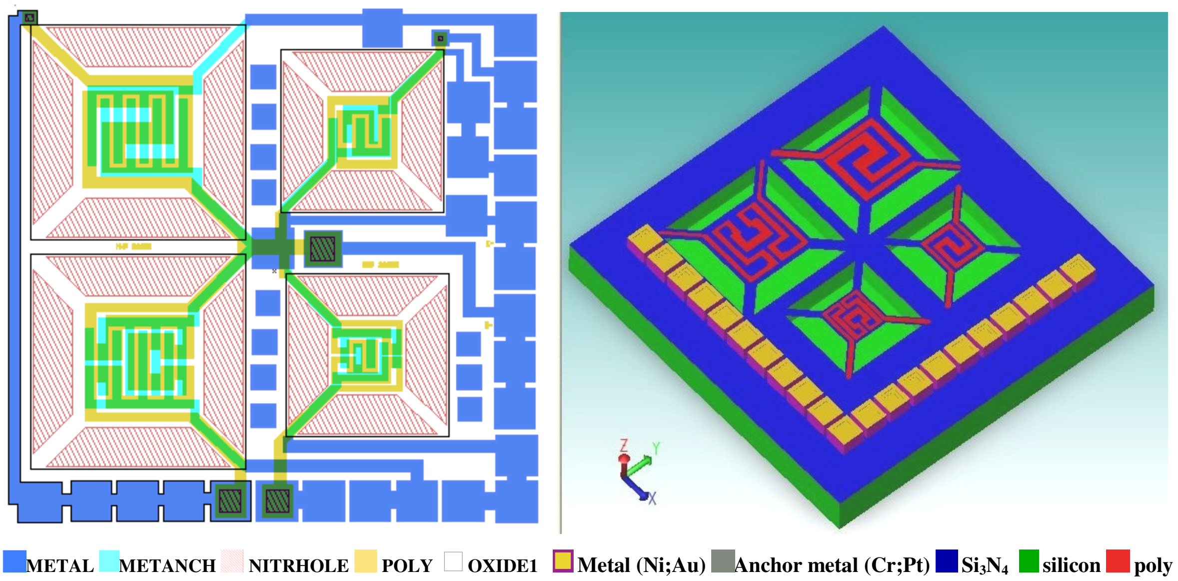

Fig. 3.3. 2-D layout and 3-D solid model of spiral and fan shape heaters (500 µm × 500 µm and 300 µm × 300 µm); top nitride layer and IDE are not shown in 3-D model.

measurement of the highly resistive sensing materials. Only large active areas having large length to width ratio of the electrodes allow reliable measurement of highly resistive MOX materials. On the contrary, the length to width ratio of suspension beams cannot be increased arbitrarily without compromising the mechanical stability and increasing the current density along the metal lines needed for electrical connection. A popular approach to obtain temperature homogeneity is to use high thermal conductivity films or silicon plugs underneath the membrane [90]. As the fabrication steps are predefined by the MUMPs process, two different solutions are used to obtain the best possible temperature distribution – using various heater geometries and varying the heater width to modulate the current density.

The heater geometries used are shown in Fig 3.1. Three different sizes of the membrane are used and the heater area is dependent on the membrane size. The 3-D solid models are meshed appropriately and electro-thermal simulation is carried out by applying potential across the heater connections. Following boundary conditions are applied to all MHPs unless specified:

1. Substrate is fixed i.e. no mechanical movement is allowed for substrate.
2. All the heater parts including the substrate are initialised to room temperature (300 K) at the beginning of the simulation.

The material properties used for the membrane and the heater are given in Table 3.1. Fig. 3.4 and 3.5 show the typical results of meshing, temperature profile, potential distribution and current density for the three different size MHPs for an applied heater potential of 5 V. At the beginning of this research work, conventional design of the heater geometries with constant current density was adapted. It was observed that heating of the active area with constant power per area, resulted in a non-homogeneous temperature profile. From the analysis in section 2.5, it is clear that the inner part of the heated membrane endures heat losses only to the ambient air and radiation, while the outer part additionally suffers from heat losses through

Table 3.1. Material properties used for FEM simulation of MHPs.

Properties	Silicon Nitride	Poly Silicon
Resistance, Ω/sq	-	19 - 25
Young's Modulus, GPa	245	158
Poisson ratio	0.23	0.22
Density, kg/m^3	3187	2330
Thermal Expansion Coefficient, K^{-1}	2.25e-6	2.7e-6
Thermal Conductivity, W/m-K	2.25	32

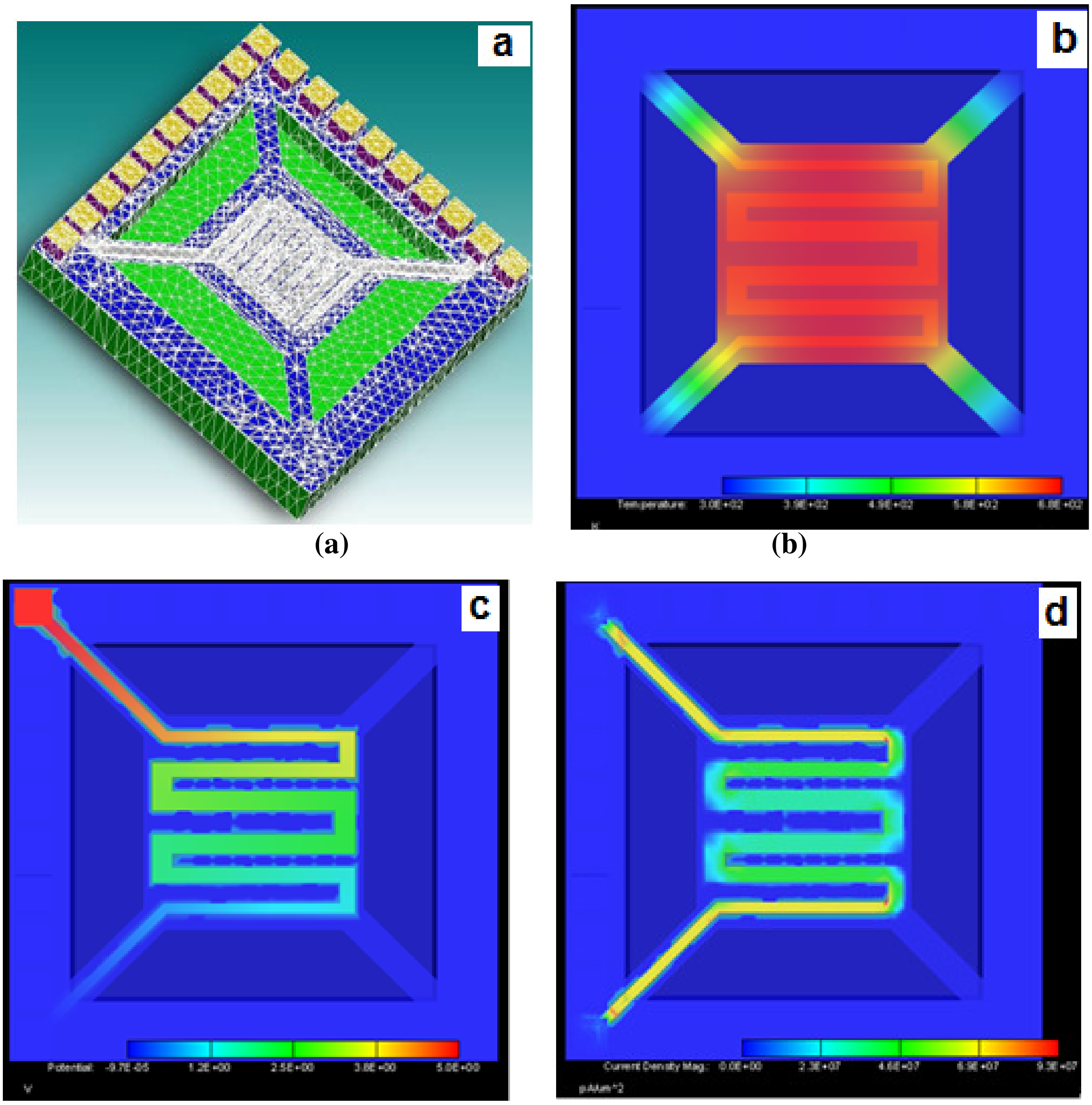

(a) **(b)**

(c) **(d)**

Fig. 3.4. (a) Meshing, (b) temperature profile, (c) potential distribution and (d) current density of non-uniform serpentine heater for an applied heater voltage of 5 V (Membrane size is 900 μm × 900 μm).

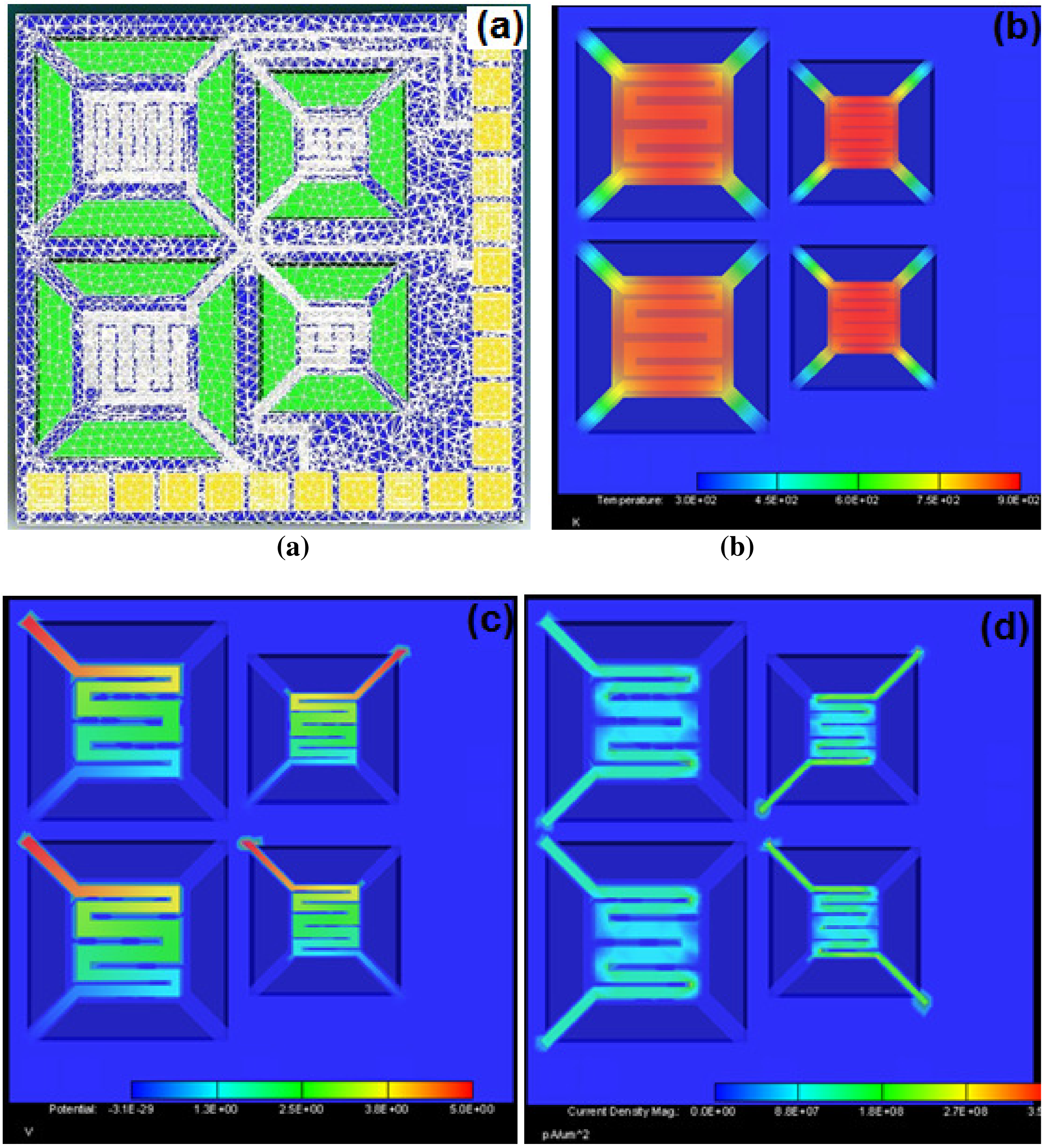

(a) (b)

(c) (d)

Fig. 3.5. (a) Meshing, (b) temperature profile, (c) potential distribution and (d) current density of non-uniform serpentine heater for an applied heater voltage of 5 V (Membrane sizes are 500 μm × 500 μm and 300 μm × 300 μm).

the membrane suspension beams. This causes the borders of the active area to be colder than the inner part. In order to improve the temperature homogeneity, the width of the poly heater is progressively increased towards the centre from the edges. Thus by controlling the current density, the heater design is optimized to obtain temperature uniformity better than 10 % over the surface comprising the IDE (~ 800 μm × 800 μm in Fig. 3.4). As can be seen from Figs. 3.4 and 3.5, the complete MHP is heated uniformly except near the beams, which are anchoring the MHP to the substrate. The suspended membrane provides good thermal isolation between the substrate and the gas sensitive heated area, resulting in substantial reduction of heater power. The whole substrate remains nearly at ambient temperature. The current densities are kept $< 1 - 10 \times 10^{9}$ Am^{-2} for all the heaters. Beyond this electromigration effects have been reported with accompanying resistance changes attributed to redistribution of dopant species [91].

The comparison of the results with the uniform (constant current density) and non-uniform heater structures for various heater geometries are given in Fig. 3.6 and in Table 3.2. From Table 3.2, it is seen that non-uniform structures offer better temperature homogeneity and power efficiency at the same time the power consumption is kept low (<10 mW). Such improvement in heater temperature profile with non uniform resistance structure has been reported earlier [92]. Among the four different heater geometries, non-uniform spiral shape heater has offered the best temperature uniformity over the sensing area with high power efficiency for a heater power of ~8 mW. Fig. 3.7 shows the average maximum temperature of the four MHPs as a function of applied voltage and applied power. For temperature up to 700 K, the temperature – power relationship is linear as expected and reported earlier [40, 48, 49].

Similar studies are carried out for (300 μm × 300 μm) and (500 μm × 500 μm) MHPs with various heater structures. The temperature profile over the active area for these MHPs is presented in Fig. 3.8. As can be seen, the temperature is within ± 8% of maximum

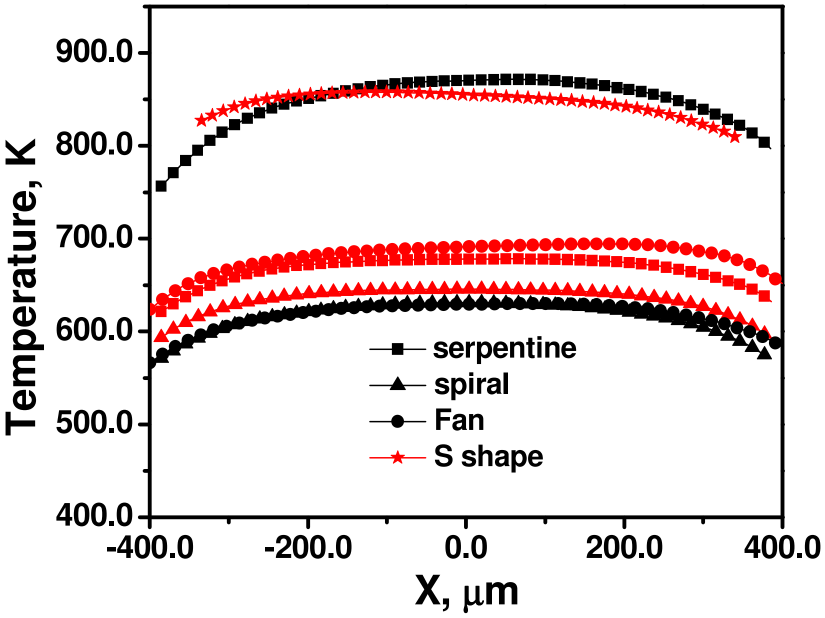

Fig. 3.6. Comparison of temperature profile of 900 µm × 900 µm MHPs with uniform (black) and non-uniform (red) heater structures (heater voltage = 5V).

Table 3.2. Temperature characteristics of 900 µm × 900 µm MHP structures (heater voltage = 5V).

Heater type	Power, mW	Max. temperature, T_{max}, K	Temp. deviation from T_{max}, %	Power efficiency, K/mW
Uniform Serpentine	15.53	872	13.3	36.83
Non uniform Serpentine	9.57	678	8.26	39.5
Uniform Spiral	8.9	631	9.5	37.19
Non uniform Spiral	8.56	646	8.06	40.42
Uniform Fan	8.11	629	10.1	40.56
Non uniform Fan	10.37	694	10.08	38.05
S shape	16.35	882	7.2	35.57

temperature in the active area. Fig 3.9 shows the temperature as a function of heater voltage and heater power for all three sizes of MHP. All MHPs show a power efficiency of ≥ 10 K/mW for temperature up to 650 K. Using the analytical eq. (2.3), the conduction losses are estimated at 0.83, 0.78 and 0.63 mW for (900 µm × 900 µm), (500 µm × 500 µm) and (300 µm × 300 µm) MHPs respectively. This shows that less than 10% of the power is dissipated through conduction and ~90% of the power is used for efficient heating of the membrane. Among the three sizes, the smallest MHP exhibits the highest efficiency as the heating area is smaller and the length-to-width ratio of suspension beams is more compared to other MHPs.

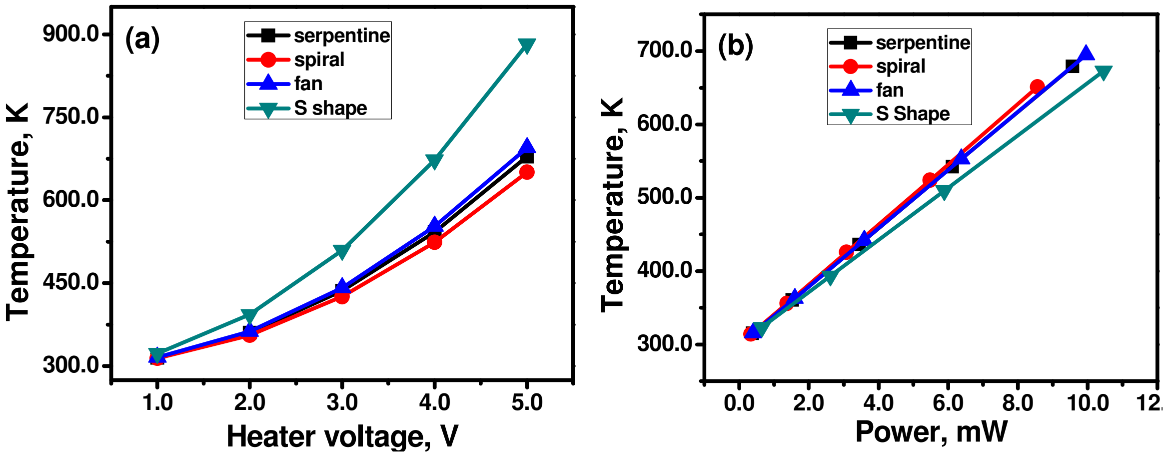

(a) (b)

Fig. 3.7. Temperature characteristics of different MHPs (900 µm × 900 µm) as a function of applied (a) heater voltage and (b) heater power.

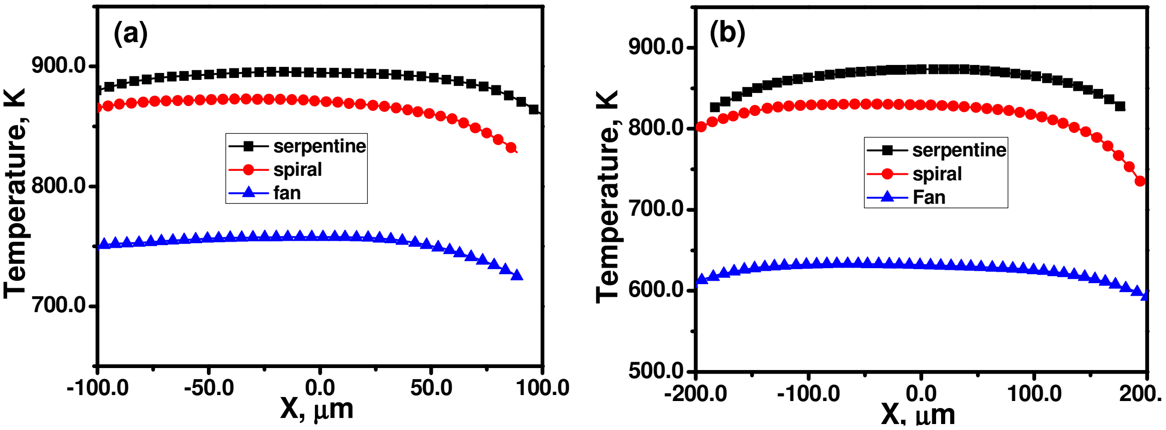

(a) (b)

Fig. 3.8. Temperature profile of (a) 300 µm × 300 µm and (b) 500 µm × 500 µm MHPs (heater voltage = 5V).

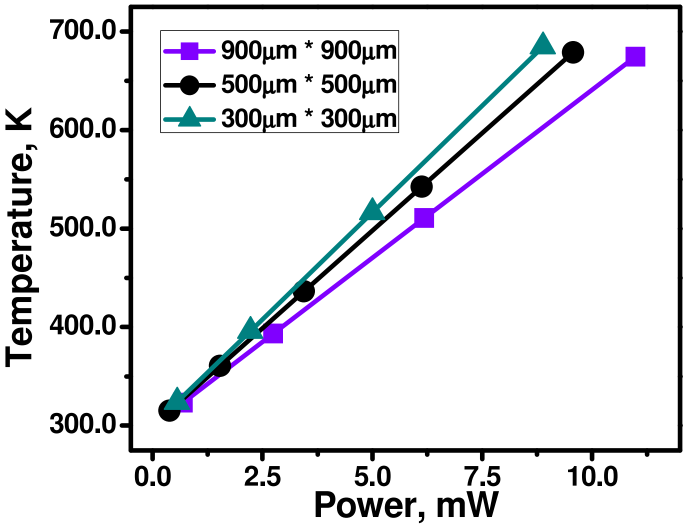

Fig. 3.9. Comparison of power efficiency of various sizes of MHP.

3.2 Design and simulation studies of microcantilever structures

Microcantilevers are the simplest and most widely used MEMS structure, especially for chemical and bio-sensing applications [78, 93]. The most common and well established application of microcantilevers is in atomic force microscopy (AFM) for the topography imaging of non-conductive surfaces. In the past decade, microcantilever based sensors have proved to become a versatile transduction platform for physical parameters, chemical, volatile organic molecules, explosives and biomolecule detection. These sensors have several advantages namely high sensitivity, low cost, simplicity, low analyte requirement (in µg/µl), non-hazardous procedures and fast response. Microcantilevers are extremely sensitive to surface processes owing to their large surface area to mass ratio. The basic principle of microcantilever based sensors is the analyte induced surface stress generation, which leads to change in the resonant frequency (dynamic or resonant mode operation) and deflection due to differential surface stresses (static mode operation) [62, 74]. This section presents the design of various types of microcantilevers and their simulation results.

3.2.1 Design of microcantilevers

As MUMPs process was adopted for fabrication, the layers and materials for the microcantilever design were governed by the foundry. Using the available layer combinations, the following structures were explored.

(i) Rectangular microcantilevers with various length and width
(ii) Rectangular microcantilevers with embedded heater and piezo resistor
(iii) U and V shaped microcantilevers

The cross-sectional view of various layers used for the design of piezoresistive microcantilevers is shown in Fig.3.10. As shown in Fig. 3.10, the rectangular microcantilever was designed using two silicon nitride structural layers of 0.35 µm each. The poly heater (0.7 µm) was sandwiched between two nitride layers. Though poly was a better choice for piezo

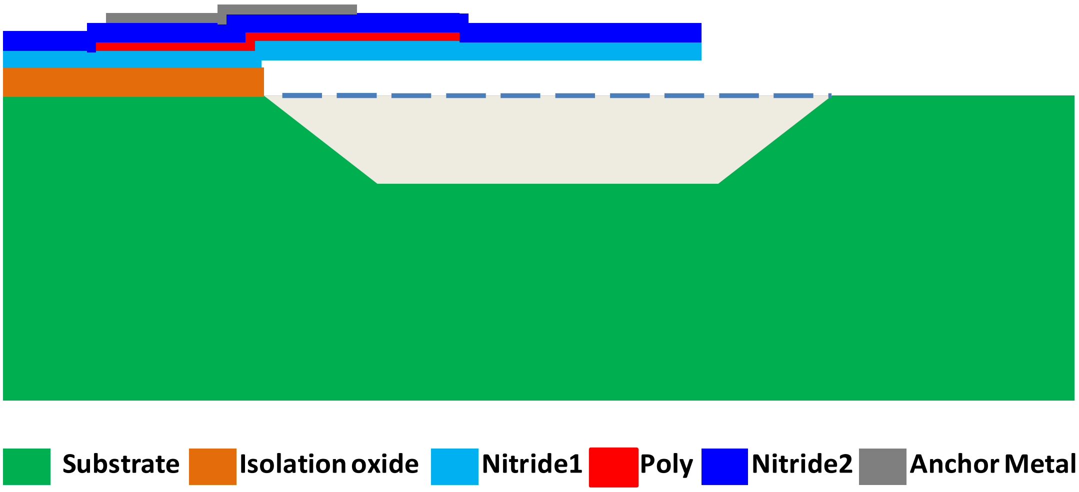

Fig. 3.10. Cross-sectional view of the structural layers of piezoresistive microcantilever.

resistor, it could be placed only in the neutral axis of the nitride cantilever. Hence, poly was used as a micro heater to provide thermal activation for the physisorbed / chemisorbed species interacting with the sensing layer. The metal layer comprising of Chromium - Platinum, which was meant for anchoring the Nickel-Gold metal structures, was used to form piezo resistors. Nickel – Gold layer was used for interconnections and contacts.

For electro-thermo-mechanical simulations, the solid models of the microcantilevers are appropriately meshed as shown in Fig. 3.11. The material properties used for simulations are given in Table 3.3. The FEM simulation of the designed microcantilevers is divided into four parts and discussed individually in the next sections.

3.2.2 Simulation studies of microcantilevers

3.2.2.1 Mechanical analysis

Geometrical dimensions of the microcantilevers play an important role in both static and dynamic modes of sensor operation [71] as can be seen from eqs. (2.14) and (2.21). As shown in Fig. 3.10, the main cantilever structure comprises of two Si_3N_4 layers in all cases with a total thickness of 0.7 µm. As the thickness is fixed, only the lateral parameters (e.g. length and width in case of rectangular cantilever) are varied for all cantilevers. Mechanical analysis is performed at room temperatures by applying nominal load on the top surface of the microcantilever. The following boundary conditions are applied for all simulations unless specified otherwise.

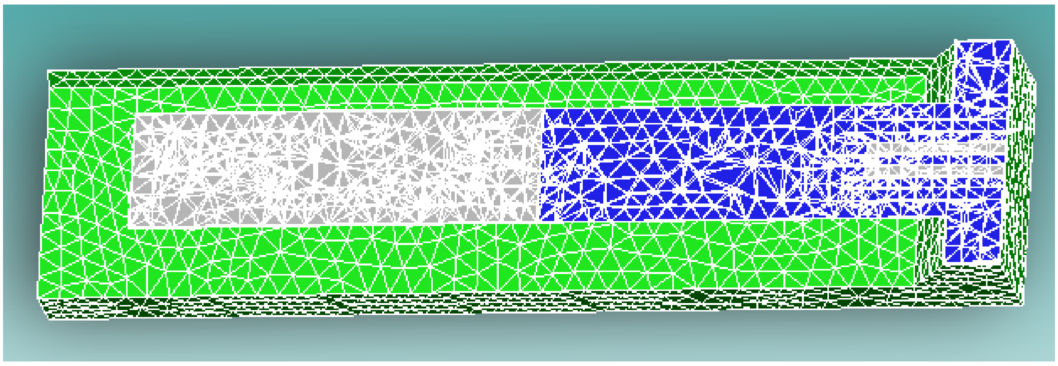

Fig. 3.11. Typical meshing of microcantilever for FEM analysis.

Table 3.3. Material properties used for FEM simulation of microcantilevers [38].

Properties	Silicon Nitride	Poly Silicon	Cr film	Pt film
Resistance, Ω/sq	-	19 - 25	7	7
Residual Stress, MPa	90 - 180	-	-	-
Young's Modulus, GPa	245	158	279	168
Poisson ratio	0.23	0.22	0.21	0.38
Density, kg/m^3	3187	2330	7200	21400
Thermal Expansion Coefficient, K^{-1}	2.25e-6	2.7e-6	4.9e-6	Look up table
Thermal Conductivity, W/m-K	2.25	32	90.3	71.6

(i) The substrate will remain stationary all the time.

(ii) The fixed end of the microcantilever, which is attached to the substrate, will remain stationary all the time.

(iii) The applied load is uniformly distributed on the surface of the cantilever and the surface stresses are induced in the *X–Y* plane.

Fig. 3.12, Fig. 3.13 and Fig. 3.14 show the plots for deflection and first modal frequency with applied load as a function of cantilever width (20, 30 and 50 µm) and length (50 to 450 µm).

As the length increases, the deflection magnitude also increases in compliance with eq. (2.14), as it is proportional to the square of length. There is no significant change in modal frequency with load as (t « L).

Fig. 3.15 summarizes the results of deflection and resonant frequency as a function of cantilever geometry for an applied load of 1 Pa on the cantilever surface. As can be seen from

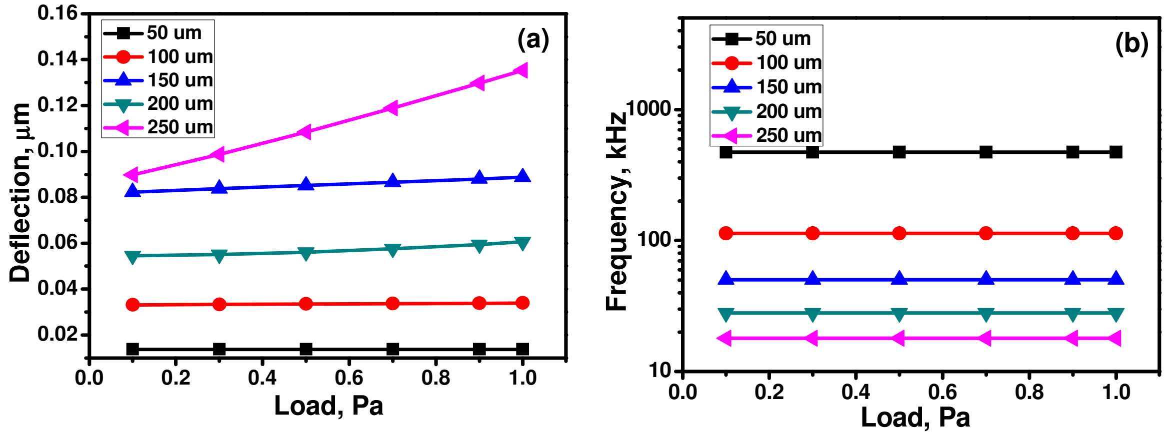

(a) (b)

Fig. 3.12. (a) Deflection and (b) resonant frequency vs applied load as a function of length of rectangular microcantilever (width = 20 µm).

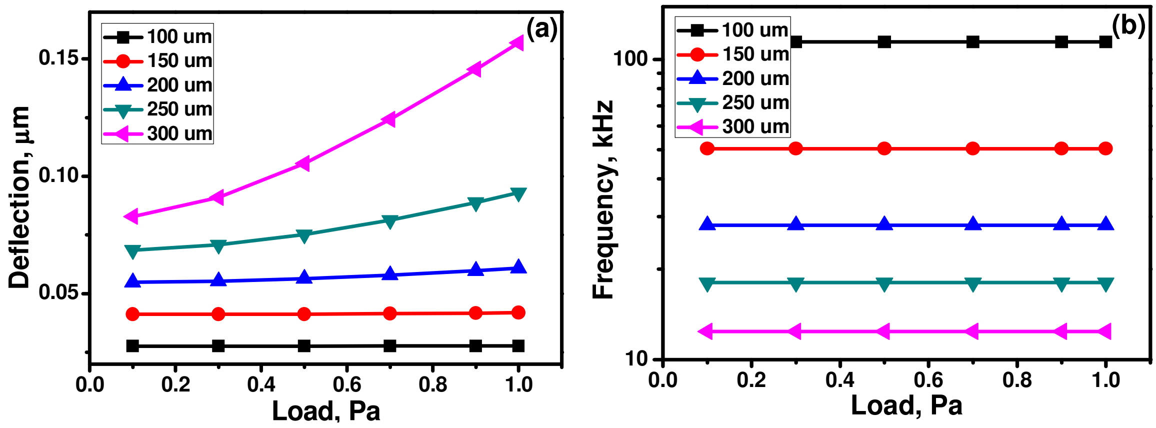

(a) (b)

Fig. 3.13. (a) Deflection and (b) resonant frequency vs applied load as a function of length of rectangular microcantilever (width = 30 µm).

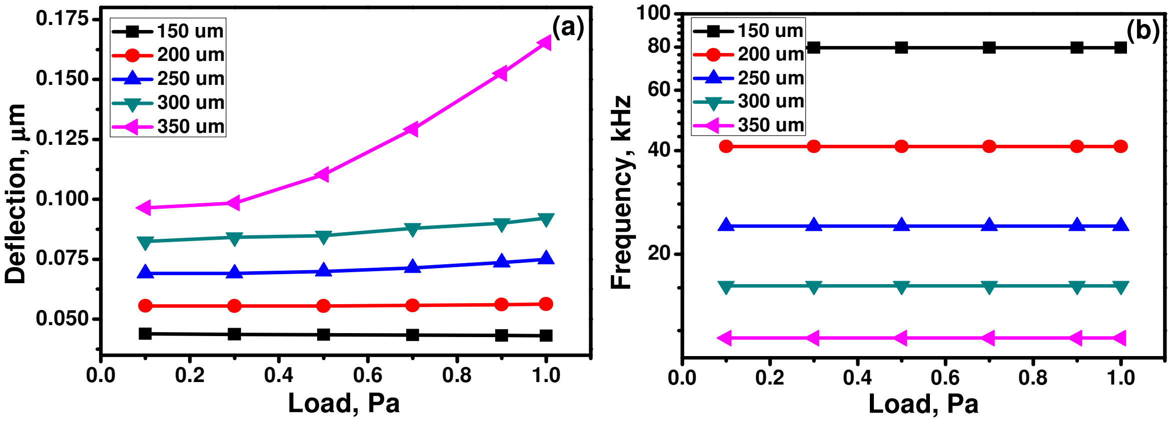

(a) (b)

Fig. 3.14. (a) Deflection and (b) resonant frequency vs applied load as a function of length of rectangular microcantilever (width = 50 µm).

equations (2.14) and (2.21), the inverse relationship between the deflection and resonant frequency poses a contradictory requirement of L and t. Any attempt to increase the deflection by increasing the length or decreasing the thickness (which is not allowed in MUMPs) will decrease the resonant frequency. From the simulation results, it is apparent that optical deflection method is more sensitive compared to resonant frequency method due to the limitation of cantilever thickness.

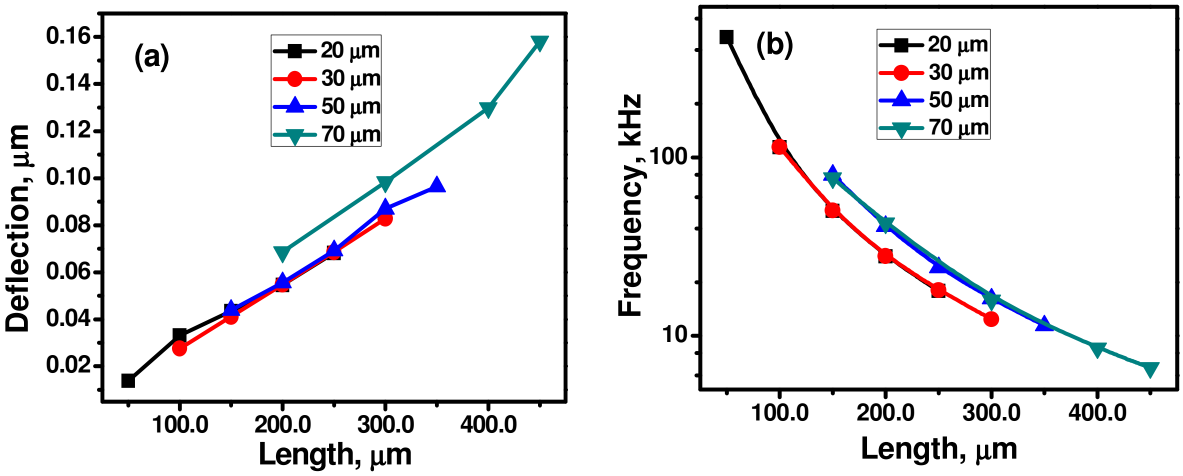

(a) (b)

Fig. 3.15. (a) Deflection and (b) resonant frequency vs length of rectangular micro-cantilever for an applied load of 0.1 Pa. (microcantilever width is given in the inset).

Simulations are carried out on V and U shaped cantilevers (having two different lengths) to evaluate the deflection sensitivity. The results are compared with the conventional rectangular cantilever. One set of results is presented in Fig. 3.16. For the dimensions mentioned in Fig. 3.16, the deflection vs load plot and deflection contours show that the U-shape cantilever has better deflection sensitivity and linear response over the conventional rectangular microcantilever [93, 94].

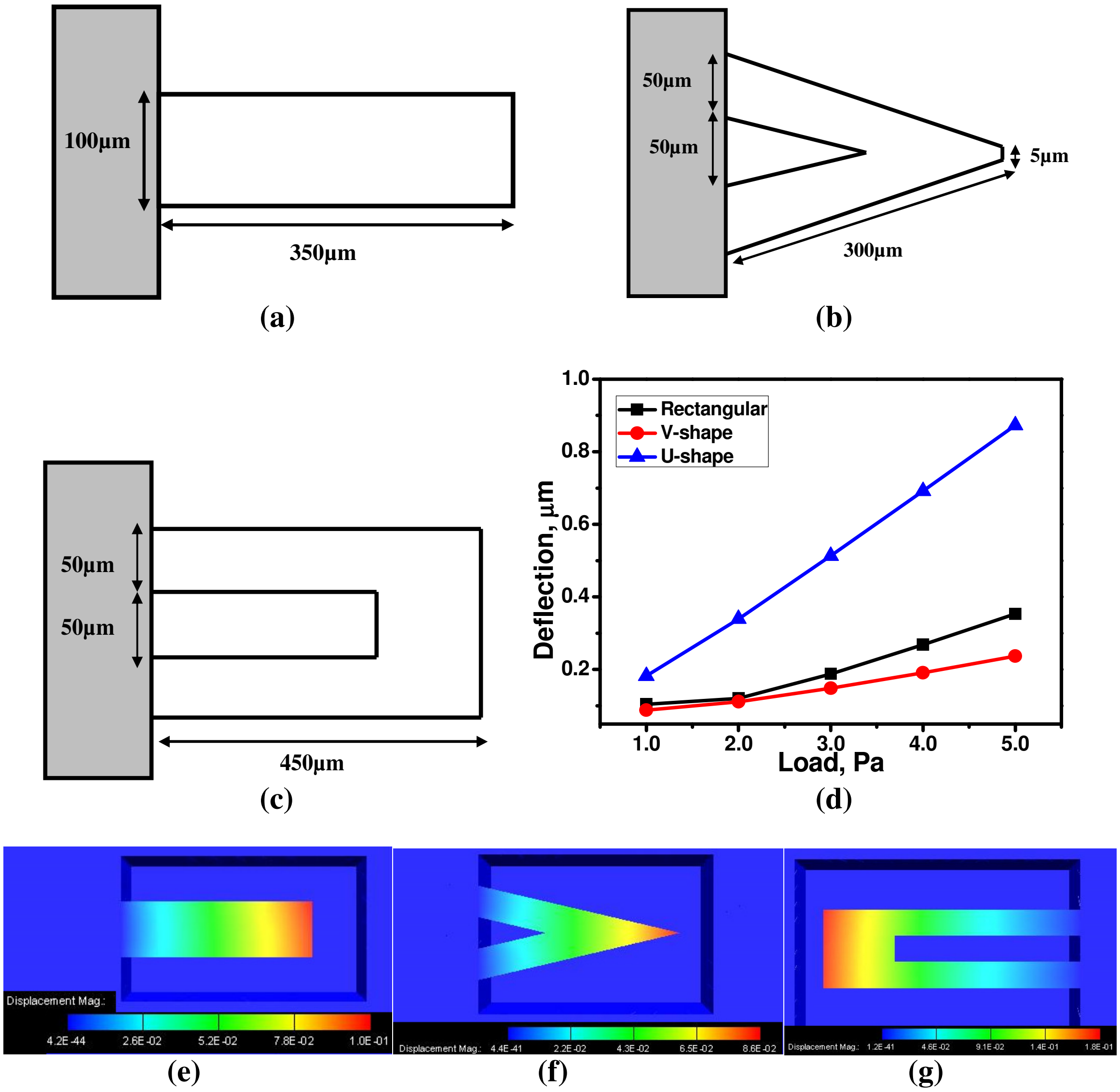

Fig. 3.16. Schematic representation of (a) rectangular, (b) V-shape and (c) U-shape microcatilevers; (d) comparison of deflection vs load; (e), (f) and (g) are deflection contours of (a), (b) and (c) for an applied load of 1Pa.

3.2.2.2 Electro thermal analysis of embedded microheater

Microcantilever with integrated heaters has been used for calorimetry, materials characterization and data storage applications [95]. Recently microcantilevers with integrated heater have gained attention especially for gas sensor applications, where the thermal energy is exploited to achieve selectivity and reversibility. The requirements of microheaters are elaborated in Chapter 2. In order to heat the microcantilevers for gas sensing applications, poly heater is embedded in some of the structures. Electro-thermal analysis of these buried heaters is carried out by applying DC voltage of up to 5 V. Following boundary conditions are applied unless specified;

(i) Substrate is fixed i.e. no mechanical movement is allowed for the substrate.

(ii) All the heater parts including the substrate are initialised to room temperature (300 K) at the beginning of the simulation.

Fig 3.17 shows the temperature profile of various microcantilevers for an applied heater voltage. Depending on the temperature requirement, the voltage is varied from 1 to 5 V. As can be seen from the figure, > 75% of the cantilever area is heated uniformly (< 15% variation from the peak temperature). The suspended part of the heated area experiences heat losses only to the ambient air and radiation, whereas the fixed end additionally suffers from heat losses through conduction to the substrate. The heater power is less than 15 mW at the desired maximum temperature in all cases owing to the small area of microcantilevers. It is observed that for temperature up to 700 K, the temperature – power relationship is linear as in the case of MHPs.

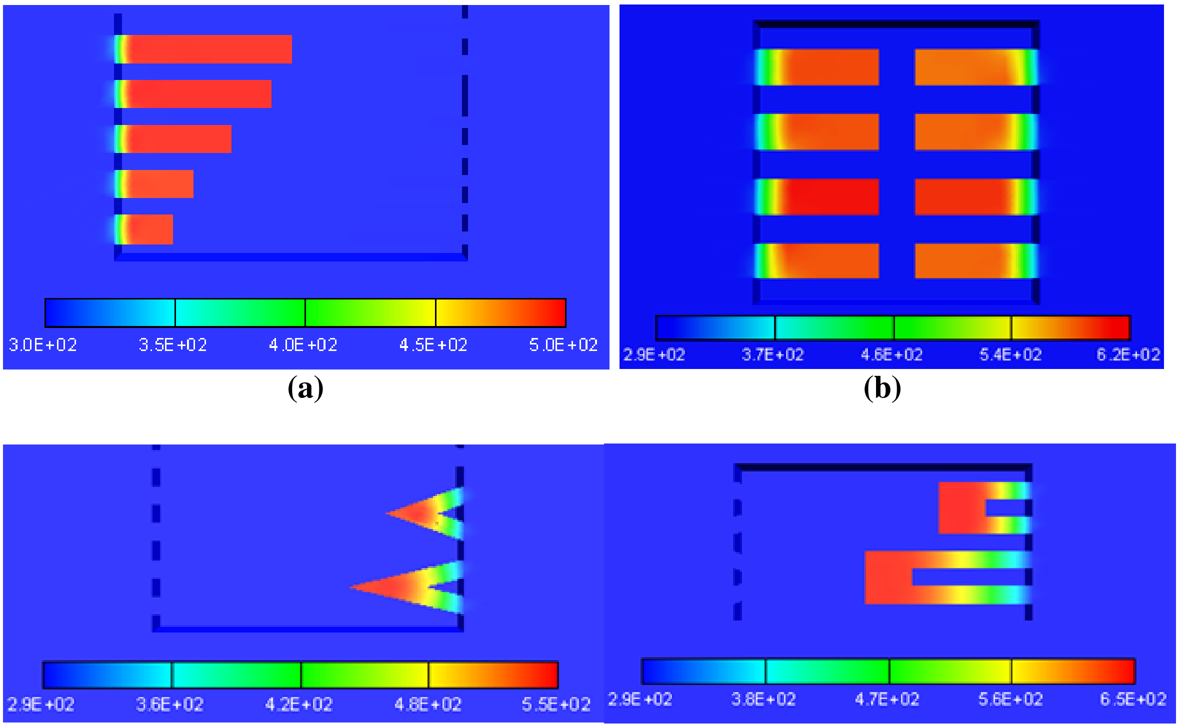

(a) **(b)**

(c) **(d)**

Fig. 3.17. Temperature profile of (a) cantilevers of various length (width = 70 μm) at 3 V; (b) 350 × 100 μm cantilevers with various heater geometries at 5 V; (c) and (d) V and U shape cantilevers at 3 V (for the smaller cantilever) and 3.5 V(for the bigger cantilever).

3.2.2.3 Thermo-mechanical analysis

Simulation of induced surface stress of the microcantilever is carried out for various surface loads and temperatures by thermo-mechanical analysis. The FEM simulator requires the stress at the surface of the microcantilevers in *X*-*Y* directions to be specified in MPa. The input values of the stress are chosen accordingly to match reported data in literature [66] for the cantilever displacement. The tip displacement of the cantilever varies in accordance with the applied stress at the surface during the chemical detection process. To simulate the thermal activation and adsorption of chemical species, the cantilever surface is kept constant at a fixed temperature and a nominal load is applied on the microcantilever surface. The results of thermo-mechanical and piezo resistive simulations for the 350 μm × 100 μm rectangular microcantilever are presented here. The following boundary conditions are applied unless specified;

(i) Substrate is fixed i.e. no mechanical movement is allowed for substrate.

(ii) Top surface of the microcantilever is applied with the temperature value of interest.

(iii) Substrate temperature is kept constant at 300 K.

Typical Mises stress and deflection contour of the microcantilever are shown in Fig. 3.18 for an applied load of 0.1 Pa at room temperature. The maximum stress is concentrated at the fixed end (i.e. $x = 0$) as derived in eqs. (2.8) and (2.9). Fig. 3.19 shows the microcantilever deflection at different loads as a function of surface temperature. It is seen that as the applied load increases, the displacement tends to become non-linear with temperature. In order to get a linear response, the maximum displacement is usually restricted to < 20 % of the microcantilever thickness. In practical applications, the surface stress is calculated from the cantilever deflection, but it is difficult to determine surface stress from molecular adsorption as the physical parameter and the processes involved are rather complex and unknown.

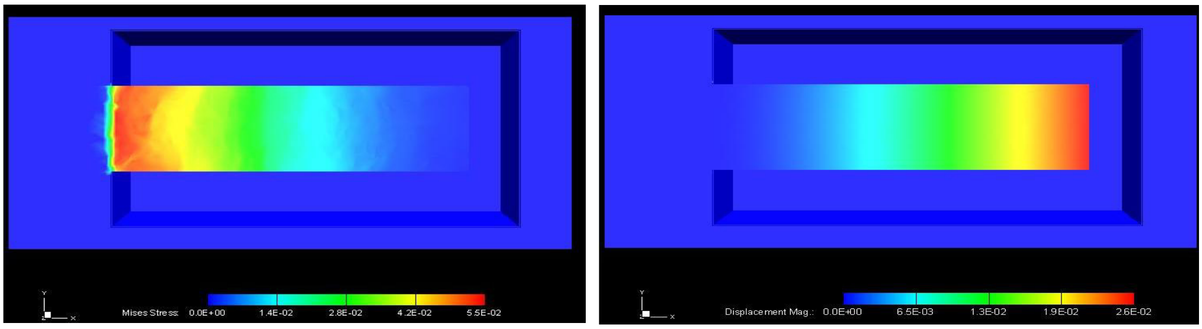

(a) **(b)**

Fig. 3.18. (a) Mises stress and (b) displacement contour of microcantilever for an applied load of 0.1Pa at 300 K.

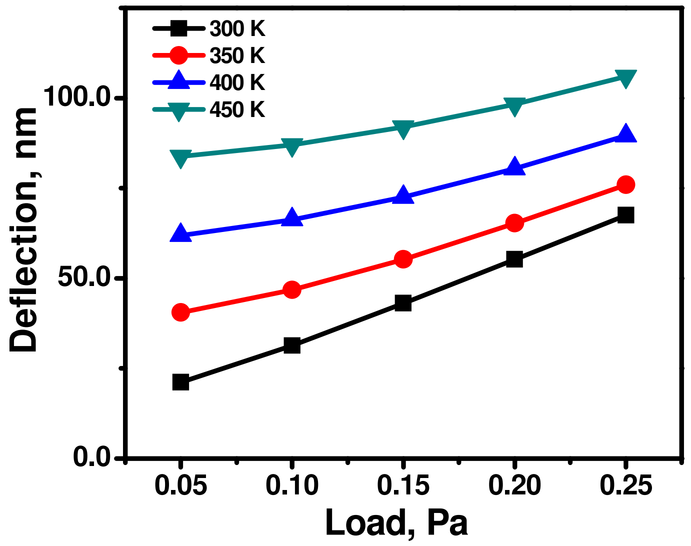

Fig. 3.19. Deflection vs applied load on the cantilever as a function of surface temperature.

3.2.2.4 Piezo resistor simulation

In a piezoresistive cantilever, the detecting resistors, called piezoresistors, are placed at the maximum stress points of the cantilever beam. As the microcantilever deflects, it undergoes a stress change that will apply strain to the piezoresistor, thereby causing a change in resistance which can be measured by electronic means. As long as the cantilever deflection is negligible compared to its length, the resistance of a piezoresistor is expected to change linearly with the deflection. Both metals and semiconductors show piezoresistance; while in metals the change of resistance is mainly a result of the geometrical variation [96], the piezoresistivity in semiconductors is a result of change in the band-gap energy [97]. Owing to the simplicity and cost effectiveness, piezoresistive detection is more widely used, especially in integrated sensor systems [62, 98]. In addition, the piezoresistive readout system can easily be integrated on the same chip using CMOS fabrication. The placement of the piezoresistor on the microcantilever surface determines the sensitivity of the chemical sensor. The highest sensitivity can be achieved by placing the piezoresistor on the cantilever surface near the base where the stress is maximum as given by:

$$\sigma_{max} = \frac{6L}{Wt^2}F = \frac{3Et}{2L^2}\,\Delta z \tag{3.1}$$

where *F* is the applied force and *w* is the width of the cantilever beam. The fractional resistivity change is proportional to the applied stress σ, and the proportionality factor is the piezoresistive coefficient, π [98]. For isotropic homogeneous material, the fractional change in resistivity, Δρ is governed by,

$$\frac{\Delta\rho}{\rho} = \pi\sigma = \pi E\varepsilon \tag{3.2}$$

where σ = Eε (Hooke's law). The change of resistance with strain is partly due to the deformed geometry of the resistor and partly due to physical changes within the material itself. Thus the strain gauge factor, G is given by,

$$G = \frac{{}^{\Delta R}/_{R}}{\varepsilon} = (1 + 2\upsilon) + \frac{{}^{\Delta\rho}/_{\rho}}{\varepsilon} \tag{3.3}$$

where Δ*R* is the resistance change resulting from the strain ε (= Δ*l*/*l*) and ν is the Poisson's ratio. The first term on the right-hand side of eq. (3.3) is the dominant factor in metals, whereas the piezoresistance of semiconductors is dominated by the second term.

In the present research work, the anchor metal comprising of Cr-Pt thin film layer is used for incorporating the piezoresistors. The resistance R of the platinum piezoresistor is given by,

$$R = \frac{l\rho}{A} = \frac{l\rho}{wt} \tag{3.4}$$

where l is the resistor length, A is the cross-sectional area, w is the width and t is thickness. The value of t is ~35 nm for the MUMPs process. In order to get maximum resistance value, w is fixed at the minimum feature size of 5 µm. The piezoresistor structure is placed close to the fixed end of the cantilever, where the Mises stress is the maximum (Fig. 3.18 (a)).

For piezoresistive analysis, the FEM solver uses the results obtained from the thermo-mechanical analysis on the cantilever deflection behaviour. The piezoresistive equations are solved using the stress field obtained from the thermo-mechanical simulations. One volt potential is applied to the piezoresistor and the resultant change in current is measured as a function of applied load and temperature. Fig. 3.20 shows the plots for the deflection and (ΔI/I) as function of applied load at various temperatures. Table 3.4 further tabulates the deflection, Mises stress and PZR sensitivity for various applied load at room temperature. As can be seen, the percentage change in current increases linearly with the stress, which in turn depends on the deflection of the cantilever. Though silicon is more sensitive and is the most widely used material for piezoresistors, its sensitivity deteriorates rapidly with increase of

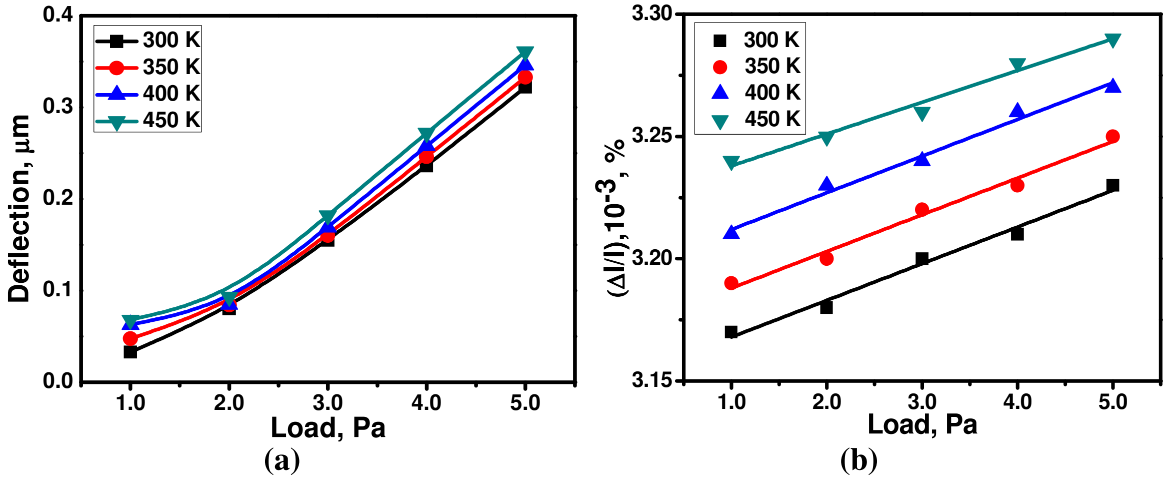

Fig. 3.20. (a) Deflection and (b) PZR sensitivity as a function of applied load and temperature.

Table 3.4. Displacement and PZR sensitivity as a function of applied load at room temperature.

Load, MPa	Deflection, μm	Stress, MPa	(ΔI/I), %
5.00E-08	1.29E-02	2.80E-02	1.47E-04
1.00E-07	2.58E-02	5.50E-02	4.29E-04
1.50E-07	3.87E-02	8.30E-02	7.08E-04
2.00E-07	5.16E-02	1.10E-01	1.15E-03
2.50E-07	6.45E-02	1.40E-01	1.45E-03

temperature. In that context, platinum is superior to silicon as the piezoresistive coefficient of platinum film is not affected much up to a temperature of 100 °C [79].

In conclusion, MUMPs process was adapted for the design of various microstructures and simulations were carried out using a commercially available FEM solver. Electro-thermal simulations of micro hotplates suggested that heaters with non-uniform resistance exhibited better temperature uniformity and low power consumption. Electro-Thermo-mechanical analysis of microcantilevers indicated that as the applied load was increased, the displacement tend to become non-linear with temperature.

CHAPTER 4: FABRICATION AND CHARACTERIZATION OF MEMS STRUCTURES

This chapter presents the mask design, fabrication and characterization studies of various micro structures. Based on the simulation results presented in the previous chapter, the design of the microstructures was optimized and subsequently fabricated. The optical, electrical and thermal characterization studies of the microstructures are discussed in detail in the following sections.

4.1 Mask design and fabrication of MEMS structures based on MUMPs process

The design of the microstructures was based on MUMPs for fabrication in a multi product wafer run (MPW). MUMPs process has six mask levels (HOLEP and HOLEM are secondary masks), the details of which are listed in Table 4.1 [38]. The process flow is shown in Fig. 4.1. The mask layouts were required to comply with the design rules like minimum feature

Table 4.1. Layer name, lithography level, minimum space and feature for MUMPs [38]

Material Layer	Thickness, µm	Lithography Level Name	Lithography Level Purpose	Min. feature, µm	Min. space, µm
Isolation Oxide	2.0		2.0 µm thermal oxide		
Oxide 1	0.5	**OXIDE1**	0.5 mm PSG; Define trench; release Nitride	20	20
Nitride 1	0.35		0.35 mm low-stress silicon nitride		
Poly	0.7	**POLY (HOLP)**	0.7 mm doped polysilicon; Pattern Poly	5	5
Nitride 2	0.35	**NITRHOLE**	Define areas where Nitride is removed. Define trench. Open hole for electrical contact between Metal and Poly	5	5
Oxide 2	1.1	**METANCH**	Open holes for anchor Metal to Nitride or Poly. Open holes for thin metal traces of Anchor Metal	50	10
Anchor Metal	0.035 (Cr + Pt)	**METANCH**			
Plating Base	0.55		500 nm Cu + 50 nm Ti		
Metal	20.5	**METAL (HOLM)**	Pattern Metal ; 20 µm Ni + 0.5 µm Au	8	8
Sidewall Metal	1.0 -3.0	**GOLDOVP**	Define area for gold Sidewall Metal and pattern Sidewall Metal	50	50

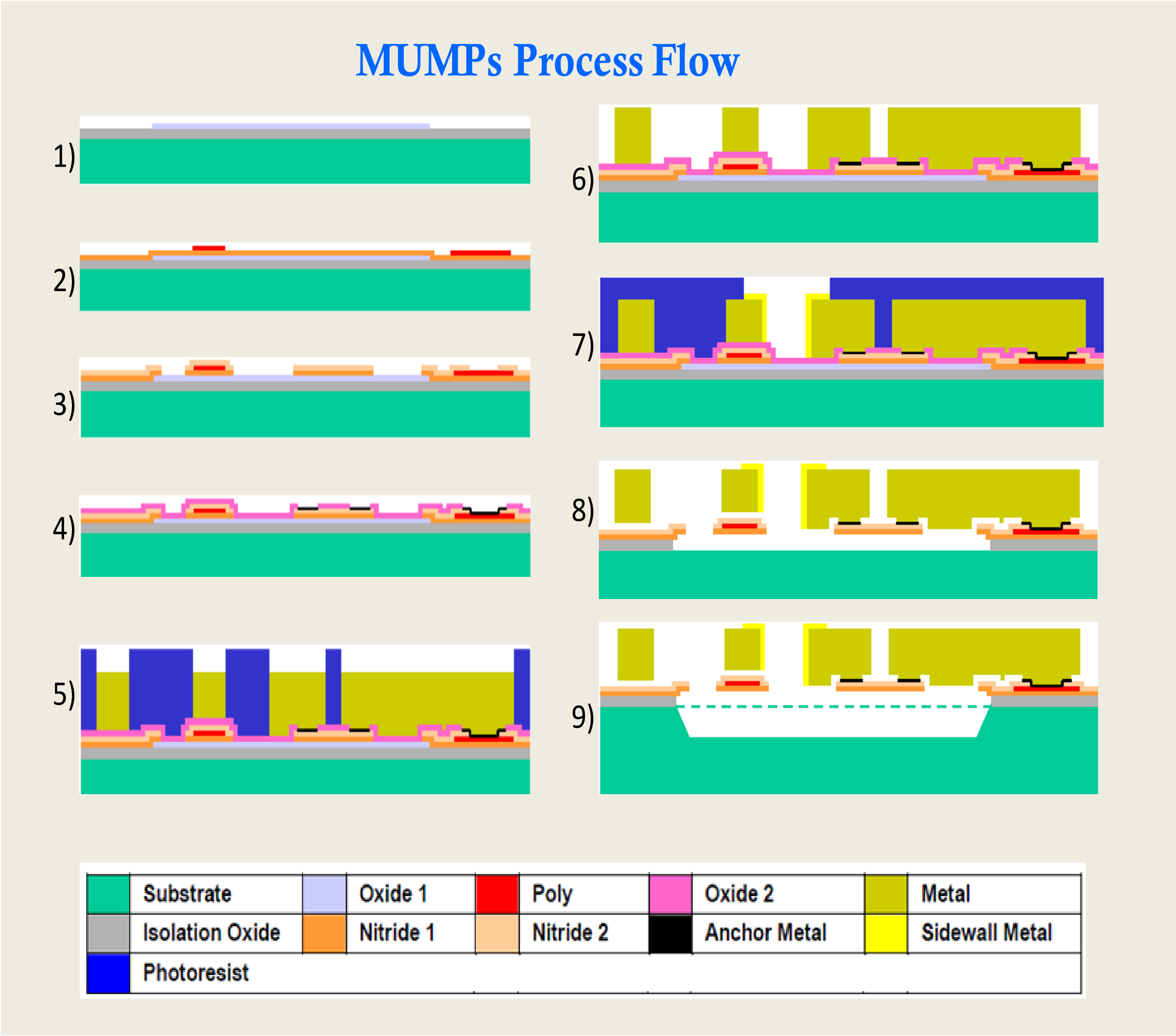

Fig. 4.1. Schematic representation of MUMPs process flow diagram [38].

size, minimum space, enclose, etc. The standard chip size for MUMPs process was 1cm x 1cm, which could be further sub-diced into 4 sub chips. So the design area was divided into four quadrants and dicing streets were drawn in POLY (width = 150 µm). The complete 2D layout showing all the masks is presented in Fig 4.2. In Fig 4.2, top two quadrants were dedicated for microhotplates of various sizes and embedded heaters. Bottom left quadrant was used for microcantilever structures. The last quadrant was used for other test structures which was not part of this research work. Each quadrant was divided into many sub modules

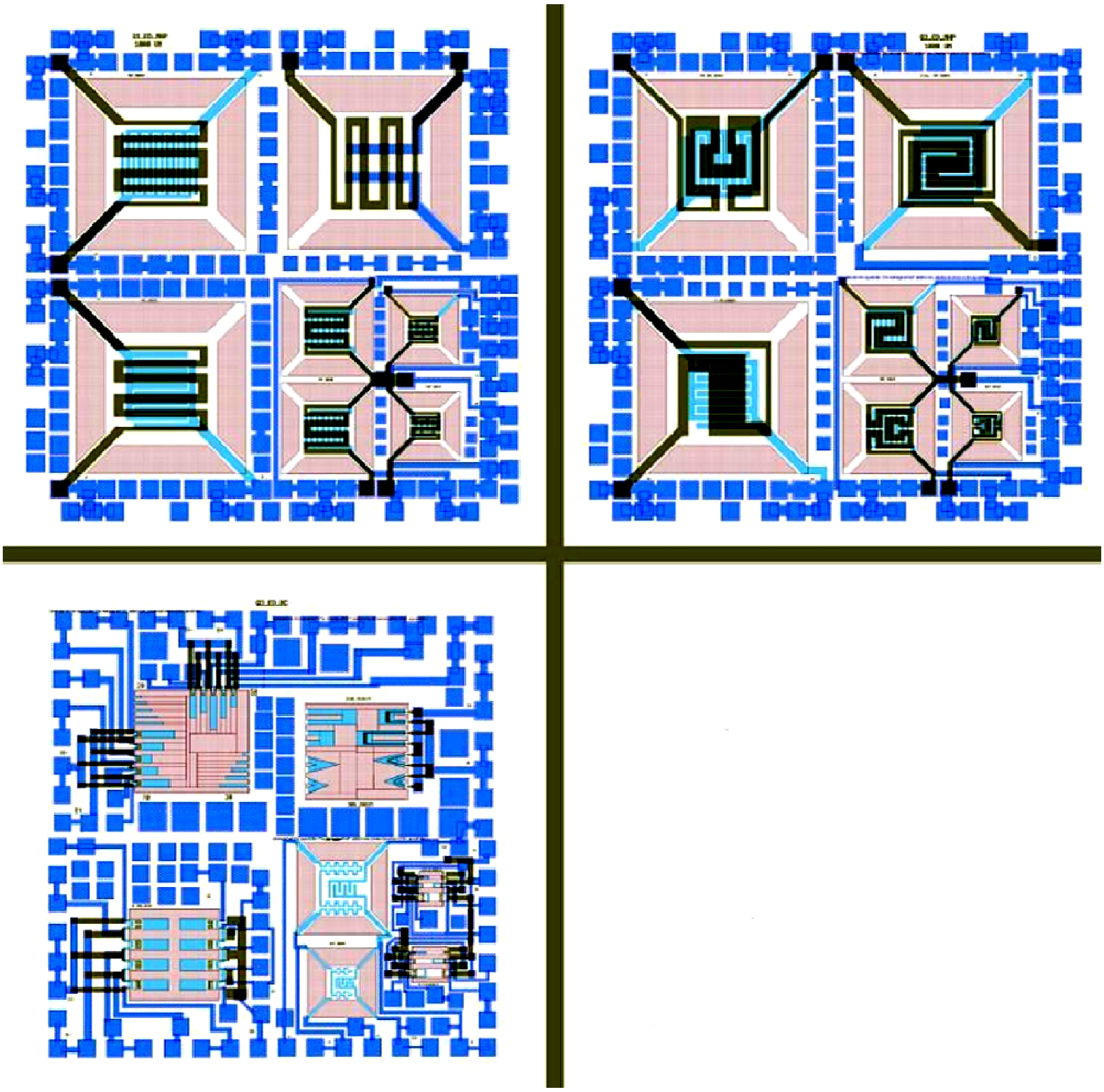

Fig. 4.2. 2-D layout of designed microstructures; top two quadrants consist of MHP of various shapes and sizes; bottom left quadrant comprises of various microcantilevers.

for ease of design and simulation. The final layout was integrated using a commercial layout editor. The complete design for six mask levels was submitted to foundry, where the microstructures were fabricated and diced.

Structural and optical characterizations were carried out on all the fabricated microstructures. As a small portion in the centre of the membranes of (900 µm × 900 µm) and (500 µm × 500 μm) MHPs were not released fully, only the smallest MHP (300 μm × 300 μm) was chosen for extensive thermal characterization.

4.2 Structural and optical characterization of microstructures

A variety of techniques are available for the characterization of MEMS structures to measure various physical properties such as film thickness, step height, dimension, roughness, cross section, stress, stiction, response time, thermal expansion, resonance frequency, etc. Table 4.2 shows a comparison of commonly available optical techniques for MEMS devices. For this research work, optical microscopy and SEM were used to study the individual structures and verify the design geometries. Laser Doppler Vibrometry (LDV) was used for dynamic measurements such as vibrational velocity and displacement and White Light Interferometer (WLI) was employed for surface topography measurements.

Table 4.2. Comparison of MEMS optical measurement tools [99].

Technique	Lateral Resolution (typical)	Vertical Resolution (typical)	Static Shape	Dynamic Response
AFM (Atomic Force Microscopy)	0.0001 μm	0.0001 μm	3D	No
SEM (Scanning Electron Microscope)	0.001 μm	-	2D	No*
OM (Optical Microscopy)	<1 μm	<1 μm	2D	No*
WLI (White Light Interferometer)	<1 μm	<0.001 μm	3D	No**
CM (Confocal Microscopy)	<1 μm	<0.01 μm	3D	No
DHM (Digital Holographic Microscopy)	<1 μm	<0.001 μm	3D	Yes
SVM (Strobe Video Microscopy)	<0.01 μm	<1 μm	2D	Yes
LDV (Laser Doppler Vibrometry)	<1 μm	$<10^{-6}$ μm ***	No	Yes

**Dynamic response possible using video capture technique; **Dynamic response possible using strobe technique; ***Resolution for dynamic response – not static*

4.2.1 Optical microscopy and SEM characterization

An optical microscope or a compound light microscope uses visible light and a system of lenses to magnify the image of an object that is projected onto the retina of the eye or onto an imaging device. A modern optical microscope can have a maximum magnification of about 1000X. Optical microscopy is the most useful and simplest method for general inspection purpose of samples. Major disadvantage of this technique is that the resolving power of the microscope is limited by the number and quality of the lenses and by the wavelength of the light used for illumination.

A scanning electron microscope (SEM) employs a focused electron beam to scan over a surface and create an image. The beam of electrons interacts with the sample and produces various signals that can be used to obtain information about the surface topography and composition. The most common SEM mode is the detection of secondary electrons emitted from the surface of the sample. This secondary electron imaging can generate very high-resolution images (better than 1nm), discerning the microscopic details of a sample surface. In addition, SEM images can have a large depth of field that gives a characteristic three-dimensional appearance of the sample surface. In most cases, SEM is used in conjunction with Energy Dispersive X-ray (EDX) to determine chemical composition of the samples.

Figs. 4.3 – 4.5 show the optical and SEM micrographs of some of the fabricated microhotplates and microcantilevers. Various layers of the structures such as the Si_3N_4 structural layer, embedded poly heater, Cr-Pt electrodes and Ni-Au layer on bond pads and microcantilever surface - are seen from the micrographs. From SEM images, it is clearly seen that structures are suspended above the trench.

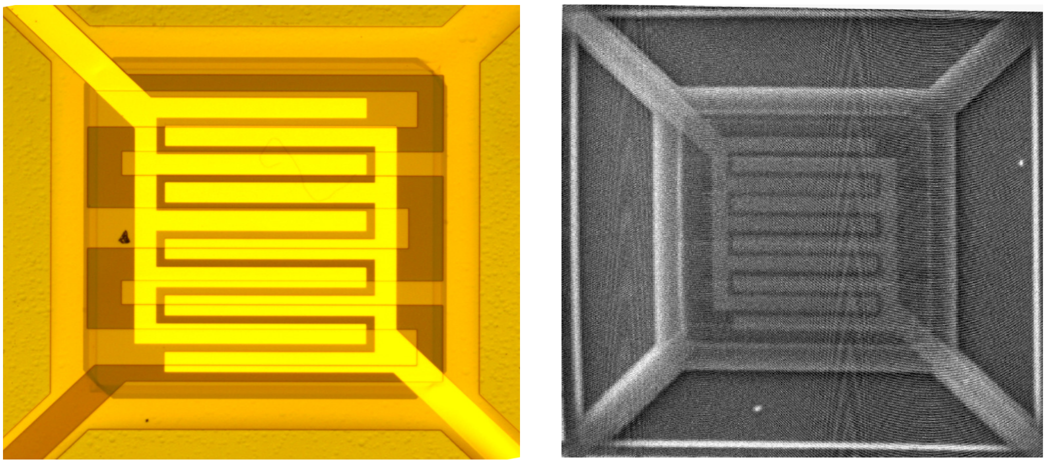

Fig. 4.3. Optical and SEM micrographs of Micro hotplates with Cr-Pt electrodes (Membrane size is 900 μm × 900 μm).

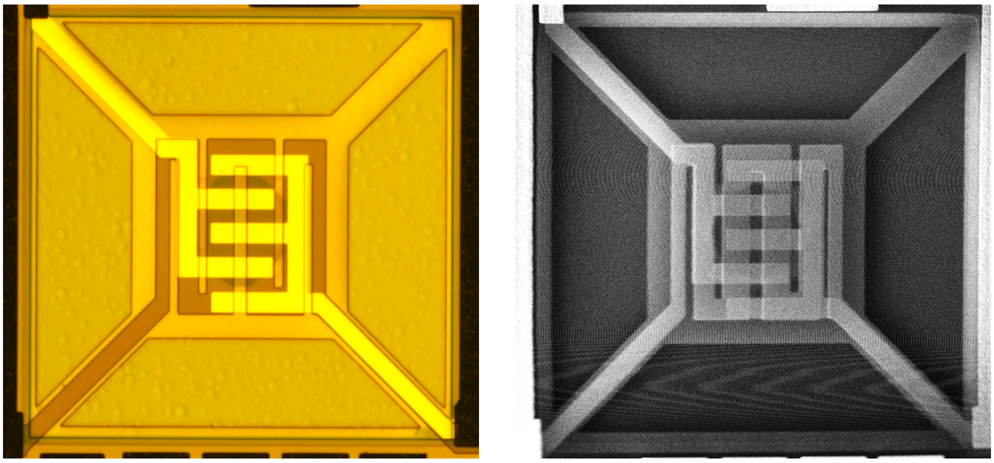

Fig. 4.4. Optical and SEM micrographs of 300 μm × 300 μm Micro hotplates.

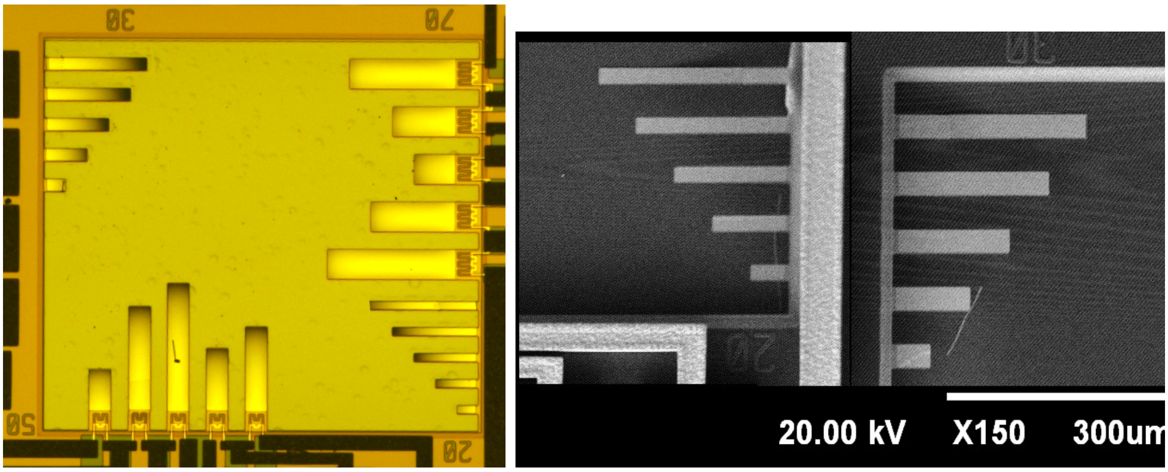

Fig. 4.5. Optical and SEM micrographs of rectangular microcantilevers.

4.2.2 Surface topography by white light interference

Static surface topography measurements using WLI provide X-Y-Z mapping of the device surface to evaluate parameters such as step heights, flatness, roughness, curvature, parallelism, angles and volumes [99]. The results can be presented as 2-D or 3-D mappings for defect analysis and / or processing to extract parameter values for given areas.

WLI is based on Michelson interferometer using the optical configuration shown in Fig. 4.6. The white light source has a coherence length in the µm range. The collimated light beam is split by a beam splitter into an object beam and a reference beam. The light scattered back from the mirror and the specimen respectively are superimposed at the beam splitter again and directed to the CCD camera. The resulting fringe patterns are mapped out for each pixel in the camera image. By moving the position interference lens using a Z stage, the interference signal is modulated for each pixel resulting in a correlogram. The maximum value of the

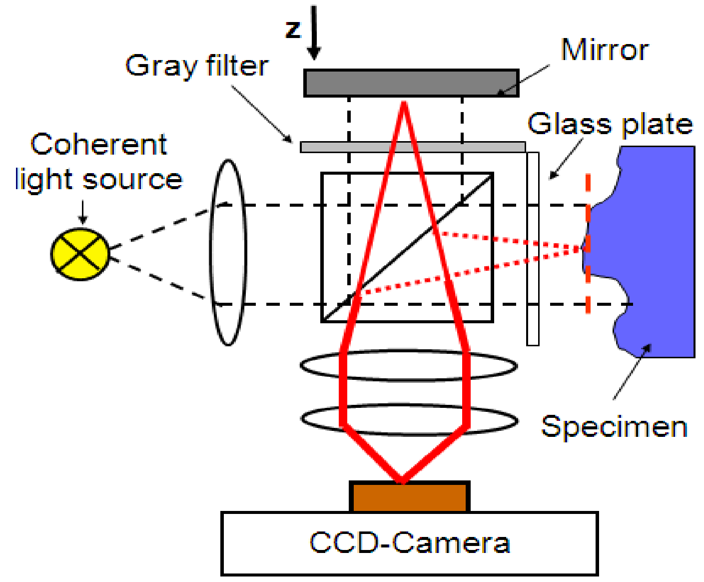

Fig. 4.6. Schematic of white light interferometer [99].

correlogram occurs when the path distance to the reference mirror and the distance to the device surface are the same. These correlograms are further processed to get true 3-D topographical representation of the surface.

Figs. 4.7 and 4.8 show the 2-D and 3-D topography of various microstructures fabricated by MUMPs process. The height difference of various layers between the trench of the substrate and the top most metal layer is clearly visible from the images. It is observed that the geometries matched very well with the designed X-Y-Z dimensions for all the microstructures.

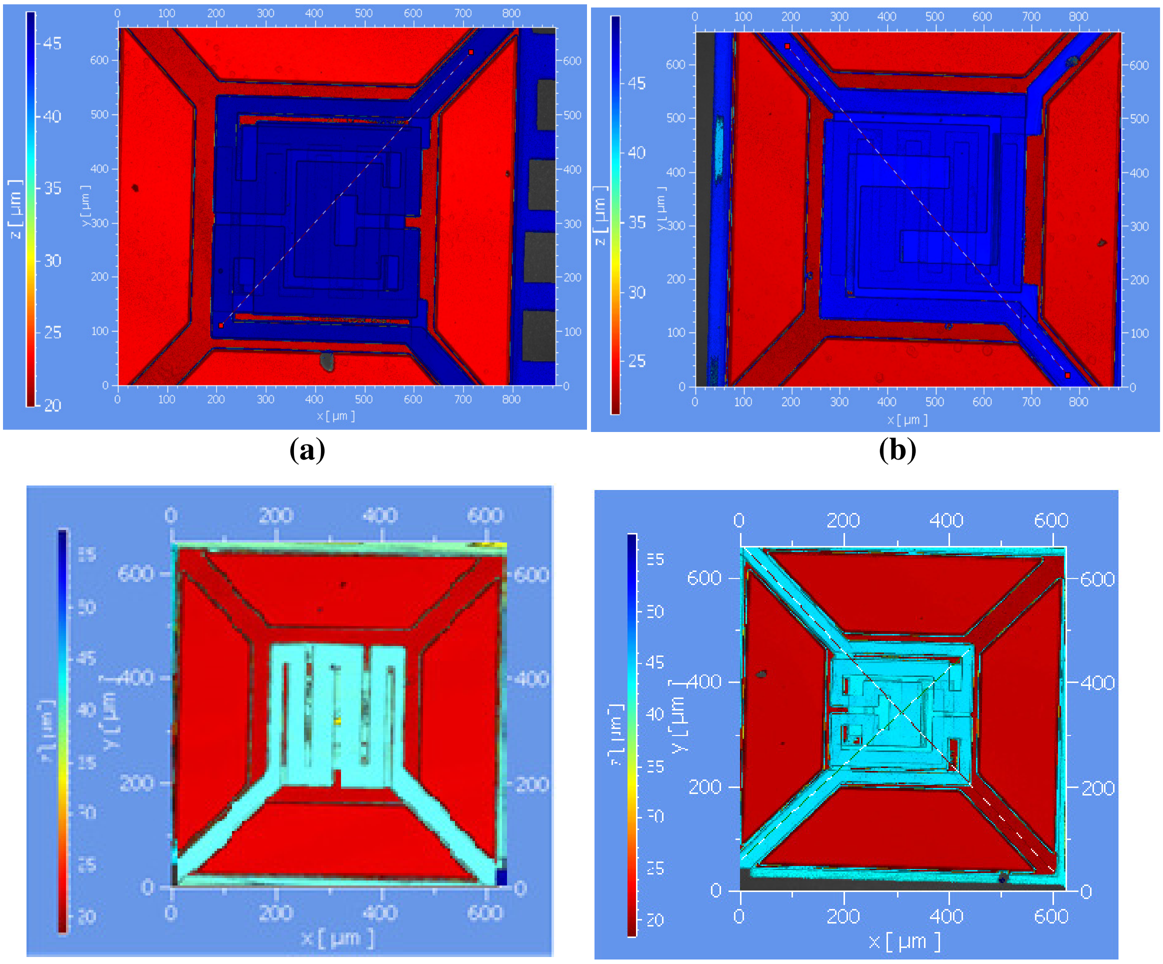

(a) (b)

(c) (d)

Fig. 4.7. 2-D topography images of (a) fan and (b) spiral shape heater (500 µm × 500 µm); (c) serpentine and (d) fan shape heaters (300 µm × 300 µm).

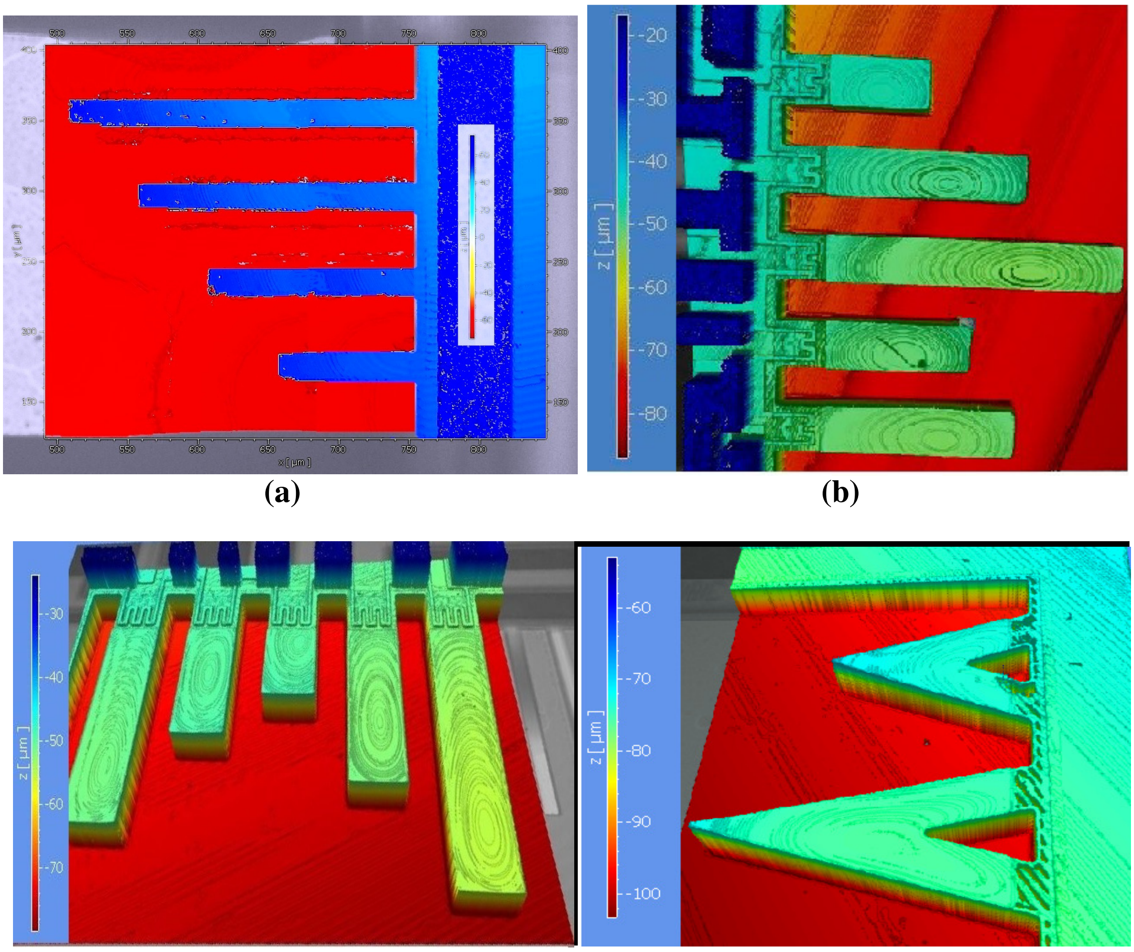

(a) **(b)**

(c) **(d)**

Fig. 4.8. 2 -D topography images of (a) 20 µm and (b) 50 µm width microcantilevers; 3-D topography of (c) 70 µm and (d) V- shape microcantilevers.

4.2.3 Laser Doppler vibrometry of microcantilevers

The laser Doppler vibrometry is a non contact mode technique using laser technology to measure the velocity and displacement at selected points on a vibrating structure [99]. The laser beam can be focused to about 1 µm size spot on the MEMS structures, which is being investigated under an optical microscope. Diffraction limitations prevent measurements of devices smaller than the wavelength of light used (633 nm). LDV is a high sensitive optical technique with the capability of measuring displacements from centimeters to picometers at frequencies from near DC to few GHz. In addition to their broad frequency range, LDVs also have a high dynamic range (over 170 dB) for velocity amplitudes from 0.02 µm/s to 10 m/s [100]. The basic arrangement of LDV is depicted in Fig. 4.9. As the name suggests, LDV uses Doppler effect, where the back scattered light from a moving target carries information about the motion quantities - velocity and displacement - at the point of incidence. Displacement of the surface modulates the phase of the light wave while instantaneous velocity shifts the optical frequency. Using interferometric techniques, the reflected light wave is mixed with a reference beam and the beams recombine at the photo detector. Using phase and frequency demodulators, the instantaneous Doppler frequency is converted into voltage proportional to vibration velocity.

In order to measure the resonant frequency and vibrational velocity of the fabricated microcantilevers, LDV was used in the frequency range 0 – 1 MHz. The MEMS chip containing the microcantilevers was mounted on a piezoelectric actuator, which was powered by a sinusoidal signal of up to 5 V. Fig. 4.10 shows the first 3 modes of 30 µm × 200 µm rectangular microcantilevers. As can be seen, the vibrational mode shapes comply with those

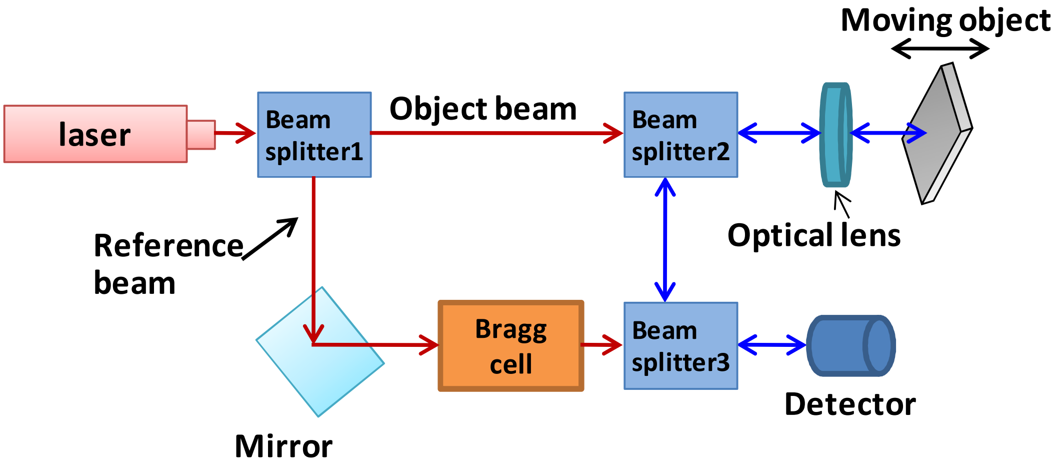

Fig. 4.9. Basic components of a Laser Doppler Vibrometer.

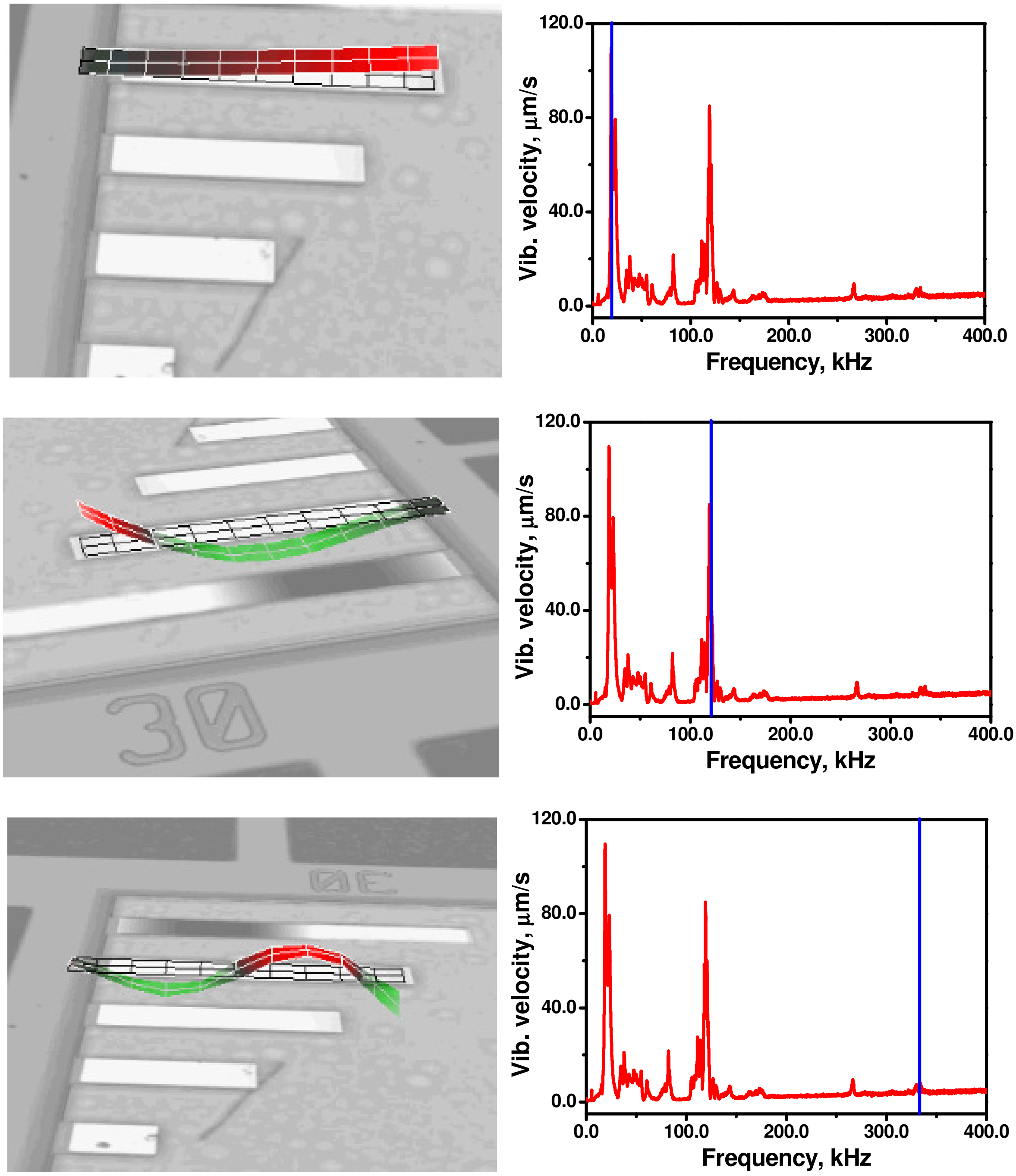

Fig. 4.10. First 3 modes of 30 µm × 200 µm rectangular microcantilever; corresponding modal frequency is marked in the velocity plot.

shown in Fig. 2.9. The amplitude of vibration is significant only for the first two modes. In general, microcantilever based sensors are operated in first mode. Nevertheless higher vibrational modes can also be used to obtain better sensitivity [70].

Fig. 4.11 shows the comparison of experimental and simulated results of the first modal frequency of 20, 30, 50 and 70 μm width rectangular microcantilevers as a function of cantilever length. In compliance with eq. (2.21), the modal frequency decreased as the microcantilever length increased. It is seen that the simulated results are marginally higher than the actual modal frequency and the error is within 20% for <100 kHz. Though the simulation model takes into account of MUMPs process details, complex effects such as geometric errors, non-uniformities, damping, residual stress, mismatching mask alignment, etc. during the fabrication are not accounted for in an idealized model.

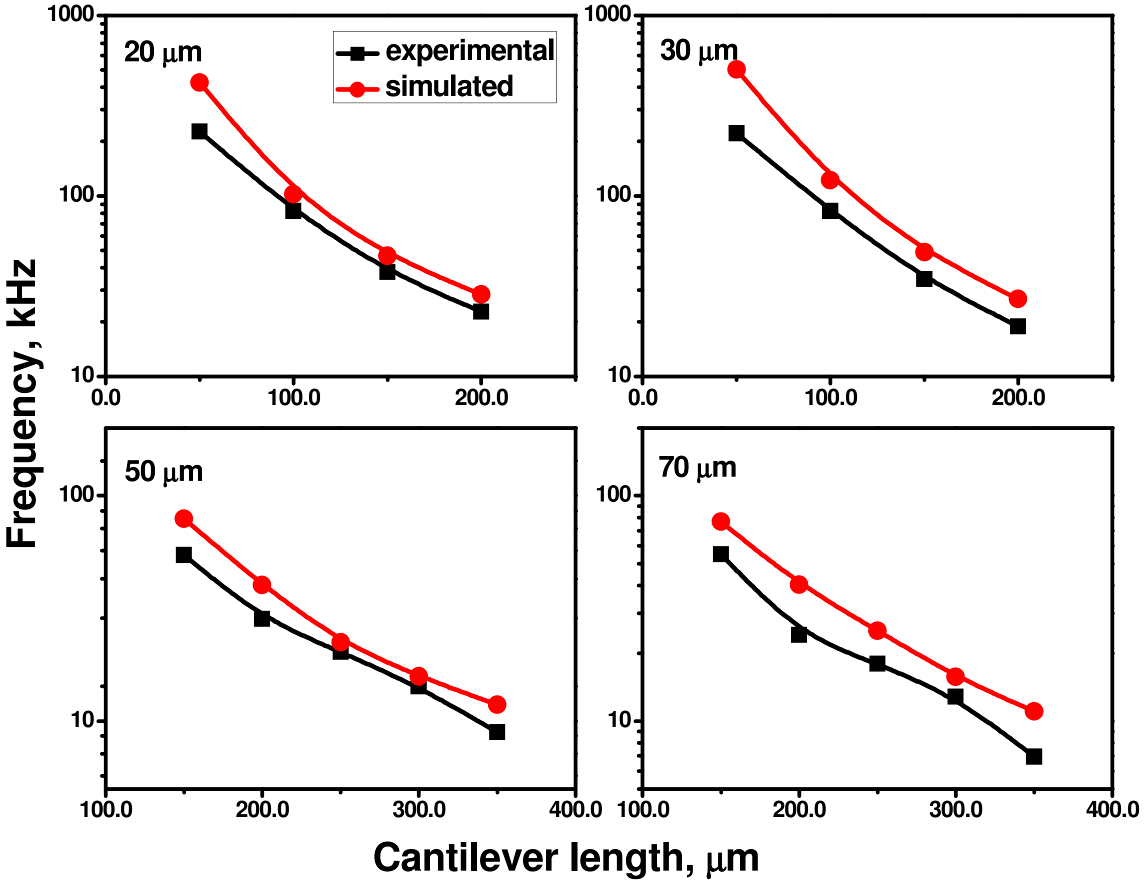

Fig. 4.11. Comparison of simulated and experimental first modal frequencies as a function of cantilever length for rectangular microcantilevers.

4.3 Electrical characterization and thermal imaging of microhotplates

In order to carry out the electrical characterization and thermal imaging, some of the (300 µm × 300 µm) MHP chips were fixed on a PCB and the contact pads are wirebonded to the PCB using 25 µm aluminum wire to facilitate electrical connections (Fig. 4.12). For estimating the thermal efficiency, the MHP was heated by applying voltage to the heater pads. For calculating the Temperature Coefficient of Resistance (TCR), the MHP chips were mounted on a heating stage, whose temperature was precisely controlled by a PID temperature controller.

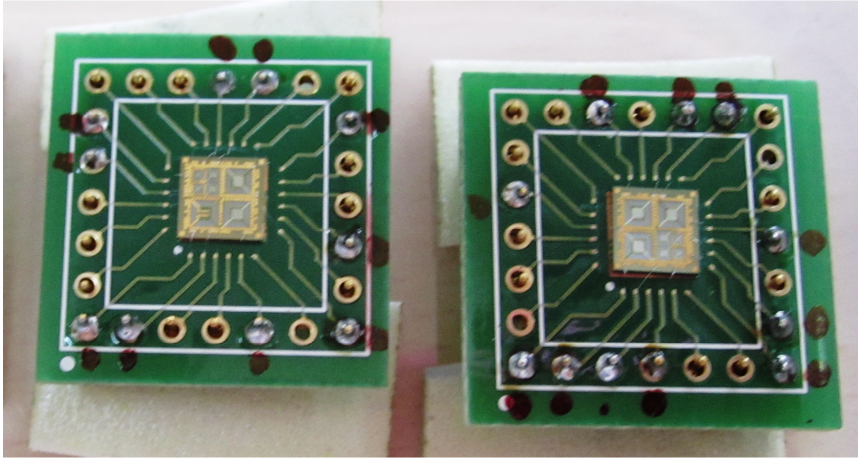

Fig. 4.12. Wirebonded microhotplates packaged on PCB.

4.3.1 Electro - Thermal characterization of MHPs

The heat on the MHP is generated by resistive Joule heating. The thermal energy, Q, generated by the Joule effect is given by (eq. 2.1):

$$\Delta Q = R\, I^2\, \Delta t \qquad (4.1)$$

where I is the current flowing through the heater resistance R during Δt time. Within a limited range of temperature, the resistivity increases linearly with temperature. The change in resistance of the poly silicon heater with temperature can be represented by [101],

$$R_T = R_o(1 + \alpha T) \tag{4.2}$$

where, R_T is the resistance at temperature T, R_o is the base resistance at reference temperature (usually room temperature) and α is the material property termed as the TCR. TCR can be obtained by rearranging eq. (4.2):

$$\alpha = \frac{(R_T - R_0)}{R_0 T} = \frac{\left(\Delta R/_{\Delta T}\right)}{R_0} \tag{4.3}$$

TCR can be experimentally determined from the slope of the resistance of polysilicon heater vs temperature data. Accordingly, the heating stage temperature was increased in steps. The actual temperature of the MHP chips was measured by an RTD temperature sensor and the corresponding resistance value of the polysilicon heater was measured by a digital multimeter. Fig. 4.13 (a) shows the resistance vs temperature plot of 300 μm × 300 μm serpentine and fan MHP. From the slope of the curves, the TCR value of polysilicon was

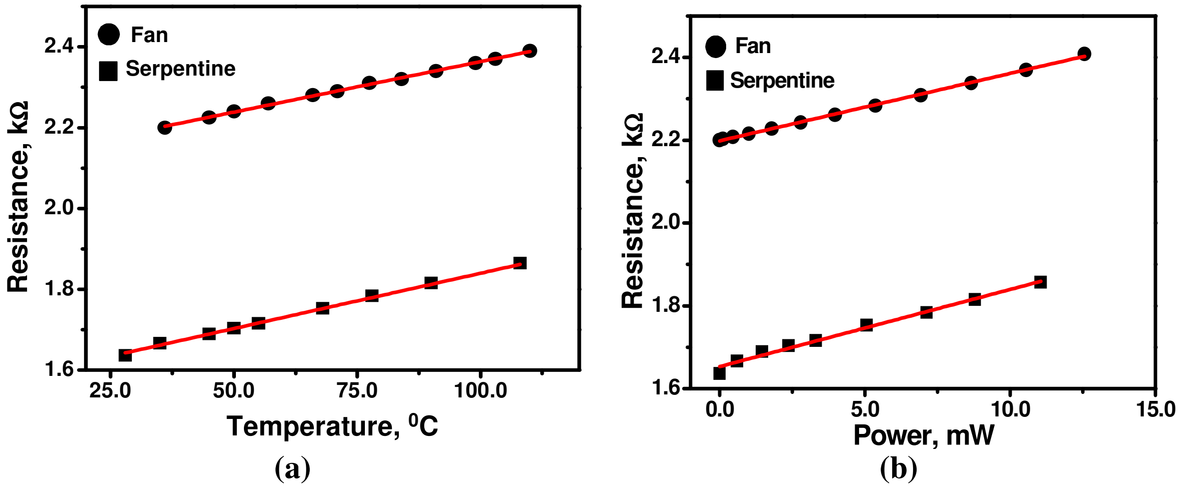

Fig. 4.13. (a) Heater resistance as a function of temperature when the MHPs were mounted on a heating stage. (b) Heater resistance as a function of applied power.

estimated as 2.6×10^{-3} / °C. The heater resistance increased linearly in the measured temperature range for both the MHPs. Thermal efficiency of the microhotplates was computed by electrically heating the polysilicon resistor with known heater power and measuring the resistance values. The heater resistance as a function of input heating power is shown in Fig. 4.13 (b). The resistance changed linearly with applied power at the rate of ~ 18 Ω / mW and ~ 16 Ω / mW respectively for serpentine and fan shape heaters. The resistance data were then correlated to the corresponding temperatures using the TCR value to compute the thermal efficiency. From Fig. 4.13 (a) and (b), thermal efficiency of both the MHPs was determined as ~10 ºC / mW, which is higher as compared to other similar commercial sensor substrates [102].

4.3.2 Temperature profile measurement of MHPs

Preliminary measurements of temperature profile of the MHPs were carried out by optical microscope by applying sufficient heater power such that the MHP glowed red-hot. Fig. 4.14 shows the optical micrographs of serpentine and fan shape MHPs at an applied power of 90

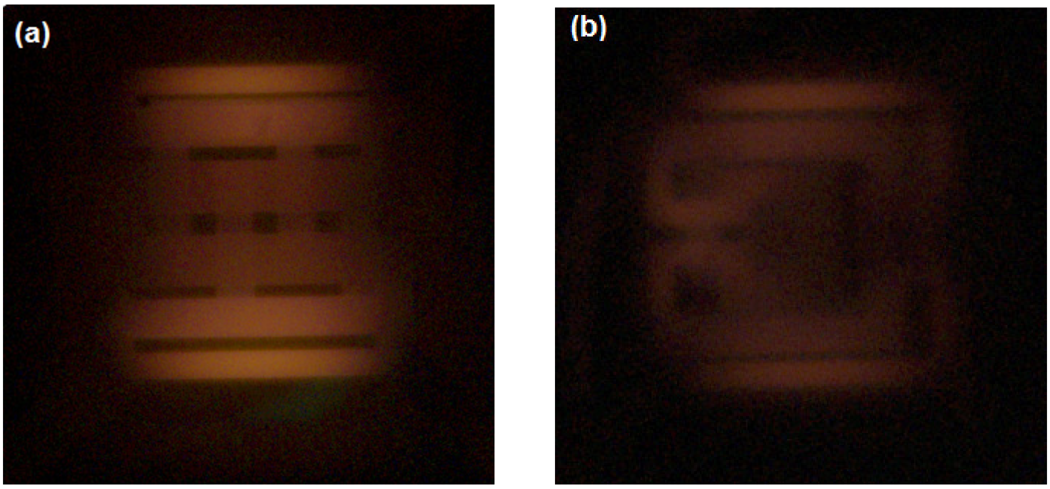

(a) **(b)**

Fig. 4.14. Optical micrograph of (a) serpentine and (b) fan shaped MHPs; Heater power was 90 mW for the serpentine and 83 mW for the fan shape MHP.

mW and 83 mW respectively. As discussed above, by controlling the current density, the temperature of the outer part of the MHP was maintained higher in order to compensate for the heat loss due to conduction through the supporting beams.

The heating characteristics of the MHPs were further evaluated with a thermal imaging camera. The camera used a high sensitivity InSb focal plane array detector in the spectral range between 3.6 µm to 5 µm. Figs. 4.15 and 4.16 show the thermal images of serpentine and fan shape MHPs for various applied heater voltages. It is seen from the figures that more than 90% area of the suspended membrane is heated uniformly. Other than the suspended MHP, the remaining substrate stayed nearly at room temperature, resulting in localised heating. This is the major requirement of MHP based gas sensors.

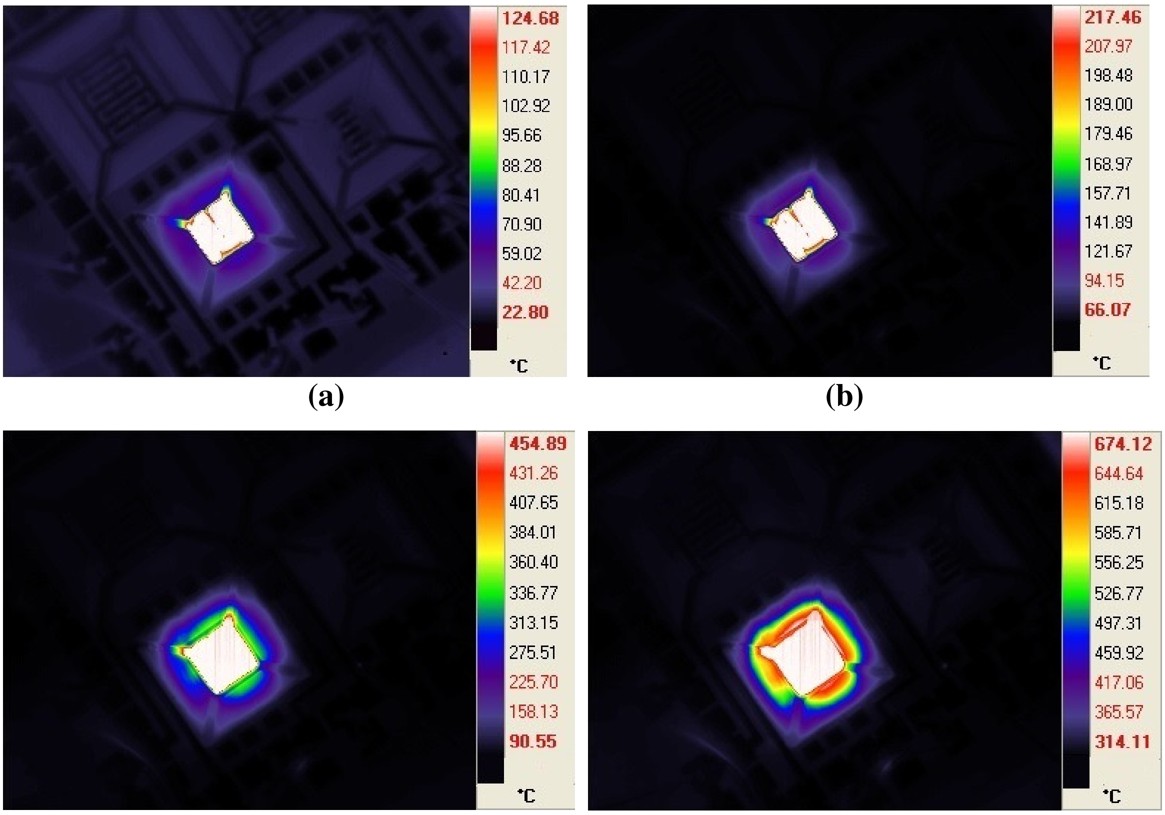

(a) (b)

(c) (d)

Fig. 4.15. Thermal image of serpentine MHP for an applied heater voltage of (a) 5 V, (b) 8 V, (c) 10 V and (d) 12 V.

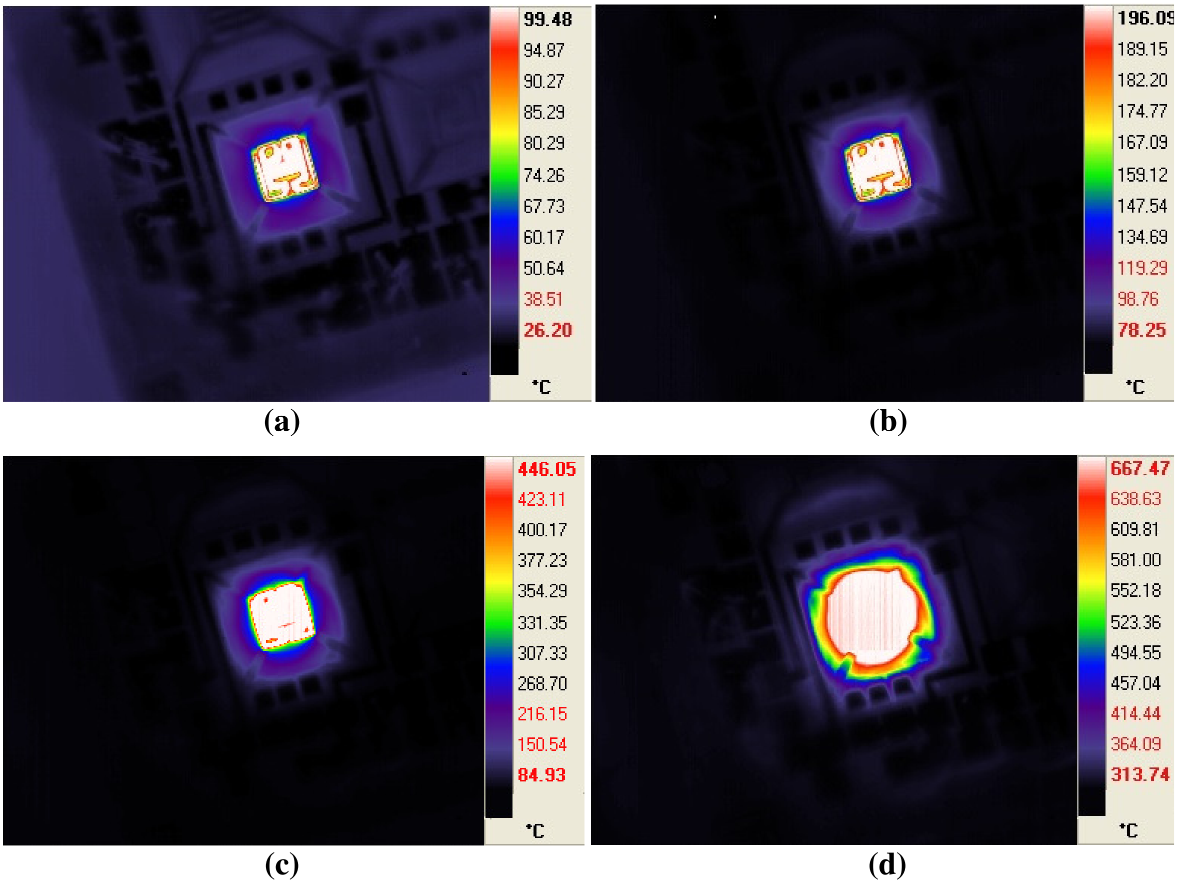

Fig. 4.16. Thermal image of fan MHP for an applied heater voltage of (a) 5 V, (b) 8 V, (c) 10 V and (d) 12 V.

The average temperature of the active area comprising IDE as a function of applied heater power is shown Fig. 4.17 for both the MHPs. An average temperature of 650 °C could be achieved for an applied power of < 55 mW for both the MHPs. Though the MHPs were designed for continuous heating, the possibility of using temperature modulation was explored by applying heater voltage in ON-OFF mode. Fig. 4.18 shows the thermal response of serpentine (at 10 V and 15 V) and fan (15 V) MHPs for an applied heater voltage. Thermal response time is defined as the time taken by the MHP to reach the steady state temperature thermal response (limited by the switching time of power supply) owing to the small dimensions and excellent thermal isolation of the suspended membrane.

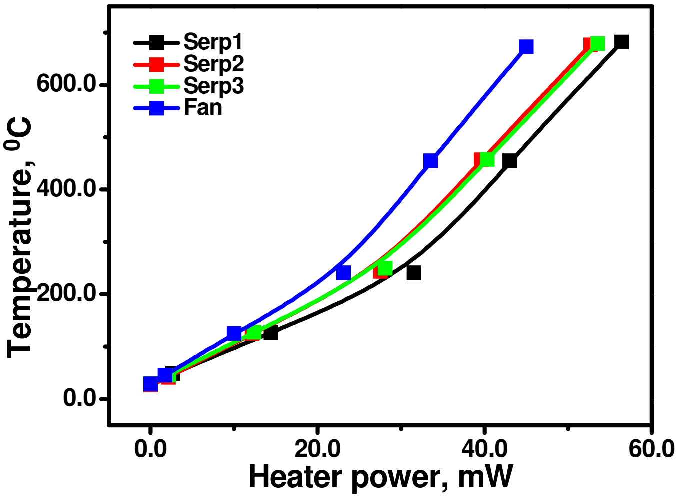

Fig. 4.17. Average temperature as a function of applied heater power for serpentine and fan MHPs.

Fig. 4.19 shows the comparison of temperature characteristics as evaluated by FEM simulation, electro-thermal measurements and thermal camera for serpentine MHP. Similar results were obtained for fan shape MHP also. Though the simulation model took into account of MUMPs process details, complex effects such as geometric errors, damping, non-uniformities, residual stress, mismatching mask alignment, etc., during the fabrication were

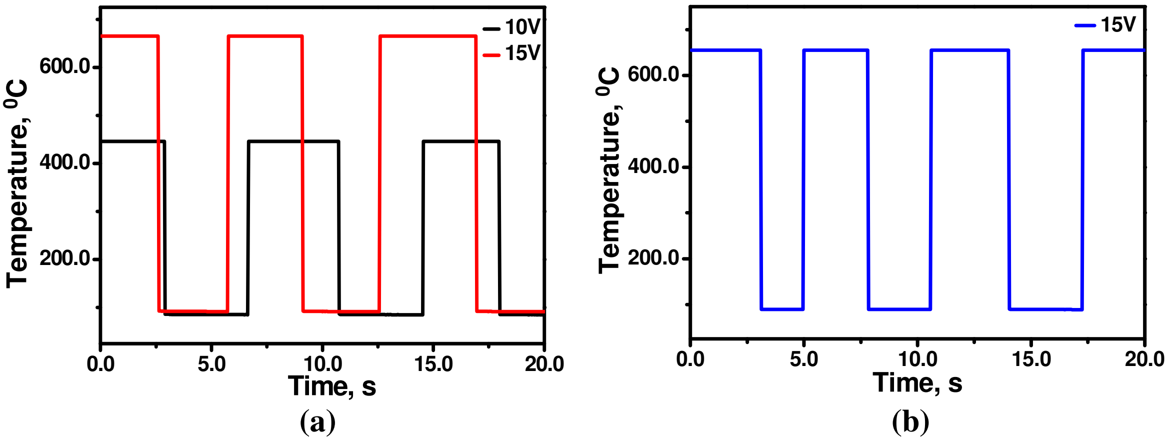

(a)

(b)

Fig. 4.18. On-Off switching characteristics of (a) serpentine and (b) fan MHPs at fixed heater voltage.

not accounted for in an idealized model. Hence there is a deviation of the simulated temperature curve at higher heater power compared to the experimental data. It is evident from Fig. 4.19 that there is a good agreement between the temperature characteristics as measured by thermal camera and as estimated from the electrical measurements.

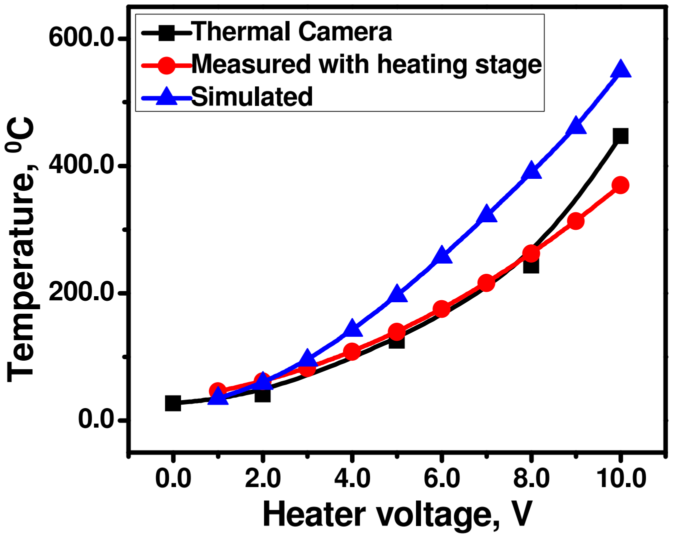

Fig. 4.19. Comparison of temperature characteristics evaluated by FEM simulation, electro-thermal measurements and thermal camera for serpentine heater MHP.

4.3.3 Gas sensing performance studies

Preliminary studies on gas sensing performance were carried out by depositing SnO_2 thin film by RF magnetron sputtering technique on the IDE of serpentine MHP chip (without any mask). Commercially available sintered SnO_2 target was used for sputtering at an RF power of 75 W and Ar : O_2 ratio of 1:1. Typical response curve of the MHP gas sensor for 2.5 ppm H_2S is shown in Fig. 4.20. When the sensor was exposed to H_2S, the gas molecules interacted with the adsorbed oxygen species on the SnO_2 surface and injected the electrons

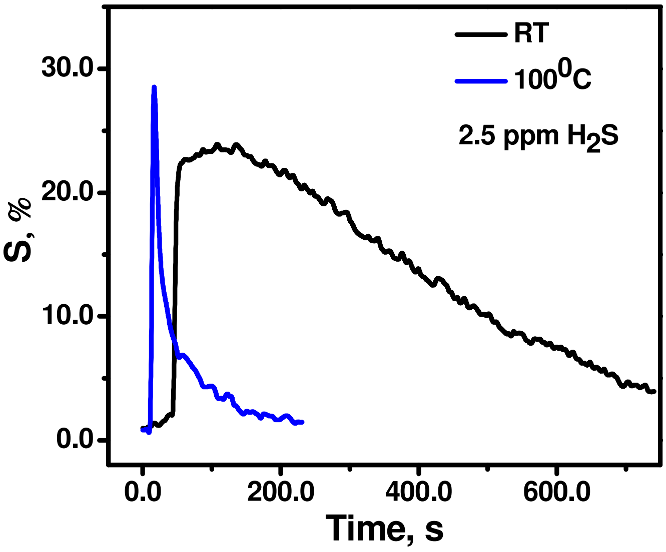

Fig. 4.20. H_2S sensing characteristics of RF sputtered SnO_2 thin film deposited on 300 µm × 300 µm MHP.

back to the conduction band, thereby increasing the surface conductivity. As expected, the response kinetics was better at 100 °C compared to that at room temperature [16].

In conclusion, various microcantilevers and microhotplates were fabricated by MUMPs. Optical microscopy, SEM and WLI measurements confirmed that the geometries matched very well with the designed X-Y-Z dimensions for all the microstructures. Optical microscopy and IR thermal imaging of the MHPs confirmed the temperature homogeneity on the suspended membrane. Thermal efficiency of the MHPs was estimated at ~10 °C / mW by electro-thermal characterization and by IR thermal imaging.

CHAPTER 5: DEPOSITION AND CHARACTERIZATION OF METAL OXIDE FILMS

Synthesis of the sensing layer is undoubtedly the most crucial part in the preparation of gas sensors. The sensing layer is mostly in the form of thin film, which is a low-dimensional material, constructed by condensing atomic / molecular / ionic species of matter, one-by-one [103]. Thin film deposition techniques are broadly classified into two types - physical and chemical - depending on how the atoms / molecules / ions / clusters of the sensing material are generated for the condensation process. In Chemical Vapor Deposition (CVD), a precursor gas reacts at the hot substrate surface to produce the atoms / molecules of interest. Physical Vapor Deposition (PVD) method includes the deposition techniques which depend on the ejection / sputtering or evaporation of the material from a source. PVD is preferred than CVD for MEMS based sensors since it can be performed at a lower process risk in terms of process environment, deposition temperature, etc., and is cheaper in regards to material costs. In this research work, sputter deposition is adopted for the deposition of sensing layers and thermal evaporation is adopted for the electrode deposition.

5.1 Deposition of metal oxide thin films

Sputtering is one of the most versatile techniques used for electronic / sensor grade thin film deposition. Sputtering process produces homogeneous films with better controlled composition, greater adhesion and excellent control of film thickness. In sputtering process an inert gas plasma, usually of argon is created by applying a high voltage between the target holder (cathode) and the substrate holder (anode). Sputtering starts when the positively charged gas ions in the plasma region are attracted to the negatively charged target at very high velocity, Due to the momentum of collisions, atomic size particles are ejected from the target. These particles are condensed as a thin film onto the surface of the substrates. Sputtering is normally performed in the pressure range of 10^{-3} to 10^{-2} mbar [103].

5.1.1 DC and RF magnetron sputtering techniques

Depending on the power supply used for plasma generation, sputtering process is classified as DC and RF sputtering [103]. A schematic representation for both the systems is shown in Fig. 5.1. In DC sputtering system, a direct voltage is applied between the cathode and anode and the plasma is generated. The positive ions strike the target to remove the neutral target atoms and condense in to thin films on the substrate. DC sputtering is mostly used for all conductive target materials. However, DC sputtering cannot be used to sputter insulating materials as the sputtering glow discharge cannot be sustained due to the build-up of positive charge on the surface of the insulating target. Radio Frequency (RF) sputtering is suitable for both conducting and non-conducting materials. The frequency of 13.56 MHz is

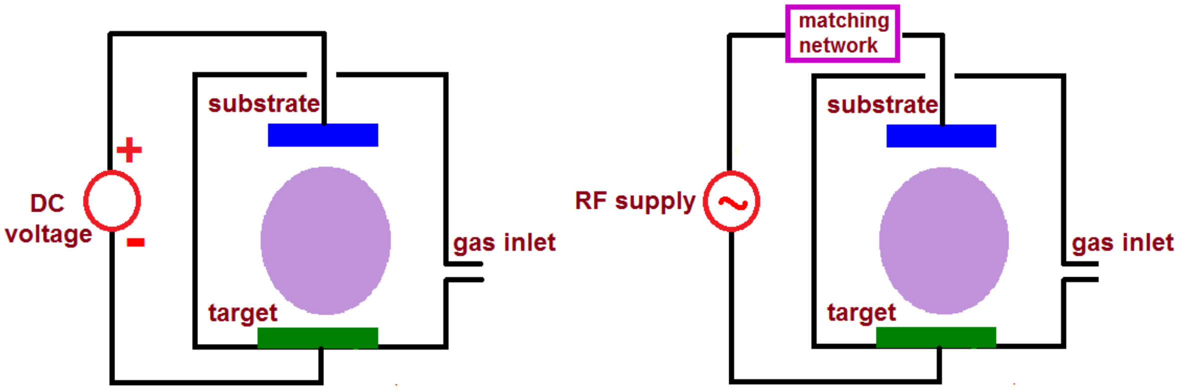

Fig. 5.1. Schematic of DC and RF sputtering methods.

often used for commercial RF sputtering systems. In these systems, the target is coupled to the RF generator through a series capacitor and a suitable matching network. This large series capacitor causes a significant negative bias to develop on the cathode (self-bias). Because the target is capacitively coupled to the plasma that prevents charge build-up on the target surface, RF sputtering is suitable for both conductive and insulating material.

In conventional DC and RF sputtering systems, the energetic electrons in the plasma do not significantly contribute to the sustenance of plasma. Most of these electrons are attracted to the substrate, resulting in unwanted heating. Thus, both DC and RF sputtering suffer from poor ionization efficiencies in the plasma, low deposition rates, and high thermal load of the substrate due to bombardment of secondary electrons. These limitations can be overcome to a great extent by the use of magnetron sputtering. Magnetron sputtering uses strong magnets to confine the electrons at or near the target surface, making it easier to sustain the glow discharge at low pressure. The magnets are placed in such a way that one pole is positioned at the center of the target and the second pole consists of a ring of magnets around the outer edge of the target as shown in Fig. 5.2. The strong magnetic field near the target area causes the electrons to travel in spiral path along magnetic flux lines near the target. The confinement of electrons near the target substantially increases the probability of an ionising electron-atom collision. The increased ionisation efficiency results in dense plasma near the target region. This, in turn, leads to increased ion bombardment of the target, giving higher sputter yield and higher deposition rates on the substrate. As the plasma is confined near the target area, the electrons do not damage the thin films being formed on the substrate, thereby maintaining the thickness uniformity and stoichiometry of the deposited thin film. In addition, the increased ionisation efficiency attained by the use of magnetron facilitates the discharge to be maintained at lower operating pressures (typically, 10^{-3} mbar) and lower

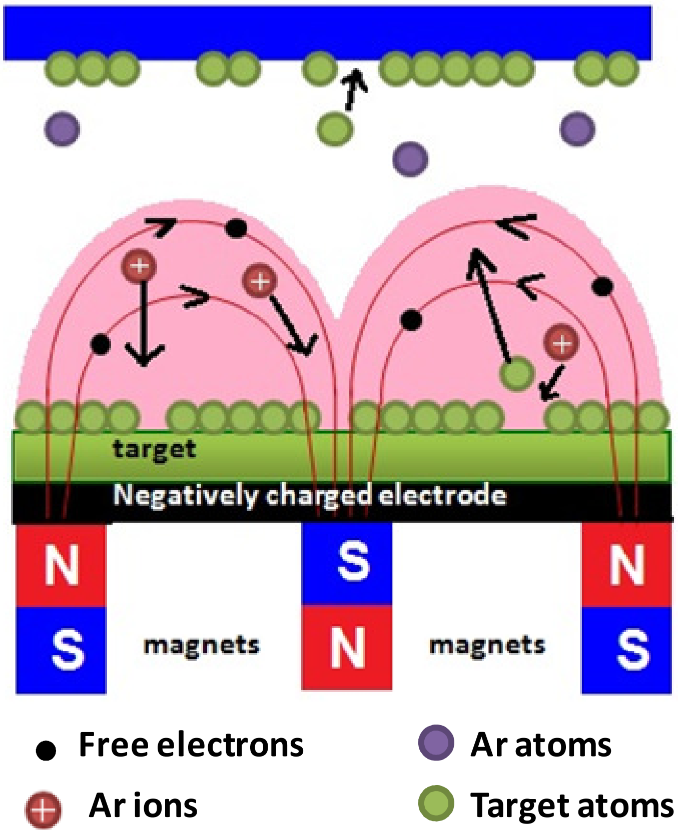

Fig. 5.2. Magnetron sputtering technique.

operating voltages (typically ~500 V) in comparison to basic sputtering modes. Thus DC / RF magnetron sputtering has become the process of choice for thin film deposition for a wide range of applications [103].

Pulsed Magnetron Sputtering (PMS) is another very important technique which has become popular in the recent years. It is well known that DC reactive sputtering of defect-free coatings of insulating materials, particularly oxides, is not feasible due to low deposition rates and the formation of arc at the target. These have adverse effects on the structure, properties and composition of the thin film. Operating the magnetron using pulsed DC supply in the mid-frequency range (10 – 200 kHz) minimizes or eliminates the arc events and stabilizes the reactive sputtering process. Using the PMS process High-quality oxide coatings can be achieved at rates comparable to that of metallic coatings [103].

For this research work, a customized two target magnetron sputtering system made by Hind High Vac was used for the deposition of sensing layers by RF sputtering method on various substrates. The system consists of the following major components:

(i) Stainless steel sputter chamber capable of holding high vacuum ($<10^{-6}$ mbar).

(ii) Turbo molecular pump to evacuate the chamber pressure to $\sim 10^{-6}$ mbar.

(iii) High vacuum valve, vent valve and gas isolation valve

(iv) Digital Pirani gauges for rotary vacuum and digital Penning gauge for high vacuum

(v) Motorized throttle valve to maintain the partial pressure (up to 0.01mbar) of argon to carry out the sputtering operation.

(vi) Two magnetron sources, one each for DC and RF sputtering.

(vii) Pulsed DC and RF power supplies.

(viii) Substrate holder.

(ix) Substrate heating and rotation facility.

(x) Gas manifold with fine control needle valves to feed gas mixture into the sputter chamber.

(xi) Safety devices and interlocks to monitor air pressure, water flow, chamber pressure, DC / RF power during sputtering and so on

The picture of main console and deposition chamber and the block diagram of the sputter system are shown in Fig. 5.3. The vacuum related operations viz. roughing, backing, throttling, high vacuum, gas inlet and venting are controlled by individual valves. All the

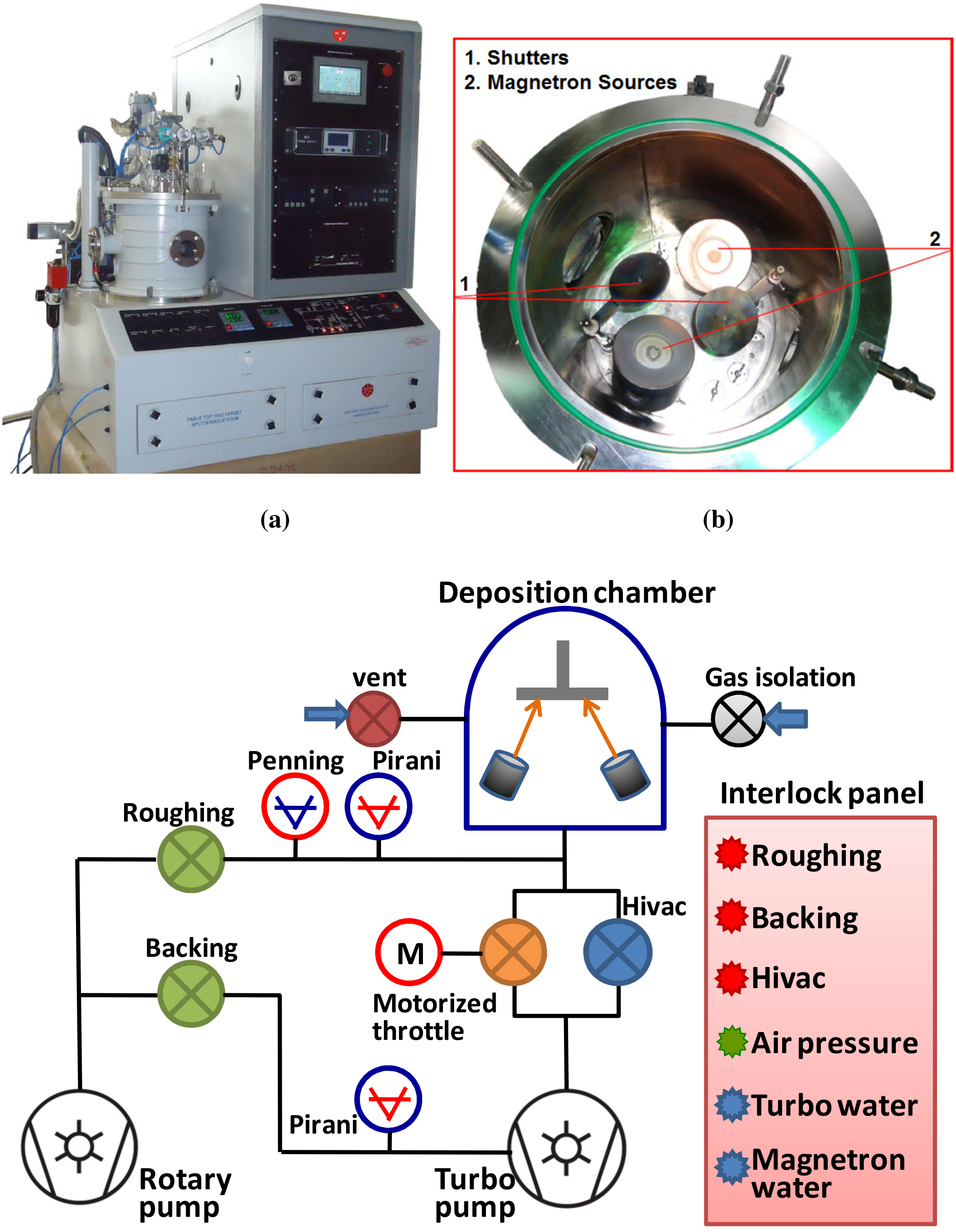

(a) (b)

(c)

Fig. 5.3 (a) Two target sputtering system, (b) sputter chamber and (c) block diagram of the sputtering system with interlocks.

valves are pneumatically operated using a compressor unit. A Programmable Logic Controller (PLC) provides complete automation of the vacuum cycle and various interlocks of the system. Most of the operations can be controlled by Human Machine Interface (HMI) panel. A closed-loop chiller system circulates water for turbo molecular pump, the magnetron heads and outer wall of the deposition chamber. All high purity gases (Ar, O_2, N_2) are routed through the gas purification & control panel and precisely mixed in the desired ratio using a Mass Flow Controller (MFC), prior to feeding into the deposition chamber.

5.1.2 Deposition of ZnO films

The optimization of sputter parameters for thin films was performed using ZnO. ZnO is a multifunctional semiconducting metal oxide and one of the most promising materials for gas-sensing application, next to tin oxide. ZnO belongs to the II–VI group and wurtzite ZnO has a hexagonal structure. It is a wide direct band gap (3.37 eV) semiconductor and has a large exciton binding energy (60 meV). In 1959, Heiland reported the gas sensitive behavior of ZnO's conductivity [104]. Since then ZnO has gained significant momentum in the field of gas sensors.

As ZnO is a binary oxide, RF magnetron sputtering was chosen for the thin film deposition. As discussed earlier, RF magnetron sputtering is one of the most popular and preferred growth techniques for thin films due to its low cost, low operating temperature, good reproducibility and compatibility with surface micromachining technologies. For process optimization, both sintered ZnO target (99.99%) and powder target were used. Sintered targets of 2″ circular discs with a copper back plate were procured commercially. Corning glass was used as substrates. The glass substrates were thoroughly cleaned with organic solvents and dried before loading in the sputtering system. The substrates were fixed on the stainless steel (SS) substrate holder above which a disc heater was placed to facilitate substrate heating. The temperature of the substrate was monitored with thermocouple attached close to the substrate. The sputtering chamber was evacuated to ~1.5×10^{-5} mbar by turbo molecular pump prior to the introduction of the Ar–O_2 gas mixture. The flow rates of Ar and O_2 were controlled by MFCs at 30 and 20 sccm respectively and the gases were mixed in a gas manifold and fed to the sputter chamber through SS tubing. After the chamber was evacuated to high vacuum, a throttle valve was used to adjust the chamber pressure during sputtering. Once the plasma was struck, the power and the pressure were adjusted to the desired conditions. The reflected power was tuned to a minimum value by automatic tuning of matching network. The ZnO target was sputter cleaned for 10 min prior to the start of deposition. Pre-sputtering enabled the removal of any contamination from the target surface and helped to reach the stable plasma conditions. Sputtering was initiated by opening the shutter above the magnetron. Substrate holder was rotated (~10 rpm) to enable uniform film deposition. Although no external substrate heating was provided during the deposition process, the substrate temperature rose up to a maximum of 50 °C due to self-heating in plasma. No post annealing was carried out on the films.

Chamber pressure is one of the main parameters to be optimized for each material to be sputtered. Deposition rate increases at lower sputter gas pressure as the sputtered atoms leaving the target will undergo fewer collisions; at the same time sustaining the plasma is difficult below 10^{-2} mbar [105]. After a number of runs, the sputter pressure for ZnO deposition was optimized at $1 - 2 \times 10^{-2}$ mbar. RF power is another parameter which influences the sputter rate and quality of the films. Higher RF power leads to high deposition rate as the ions bombarding the target will have a higher energy. High power also results in cracking of sputter target and damaging the substrate surface, especially in the case of insulating targets. Low sputtering power results in amorphous films as the ejected species have low kinetic energy, which is not sufficient for the arrangement and crystallization of the films. In order to optimize the sputter power, the films were grown at various RF power while keeping the other parameters same. The crystalline structure and orientation of these films were investigated by X-ray diffraction (XRD). The surface morphology and roughness of the films were characterized by Atomic Force Microscopy (AFM).

5.1.3 Characterization of ZnO films

5.1.3.1 X- ray Diffraction of ZnO films

XRD is a versatile, non-destructive analytical tool for the identification and quantitative determination of the various crystalline compounds, known as 'phases', present in solid materials and powders [106]. X-ray diffraction is based on the constructive interference of monochromatic X-rays on a crystalline sample. X-rays with a wavelength similar to the

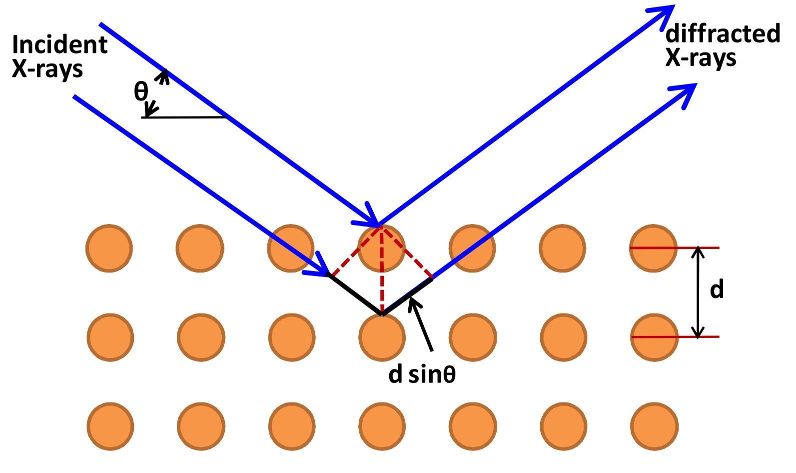

Fig. 5.4. Schematic diagram showing diffraction of X-rays by a crystal.

distances between the crystal planes can be reflected such that the angle of reflection is equal to the angle of incidence. This is known as ‘diffraction´, which is described by Bragg's Law ($n\lambda = 2d \sin \theta$). As shown in Fig. 5.4, the interaction of the incident X - rays with the sample produces constructive interference when the conditions satisfy Bragg's law . By using X-rays of known wavelength λ and measuring the incident angle θ, the spacing d of the planes in a crystal can be determined through Bragg’s law.

Fig. 5.5 shows the XRD patterns of ZnO thin films grown at different RF power. The XRD measurements revealed that all of the obtained films were polycrystalline with hexagonal structure and had a preferred orientation with c-axis perpendicular to the substrate (JCPDS file no. 36–1451). Though higher power yielded a thicker film for the same deposition time, it is not preferred as it would cause the ZnO polycrystalline structure to be randomized within the thin film. Also, high RF power induces faster reaction rate and it damages the surface, leading to poor crystalline quality. Too low RF power results in amorphous films due to low kinetic energy of the target atoms. Accordingly, the RF power must be optimum to have an

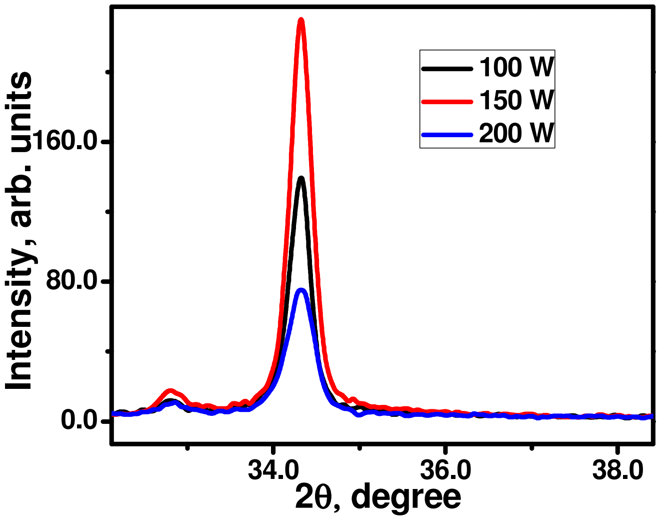

Fig. 5.5. X-ray diffraction pattern of ZnO films as a function of RF power; target was commercial sintered ZnO target.

efficient nucleation and growth in the preferred orientation. As it is evident from the XRD spectrum in Fig. 5.5, the optimum power for sintered ZnO target is observed to be ~150 W above which the (002) peak intensity reduces and also the peak is broadened.

Many applications demand tailor-made properties for the MOX sensing layers, which is not possible if commercial sintered targets are used. One simple approach is to make a composite target consisting of either hot-pressed and sintered metal and oxide powders together or of the mixed powders without sintering. Main advantage of using powder targets is that it is easier to get a variety of compositions using a mixture of the complex compounds without sintering the target materials. The drawback to powder targets is lower sputtering rates than those of commercial sintered targets.

In order to optimize the sputter process for powder targets, hand pressed powder targets were made using commercial ZnO nanoparticles. The working pressure, Ar : O_2 ratio and deposition time were optimized at 2×10^{-3} mbar, 3:2 and 2 hour respectively. Although no external substrate heating was provided during the deposition process, the substrate temperature rose up to a maximum of 50 °C due to self-heating in plasma. No post annealing was carried out on the films.

The XRD spectra of the films grown at different RF power are shown in Fig. 5.6. Beyond 100 W, the target developed cracks. So the maximum power was restricted to 100 W for powder targets. While ZnO powder contained crystals in random directions with multiple peaks, sputtered ZnO films were oriented normal to substrate surface, indicating a preferential orientation along the c-axis as in the case of commercial target [29].

Fig. 5.7 shows the effect of heating the substrate during the deposition. It is seen that even at a low RF power of 50 W, highly oriented films could be achieved due to the thermal energy provided by the hot substrate. In general, it is preferred to use a low temperature process for the deposition of sensing layers. Hence, substrate heating was used only where it was absolutely necessary to get crystalline films of preferred orientation.

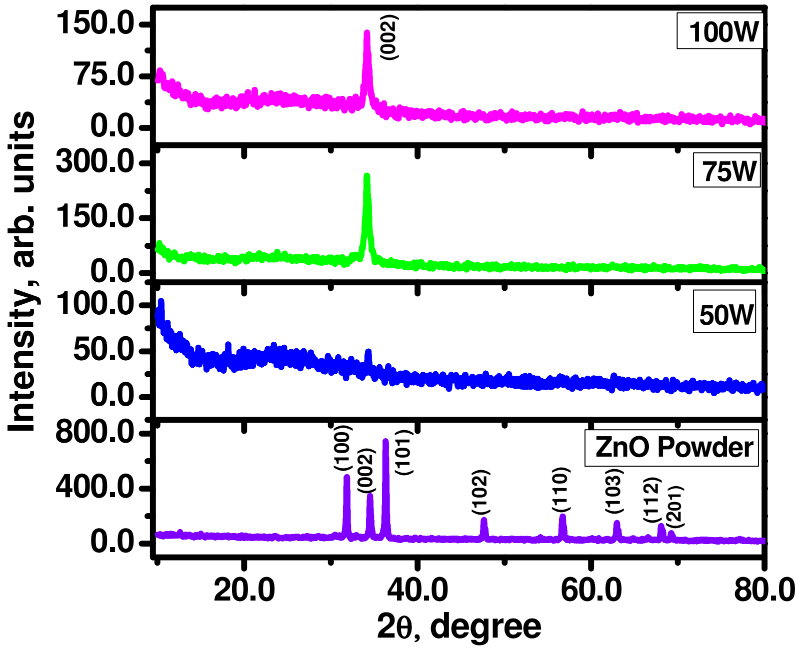

Fig. 5.6. X-ray diffraction pattern of ZnO films as a function of RF power using powder target.

5.1.3.2 Surface characterization by Atomic Force Microscope

AFM utilizes a pointed probe moving over the surface of a sample in a raster scan. Fig. 5.8 shows the schematic of AFM working principle. The AFM probe is basically a tip at the end of a cantilever which bends in response to the force between the tip and the sample surface atoms. As the cantilever deflects, the light from a laser is reflected onto a four segment

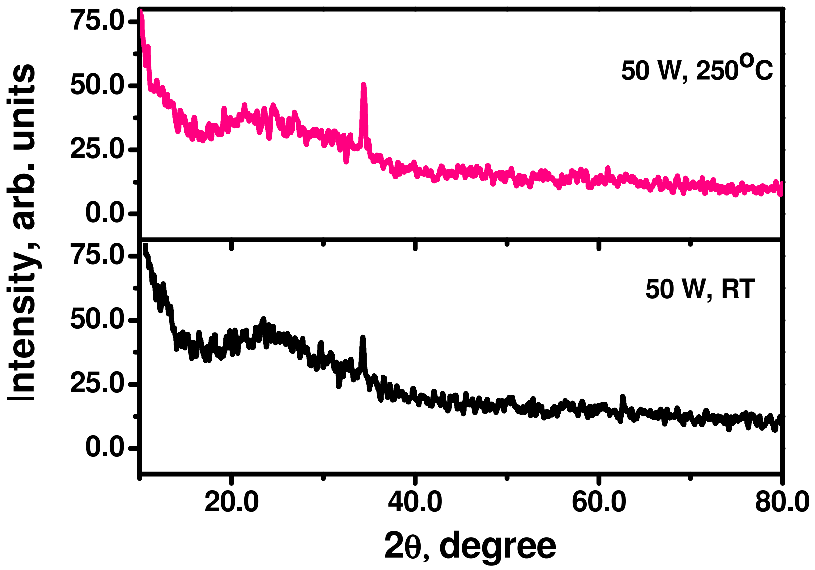

Fig. 5.7. XRD pattern of ZnO films grown at room temperature and at a substrate temperature of 250°C.

position sensitive photodiode matrix. By measuring the difference signal of the diode matrix, changes in the bending of the cantilever can be measured. Since the cantilever obeys Hooke's law for small displacements, the interaction force between the tip and the sample can be determined [106].

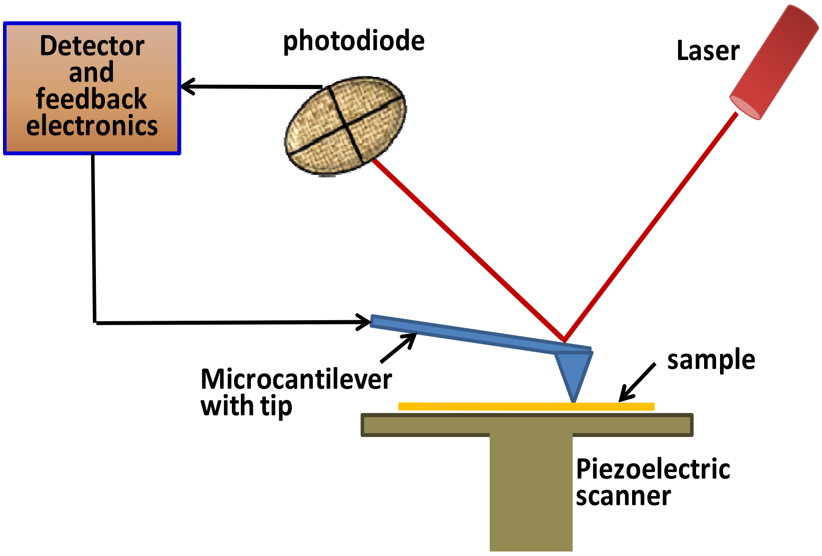

Fig. 5.8. Schematic showing AFM working principle.

Figs. 5.9 and 5.10 show the AFM images of ZnO films deposited using commercial and powder target at various RF power. From these figures, it is apparent that there is no significant morphology difference between films deposited using commercial and in-house made powder targets. The AFM pictures clearly show that the average size of the grains is of the order of nanometers and they are homogeneous, uniformly distributed over the surface with good connectivity between the adjacent particles. Average grain size is < 200 nm and the surface roughness is <50 nm for all the films. The grain size and the width of the necks between the grains are the main parameters that control the gas sensing properties in MOX

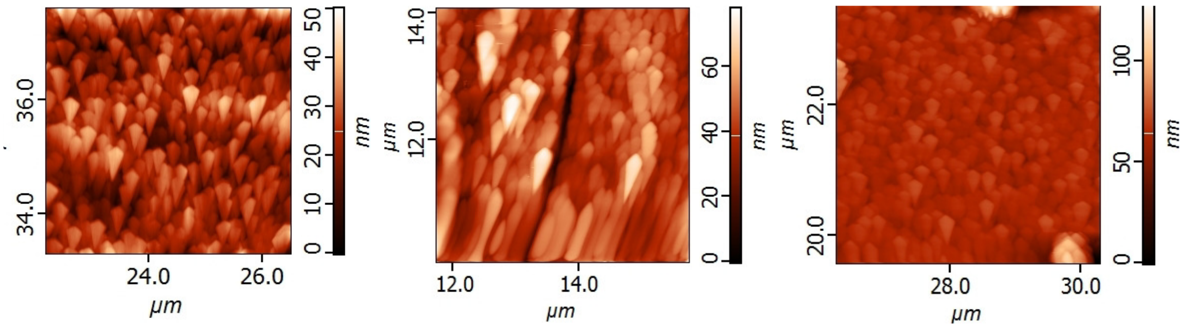

(a) **(b)** **(c)**

Fig. 5.9. AFM images of ZnO films grown at (a) 100 W, (b) 150 W and (c) 200 W using commercial target.

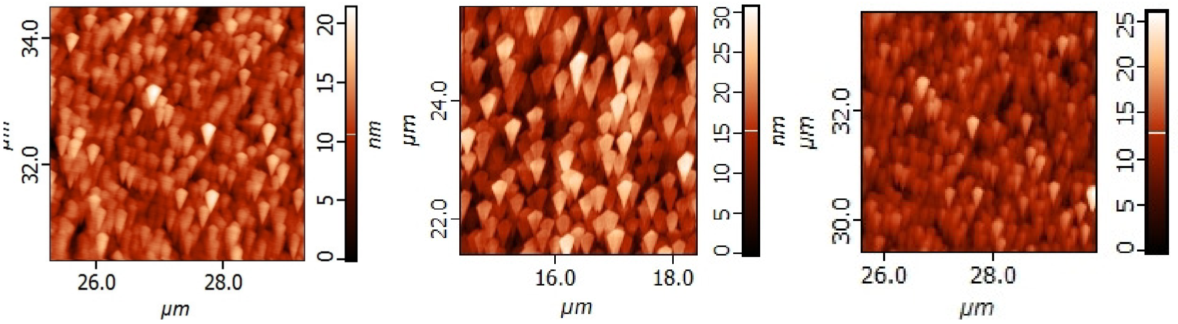

(a) **(b)** **(c)**

Fig. 5.10. AFM images of ZnO films grown at (a) 50 W, (b) 75 W and (c) 100 W using powder target.

films. In the case of thin film gas sensors, the decrease in film thickness and grain size improve the sensing performance owing to large surface area. However, the surface area must be balanced with the need for sensor stability, since high surface area structures are inherently unstable due to their high surface energy [107]. As the average grain size of all the deposited films is between 50 – 200 nm, it is expected that they would offer optimum and stable sensing performance.

5.2 Thermal Evaporation method for contact electrodes

Thermal evaporation technique is widely used for the deposition of thin films of metals, alloys and many compounds. A thermal evaporator uses resistive heater to melt the source material and increase its vapor pressure to a useful range for condensation on the cold substrate. A schematic diagram of the thermal evaporation system is shown in Fig. 5.11. In general, the evaporation is carried out in high vacuum (better than 10^{-5} Torr) to inhibit the formation of oxides and incorporation of impurities in the deposited film. Furthermore, at pressures as low as 10^{-5} Torr, the mean free path of metal atoms is quite high hence the particles move in straight lines from the evaporation source towards the substrate with minimal scattering [108]. The quality of the deposited film depends on the purity of the source material and the order of the vacuum.

For this research work, Hind Hivac make dual filament thermal evaporation system was installed for the deposition of metal layers. The system comprises of:

(i) SS Vacuum Chamber.

(ii) Dual LT evaporation assembly with source shutter and substrate holder.

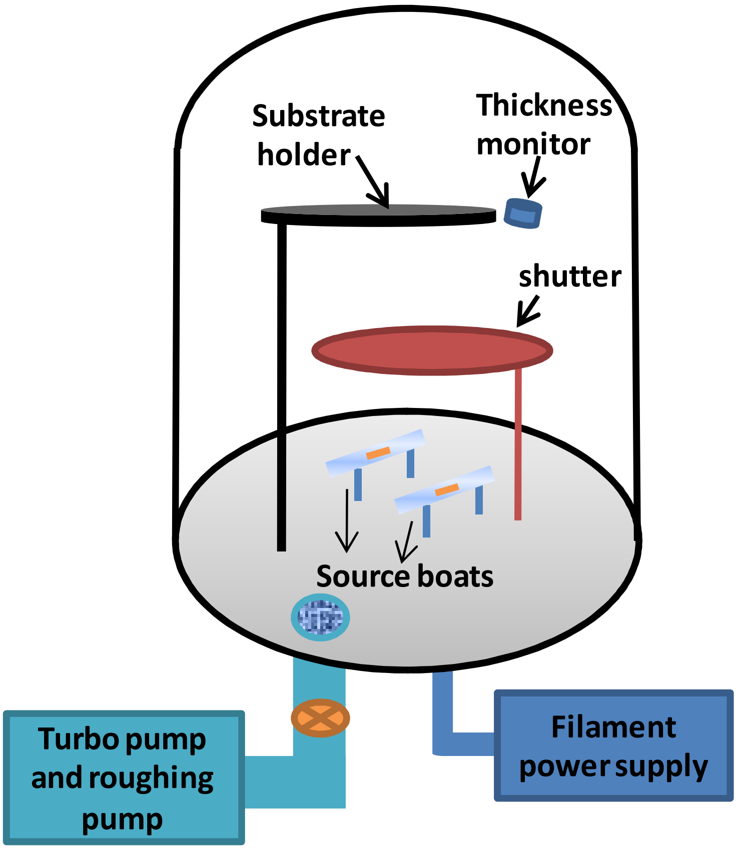

Fig. 5.11. Schematic of thermal evaporation system.

(iii) Thyristor controlled LT power supply.

(iv) Rotary and turbo molecular pump vacuum pumping system with high vacuum valve, roughing and backing valves.

(v) Pirani and penning gauge heads with digital gauge controllers.

(vi) Safety devices: Over load protection, safety panel switches inside the cabinet, vacuumswitch, circuit breaker in AC mains line.

(vii) Digital thickness monitor.

The block diagram of thermal evaporation system and the picture of evaporation chamber are shown in Fig. 5.12 (a) and (b) respectively. Several test runs were carried out using high purity gold wire (99.95%, 0.5 mm dia.) for the deposition of gold thin films on glass substrates. The optimized deposition parameters are given below:

(i) Deposition vacuum - $< 1 \times 10^{-5}$ mbar.

(ii) Deposition rate - 10 – 20 Å / s

(iii) Thickness – 200 – 300 nm.

(iv) Substrate temperature – room temperature.

This system was used to deposit sensing electrodes of gas sensors using inter-digitated shadow masks.

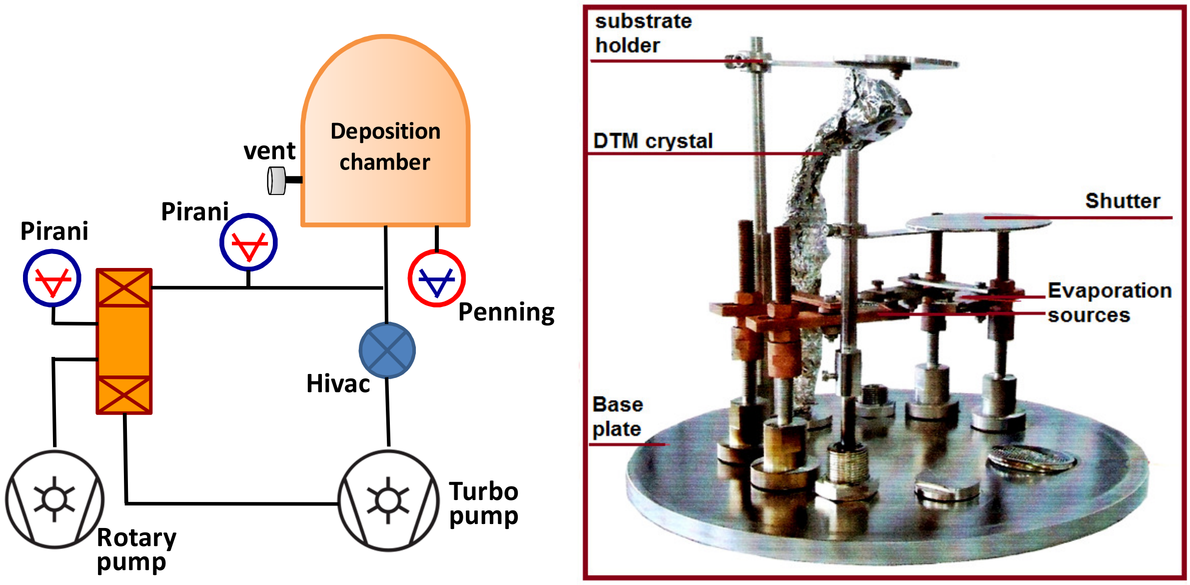

(a) (b)

Fig. 5.12. Thermal evaporation system - (a) Block diagram with interlocks and (b) picture of evaporation chamber.

CHAPTER 6: SYNTHESIS AND CHARACTERIZATION OF DOPED ZINC OXIDE FILMS

As discussed in the previous section, zinc oxide is an interesting II–VI compound semiconductor with a wide band gap of 3.37 eV and a large exciton binding energy of 60 meV. It is a unique material that exhibits both semiconducting and piezoelectric properties and has a wide range of applications such as surface acoustic wave (SAW) devices, transparent conducting oxide electrodes, solar cells, blue / UV light emitting devices, gas sensors, etc. [109]. In recent years, ZnO has become a potential gas sensor material owing to its easy synthesis procedure, good electrical properties and in particular its compatibility with silicon leading to MEMS based chemical sensors [110].

The morphology-controlled synthesis of ZnO nanostructures for gas sensing has been extensively studied, since reactions at grain boundaries and complete depletion of carriers in the nano grains can strongly modify the material transport properties. The morphology of ZnO can be varied from nanoparticles, nanowires, nanorods, nanoflowers, nanoneedles to nanobeads by choosing appropriate synthesis methods and preparation conditions [111]. Among these ZnO morphologies, nanocrystalline thin films exhibit better sensitivity and reproducibility for gas sensing applications, in comparison with other types of ZnO sensors [112, 113]. Most of the nano structures are placed randomly on the substrate while thin film deposition has better control and uniformity of the nanoparticles. Moreover, thin films are more compatible with the micro fabrication technology and batch production. The following sections describe the synthesis and material characterization of ZnO based systems studied for this research work.

6.1 Cu doped ZnO films

It is well known that ZnO thin films have a large number of point defects (such as oxygen vacancy, zinc interstitial, zinc vacancy, oxygen interstitial, etc.); hence they are inherently n-type semiconductors [114]. Doping with a suitable impurity is a well known method in order to tune the structural and electrical properties of sensing materials. Nanto *et al.* [115] demonstrated that doping of ZnO films resulted in a significant change in the resistance, higher gas sensitivity and lower operating temperature. The most commonly used metallic dopants in ZnO based systems are Al, Co, Cu, Ga, Ni, Sn, etc. [116, 117]. Due to its similar electronic shell structure, Cu has many physical and chemical properties similar to those of Zn. Substitution of copper into the ZnO lattice has been shown to improve the gas sensitivity among other properties [118]. For this thesis work, Cu doped ZnO (CZO) films with various doping concentrations have been synthesized and characterized and later explored for H_2S sensing.

6.1.1 Thin film deposition by RF sputtering

Sputtering targets were prepared in-house by mixing powders of ZnO and Cu. For this purpose, Cu powder was synthesized by dissolving 1:1 molar ratio of commercially available Zn powder and $CuSO_4\cdot 5H_2O$ in 20 ml distilled water and stirring for 30 minutes. The residual Cu powder was washed with water for two or three times and dried at 80 ^{o}C for one hour. Stoichiometric quantities of commercial ZnO powder and synthesized Cu powder were mixed and ground for few hours. The sputtering target was prepared by spreading the ground powder evenly in a copper holder of 2″ diameter, having a trench of ~1.5 mm depth and pressing manually with a solid piece of SS to make it compact. No further processes were involved in the target preparation.

Thin films of $Zn_{1-x}O$: Cu_x were grown on glass substrates in sputter up configuration at a fixed target-to-substrate separation of ~45 mm. Before loading into the sputtering chamber, the glass substrates were ultrasonically cleaned with methanol, acetone and isopropanol in sequence and rinsed with distilled water and dried. The sputtering chamber was evacuated to $\sim 1.5\times 10^{-5}$ mbar prior to the introduction of the Ar–O_2 gas mixture. The flow rates of Ar and O_2 were controlled by MFCs at 30 and 20 sccm respectively. The working pressure, RF power and deposition time were optimized and fixed at 2×10^{-2} mbar, 100 W and 2 h respectively. Substrate holder was rotated (~10 rpm) to enable uniform film deposition. Although no external substrate heating was provided during the deposition process and no post annealing was carried out on the films.

6.1.2 Structural and morphological studies of thin films

The typical XRD patterns of undoped and doped ($Zn_{1-x}O$: Cu_x) films with x = 0.01, 0.02 and 0.05 are shown in Fig. 6.1. Both films (pure and doped) are polycrystalline with a structure that belonged to the ZnO hexagonal wurtzite type. Since Cu has similar ionic radius and electronic shell structure as Zn, Cu ions can replace either substitutional or interstitial Zn atoms in the ZnO lattice. In Fig.6.1 (a), no extra peaks corresponding to Cu, oxides of Cu or Cu related secondary phases are seen, which may be attributed to the substitution of Cu ions into the Zn lattice site rather than interstitial ones. While ZnO powder contains crystals in random directions with multiple peaks, sputtered ZnO films contain nanograins which are oriented normal to substrate surface, indicating a preferential orientation along the c-axis

[119]. It is seen from Fig. 6.1 (b) that the (002) peak becomes sharp with Cu doping. The improvement in c-axis orientation with doping may be due to the fact that a reasonable quantity of Cu atoms exists in ZnO lattice site, sharing the oxygen with Zn atoms and resulting in minimal deformation in the lattice with a very little shift in the (002) peak position. Similar small shift in (002) peak position has been observed in previous studies on Cu doped ZnO (CZO) [119 - 121].

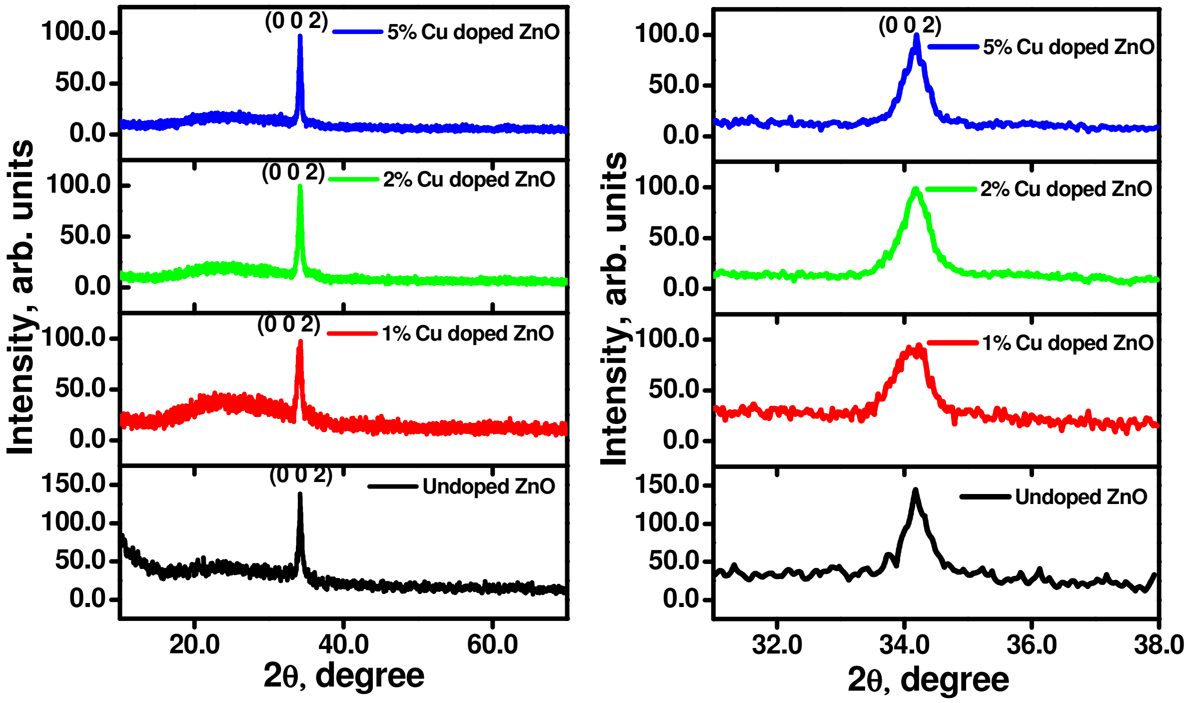

(a) (b)

Fig. 6.1. XRD patterns of undoped and CZO films (a) showing preferential c-axis orientation and (b) sharpening of (002) peak with Cu doping.

Average crystallite size of the as grown films is calculated from the diffraction line width of (002) peak based on Debye Scherrer relation [106]:

$$D = 0.9\lambda / \beta \cos\theta \qquad (6.1)$$

where D is the average particle size, λ is the wavelength of X-rays, β is the angular peak width at half maximum in radian along (002) plane, and θ is Bragg's diffraction angle.

The peak positions Full Width Half Maximum (FWHM) of (002) peak and particle size for pure and CZO films are listed in Table 6.1. As seen from the table, the variation in (002) peak position is very small, which could be attributed to the incorporation of Cu ions into the Zn lattice site. However, no systematic variation is observed in peak position with doping concentration. The FWHM of (002) peak decreases with Cu content, indicating that addition of small amount of Cu improves the crystallinity. The crystallite sizes of all the samples are of the order of 16 ± 3 nm and increase with Cu content. This confirms that the Cu doped ZnO samples are nanomaterials and the crystal size depends on the doping level.

Table 6.1. (002) peak position, FWHM and crystallite size of undoped and Cu doped films derived from XRD spectra.

Sample	(002) peak, °2θ	FWHM, degree	Crystallite size (D), nm
undoped	34.195	0.5362	15
1% Cu	34.099	0.6348	13
2% Cu	34.172	0.5369	15
5% Cu	34.168	0.4349	19

The AFM micrographs of surface morphology of the undoped and Cu doped ZnO films are shown in Fig. 6.2. All the films have a uniform columnar structure. The width of a column is <200 nm as seen from the AFM images. The films show fully coalesced, uniformly distributed ZnO grains. There is no observable morphological difference between the undoped and doped ZnO films.

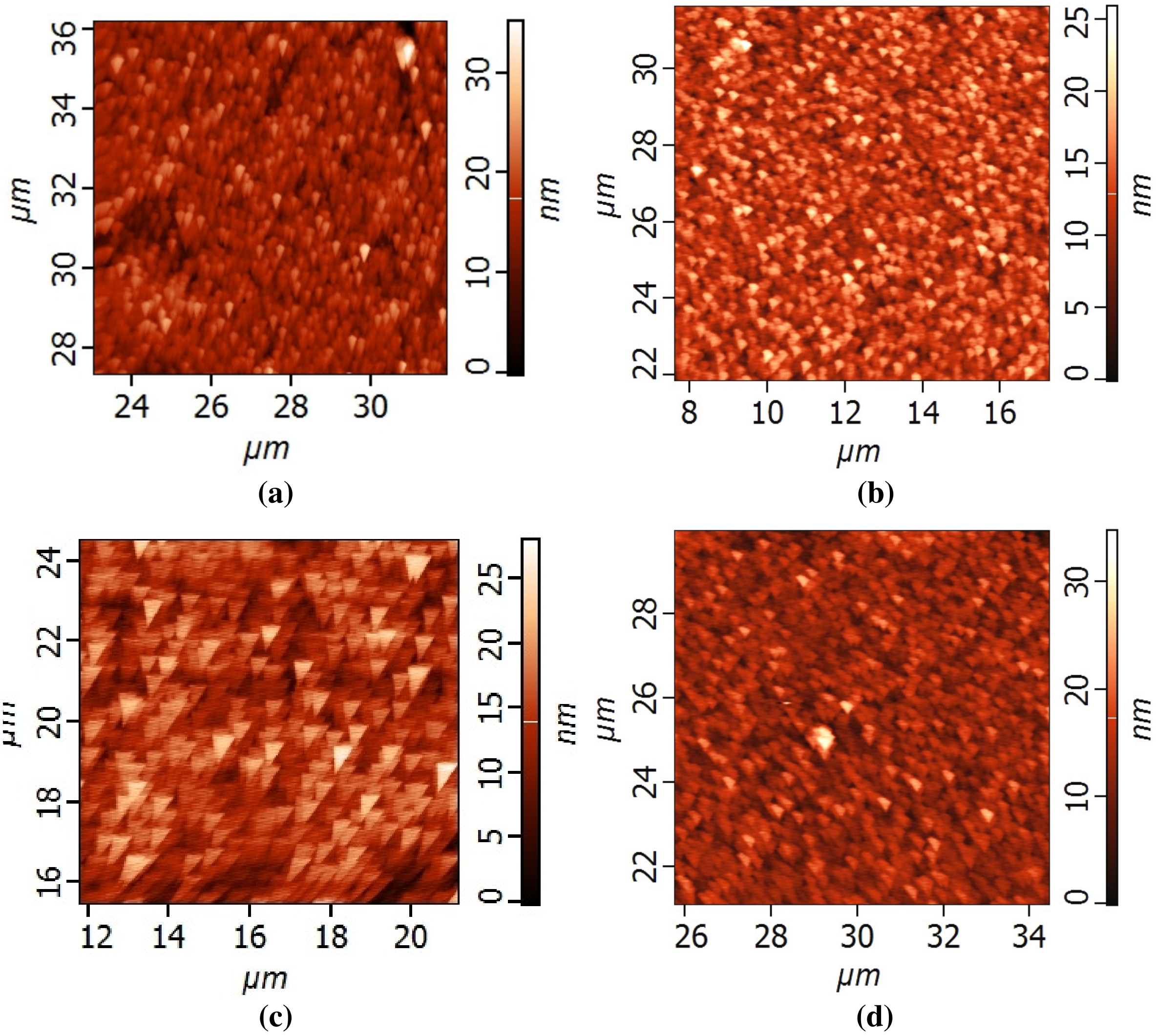

Fig. 6.2. Atomic Force Micrographs of (a) undoped, (b) 1%, (c) 2% and (d) 5% Cu doped ZnO films on glass substrate.

For a better understanding of chemical composition and bonding in CZO structures, X-ray photoelectron spectroscopy (XPS) analysis is carried out. XPS is a popular surface-sensitive quantitative spectroscopic technique which provides the elemental composition, oxidation state, chemical state and electronic state of the constituent elements that exist within a material [106]. XPS spectra are obtained by irradiating a solid surface with monochromatic X-rays which stimulate the emission of core level electrons from the top 1-10 nm of the material being analyzed. A photoelectron spectrum is recorded by counting ejected electrons over a range of electron kinetic energies. From the binding energy and intensity of the photoelectron peaks, the elemental identity, chemical state and quantification of all surface elements can be determined (except for hydrogen).

Fig. 6.3 (a) shows the XPS survey spectrum and Figs. 6.3 (b), 6.3 (c) and 6.3 (d) show XPS spectra of the O-1s, Zn-2p, and Cu-2p core level regions respectively of the 2% CZO film on

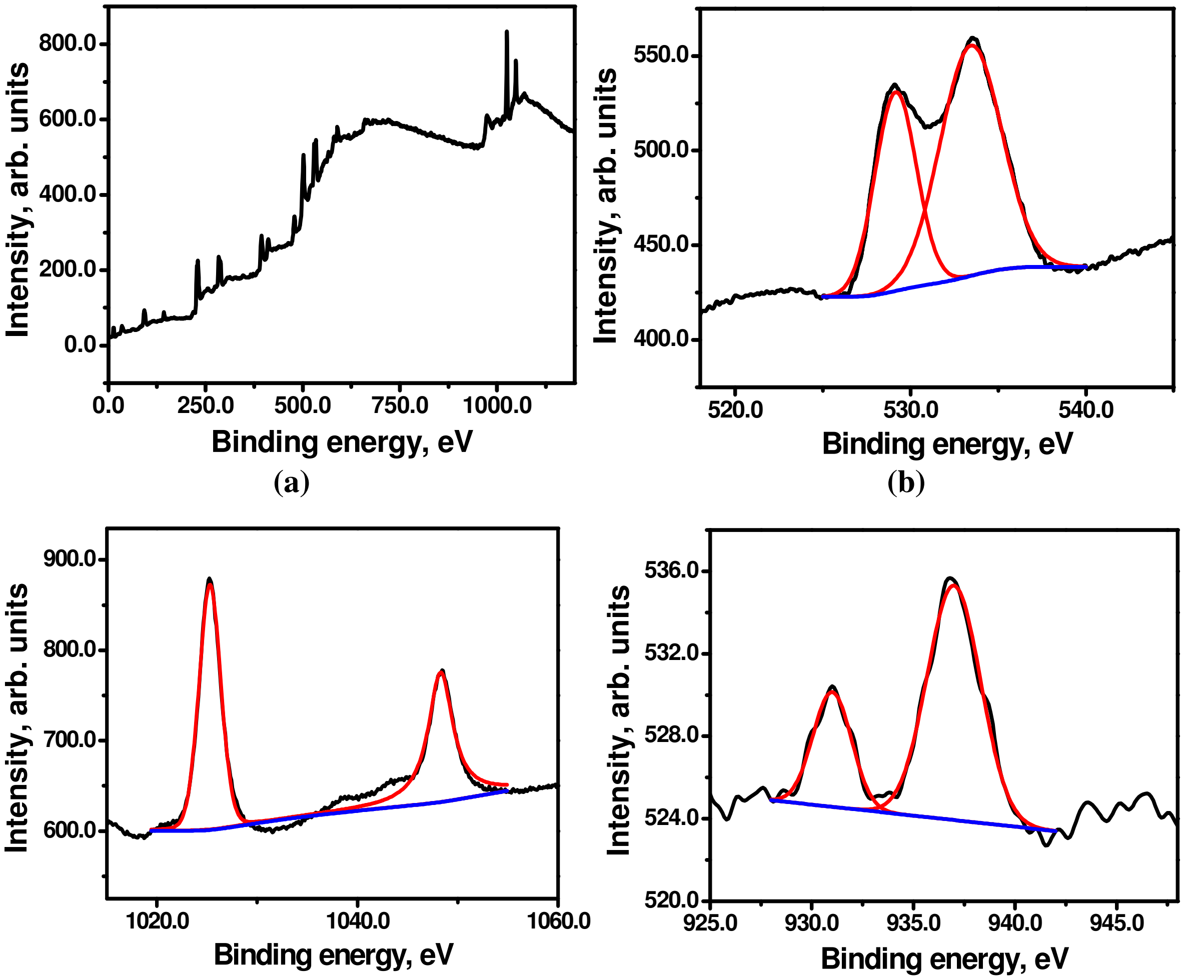

(a)

(b)

(c)

(d)

Fig. 6.3. (a) XPS survey spectra of 2% CZO film, (b) XPS spectra of O 1s, (c) XPS spectra of Zn 2p and (d) XPS spectra of Cu 2p.

glass substrate. The survey scan from 0 to 1200 eV shows multiple peaks corresponding to C, O, Cu and Zn as seen in Fig. 6.3 (a).The broad asymmetric curve of O 1s (Fig. 6.3 (b)) can be fitted to two peaks with binding energies at 529.15 eV and 533.46 eV. The distinctive peak at 529.15 eV is assigned to the surface lattice oxygen (O^{2-}) in a metal-oxide framework and the peak at 533.46 eV the presence of surface-adsorbed oxygen species such as O^- [122]. Fig. 6.3 (c) shows that Zn has a doublet corresponding to Zn $2p_{3/2}$ at 1025.29 eV and $2p_{1/2}$ at 1048.29 eV and is in the form of +2 oxidation state. Similarly, Cu $2p_{3/2}$ and Cu $2p_{1/2}$ peaks (Fig. 6.3 (d)) appearing at 930.99 eV and 936.99 eV indicate the existence of +2 oxidation valence state of Cu in CZO films [123].

6.2 Ga doped ZnO films

In order to accomplish effective doping, the dopant atoms should substitute the host atoms in the lattice. In that context, Ga^{3+} which has an ionic radius of 0.47 Å (ionic radius of Zn is 0.6 Å), is one of the best candidates for n-type doping of ZnO. Also Ga doped ZnO (GZO) is more stable with respect to oxidation due to Gallium's greater electronegativity. In addition, the electrical and optical properties of GZO thin films are greatly enhanced as the covalent bond lengths of Ga–O and Zn–O are nearly equal [124]. These properties have been extensively exploited for a variety of applications such as TCO, field emission devices, solar cell, LED, etc. [125]. Recently, GZO has attracted considerable attention for gas sensing applications. GZO has been reported to enhance the sensing for CO, H_2 and humidity [126 - 128]. In this context, GZO films with various doping concentrations have been synthesized and characterized and later investigated for H_2S sensing.

6.2.1 Thin film deposition by RF sputtering

Sputtering targets were prepared in-house using commercial ZnO powder and Ga_2O_3 powder synthesized by low temperature polyol route. Stoichiometric quantities of ZnO and Ga_2O_3powders were mixed and ground for few hours. Sputter target was prepared by spreading the ground powder on a copper holder, similar to the procedure explained for Cu doped ZnO. Thin films of $Zn_{1-x}O$: Ga_x (x = 0 to 0.05) were grown on glass substrates using a RF magnetron sputtering system. Base pressure of the sputtering chamber was ~1.5×10^{-5} mbar. The working pressure, RF power, substrate temperature, Ar : O_2 ratio and deposition time were optimized and fixed at 2×10^{-2} mbar, 100W, 100º C, 3:2 and 2 h respectively. Substrate holder was rotated (~10 rpm) to achieve uniform film deposition.

6.2.2 Structural and morphological studies of thin films

The typical XRD patterns of undoped and doped ($Zn_{1-x}O$: Ga_x) films with x = 0.01, 0.03 and 0.05 are shown in Fig. 6.4. All the films (undoped and doped) have a hexagonal wurtzite structure with a strong Bragg reflection corresponding to (002) orientation. The ionic radius of Ga^{3+} and Zn^{2+} is 0.47 Å and 0.6 Å respectively. The covalent bond lengths of Ga-O and Zn-O are 1.92 Å and 1.97 Å respectively. This marginal difference in bond length results in very little distortion of ZnO lattice. This is evident from the XRD patterns (Fig. 6.4), where no extra peaks corresponding to Ga, oxides of Ga or Ga related secondary phases are seen, indicating the substitution of Ga ions into the Zn lattice site rather than interstitial ones. While ZnO powder contains crystals in random directions with multiple peaks, sputtered ZnO films contain nanograins which are oriented normal to substrate surface, indicating a preferential orientation along the c-axis [129, 130].

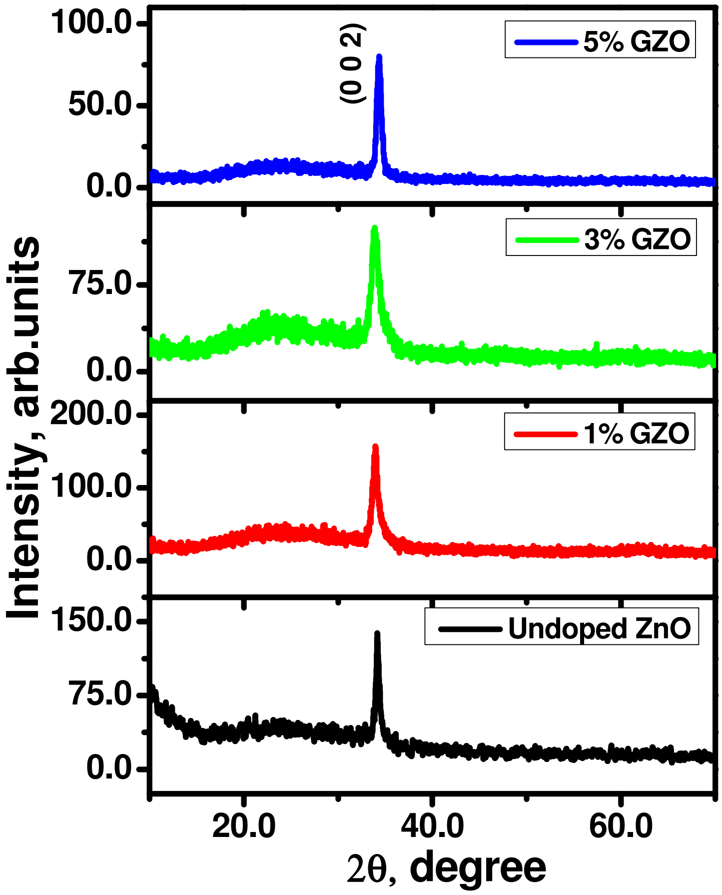

Fig. 6.4. XRD patterns of undoped and GZO films.

Average crystallite size of the as grown films is calculated from the diffraction line width of (002) peak based on Debye Scherrer relation. The peak positions, FWHM and particle size for pure and GZO films are listed in Table 6.2. It was found that the crystallite sizes of all the samples are of the order of 12 ± 2 nm, confirming the nanocrystalline nature of GZO films.

Table 6.2. (002) peak position, FWHM and crystallite size of undoped and Ga doped films derived from XRD spectra.

% doping	(002) peak, °2θ	FWHM, degree	D, nm
0	34.19	0.64	13
1	33.93	0.82	10
3	33.95	1.03	9
5	34.34	0.59	14

The AFM micrographs of surface morphology of the undoped and GZO films are shown in Fig. 6.5. All the films exhibit a rough surface morphology with nearly isotropic lateral features. The presence of columnar growth is evident from the AFM images as expected in the case of highly c-axis oriented sputtered ZnO films [131]. All the films are found to be continuous and dense with an average particle size of <200 nm. The films show fully coalesced, uniformly distributed ZnO grains. Table 6.3 shows the important parameters derived from the AFM images. It is clearly seen that the average roughness increased with doping and 3% GZO films exhibited the maximum average roughness of 8.43 nm and peak-to-peak height of ~67 nm.

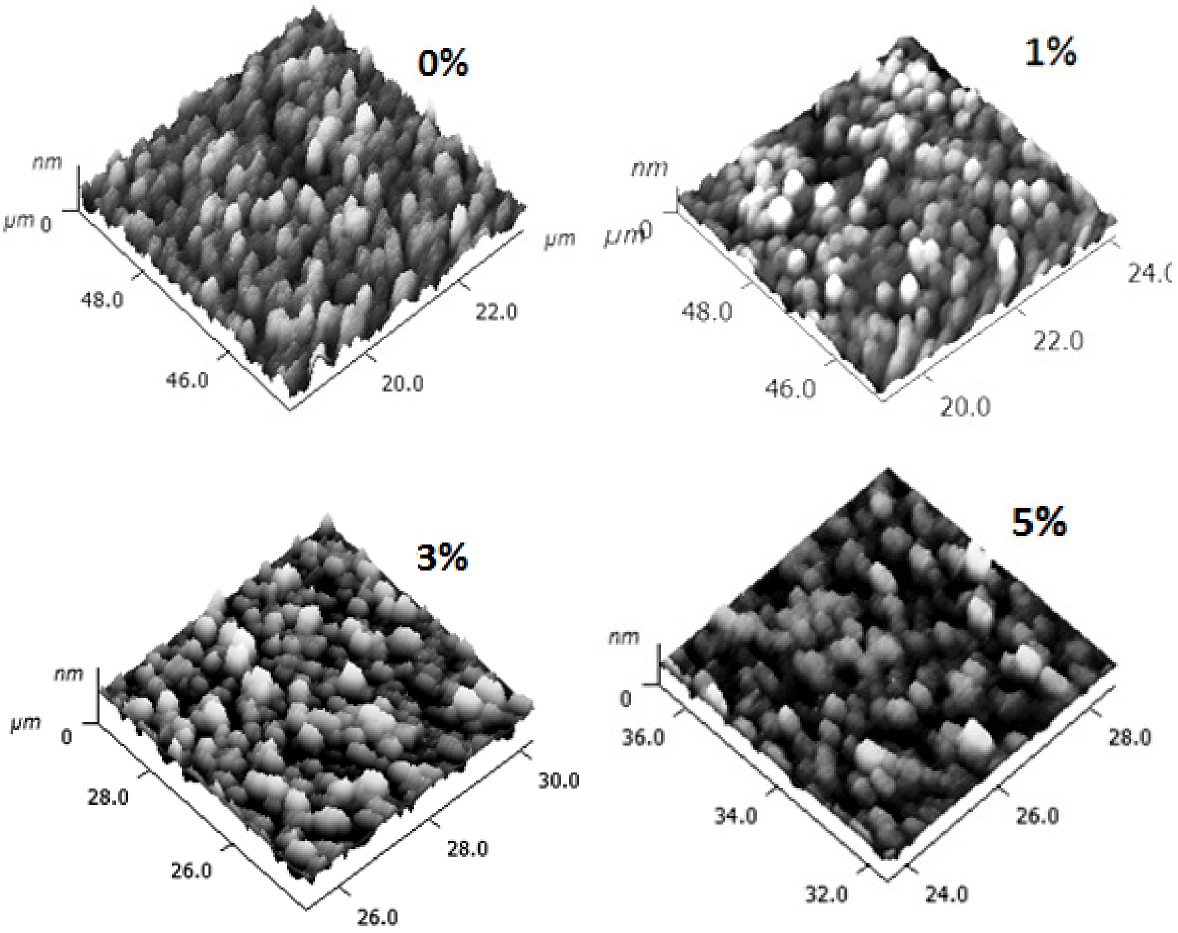

Fig. 6.5. Atomic Force Micrographs of undoped, 1%, 3% and 5% GZO films on glass substrate.

Table 6.3. Roughness and height distribution of undoped and Ga doped ZnO films calculated from AFM images.

Parameter	Undoped	1% GZO	3% GZO	5% GZO
Peak-to-peak, Sy, nm	7.8867	6.77	66.76	49.87
Ten point height, Sz, nm	5.2164	4.11	51.12	47.91
Average Roughness, Sa, nm	0.9932	0.78	8.43	7.08
Root Mean Square, Sq, nm	1.263	0.99	10.69	8.73

In order to evaluate the chemical state and bonding energy of Zn, O and Ga, XPS measurements are performed. Fig. 6.6 (a) shows the XPS survey spectrum and Figs. 6.6 (b), 6.6 (c) and 6.6 (d) show the XPS spectra of Ga $2p_{3/2}$, Zn 2p and O 1s core level regions respectively of the 3% GZO film on glass substrate. The survey scan from 0 to 1200 eV shows multiple peaks corresponding to C, O, Zn and Ga as seen in Fig 6.6 (a). The appearance of Ga spectra (Fig. 6.6 (b)) with peak maxima at 1116.34 eV and the absence of any Ga related peaks in XRD patterns suggest that Ga is incorporated into the ZnO lattice. Fig. 6.6 (c) shows that Zn has a doublet in both undoped and doped films and is in +2 oxidation state. In doped samples, the Zn 2p peaks have shifted slightly towards a higher binding energy. Due to the higher electronegativity of Ga (χ = 1.81) than that of Zn (χ = 1.65), the valence electron density of Zn in Zn–O–Ga bond became lower than that in the Zn–O– Zn bond in the undoped sample. As a result, the screening effect of the Zn is weakened and consequently the binding energy of Zn2p increased in the doped samples [130].

Fig. 6.6 (d) exhibits the deconvoluted O 1s spectra of undoped and 3% GZO films. In both the cases, the broad asymmetric curve of O 1s can be fitted in to two peaks. The lower energy peak (529.53 eV for GZO and 529.32 eV for ZnO) is ascribed to covalently bonded oxygen (lattice oxygen) in ZnO structure while the higher binding energy peak (530.85 eV for GZO and 531.09 eV for ZnO) is attributed to the adsorbed oxygen or oxygen vacancies [124, 132].

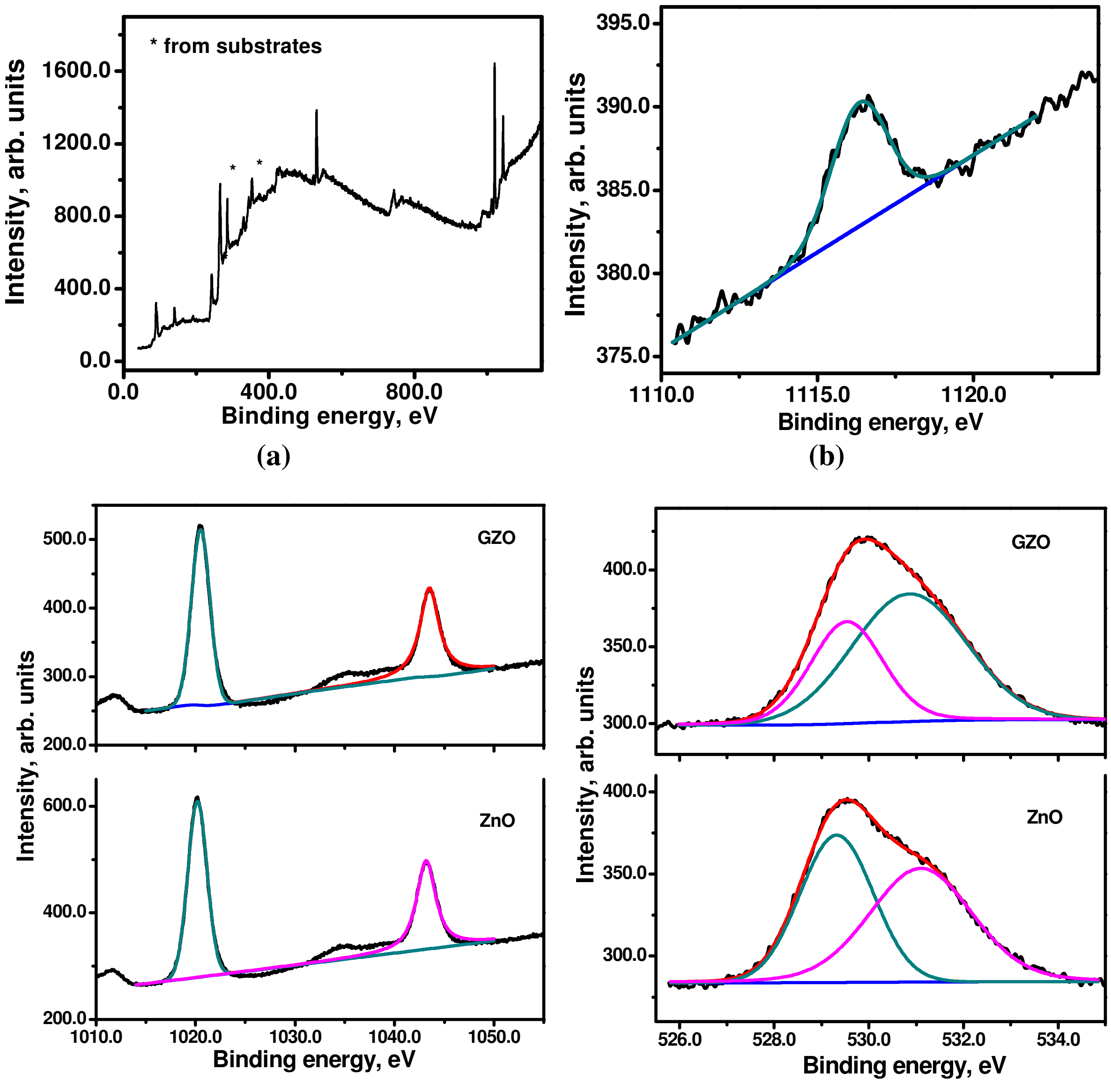

(a) (b)

(c) (d)

Fig. 6.6. (a) XPS survey spectra of 3% GZO film, (b) XPS spectra of Ga $2p_{3/2}$, (c) comparison of Zn 2p spectra of ZnO and GZO and (d) comparison of O 1s spectra of ZnO and GZO.

The increased peak intensity of adsorbed oxygen species in GZO sample indicates that Ga doping has resulted in higher number of oxygen vacancies in the lattice site. Next chapter elaborates the H_2S sensing properties of these films at different operating temperatures and gas concentrations.

6.3 Nitrogen doped ZnO (NZO) films

As discussed earlier, undoped ZnO is known to have large number of point defects such as oxygen vacancy, zinc interstitial, etc., hence it exhibits inherent n-type semiconducting behaviour. Doping with suitable element is a well known technique for enhancing the sensing characteristics of metal oxide gas sensors. Nitrogen is considered as one of the best candidate for achieving p-type conductivity as it has the similar atomic radius and electronegativity as O. On the contrary, many studies report that achieving p-type conductivity with N is not only difficult but the conductivity reverted back to n-type with time due to spontaneous self-compensation from intrinsic donors in ZnO [133, 134]. On the other hand, if N occupies the oxygen sites in molecular form, the relative density of donor defects increases which is favorable for gas sensor operation.

6.3.1 Thin film deposition by RF sputtering

Thin films of NZO were grown on glass substrates using RF magnetron sputtering technique. The working pressure, RF power, substrate temperature, Ar : N_2 ratio and deposition time were fixed at 2×10^{-3} mbar, 100 W, 100 °C, 4:1 and 2 h respectively. In order to compare the effect of N incorporation, undoped ZnO films were also grown using only Ar under the same experimental conditions. All the films were annealed at 400 °C in air for 2 hours.

6.3.2 Structural and morphological studies of thin

XRD patterns shown in Fig. 6.7 (a) reveal that both undoped and NZO films are preferentially oriented along the c-axis with a strong Bragg reflection corresponding to (002) orientation. Absence of any other impurity related peaks indicates that the films have good crystallinity and phase purity. The peak positions, FWHM and particle size for pure and NZO films are listed in Table. 6.2. It is found that the crystallite size increases with N incorporation as evident from the sharpness of XRD peak. This is further corroborated by the AFM image (Fig 6.7 (b)), where the average grain size is of the order of 300 – 400 nm. Further, the films show fully coalesced, uniformly distributed columnar ZnO grains.

Fig. 6.8 (a) shows O 1s spectrum of NZO film. The broad O 1s spectrum is composed of two components located around 529.5 eV and 530.4 eV corresponding to covalently bonded oxygen and adsorbed oxygen respectively. Similar to GZO, higher peak intensity of adsorbed

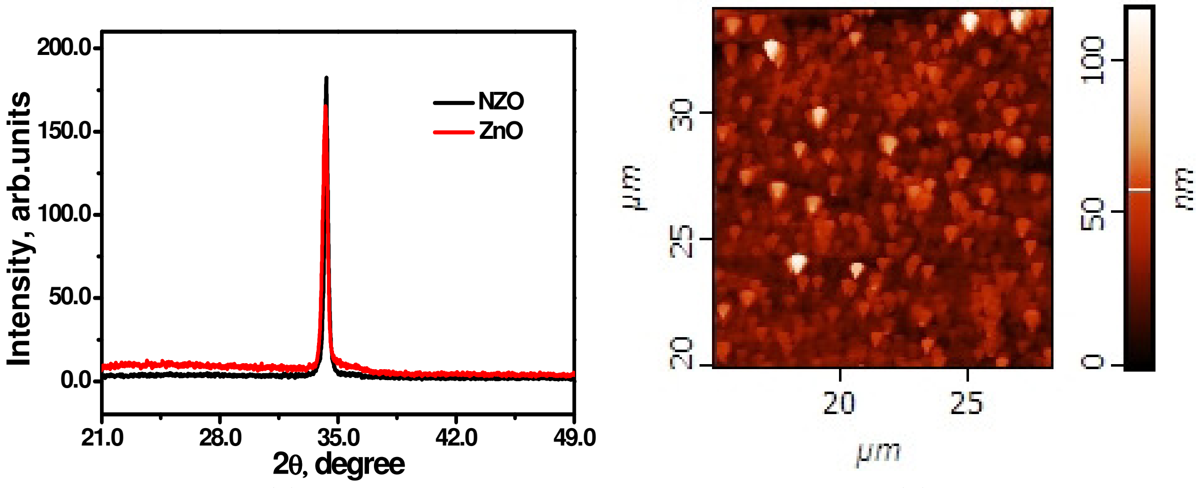

(a) (b)

Fig. 6.7. (a) XRD patterns of undoped and NZO film; (b) AFM image of NZO film.

Table 6.4. (002) peak position, FWHM and crystallite size of undoped and N_2 doped films derived from XRD spectra.

Sample	(002) peak, °2θ	FWHM, degree	D, nm
Only Ar	34.24	0.357	23
1:4 (O_2:Ar)	34.31	0.274	30

oxygen indicates that N substitution has resulted in a higher number of oxygen vacancies in the lattice site. XPS spectra of nitrogen-doped ZnO films (Fig. 6.8 (b)) are characterized by the presence of weak N 1s lines located in the energy range of 395 - 415 eV. In this energy range, there are two components of the N 1s spectra, due to the existence of two different chemical bonds of nitrogen atoms with the surrounding atoms. The low-energy component of the XPS N 1s core- level spectra with binding energy of about 397.7 eV is caused by the formation of chemical N-Zn bonds arising from the substitution of oxygen atoms by nitrogen atoms in the nitrogen doped ZnO [135]. The appearance of the high-energy component of the XPS N 1s core-level spectra with binding energy of about 406.5 eV is generally attributed to arise from $(N_2)_O$, denoting a substitution of molecular N for O sublattice, which is considered as a double donor [136]. It is seen from Fig. 6.8 (b) that the intensity of 406.5 eV peak is equally stronger to that of 397.7 eV peak, indicating that a great amount N elements exists in the form of $(N_2)_O$ double donor defect in the N-doped ZnO film, which is favourable for gas sensing [137].

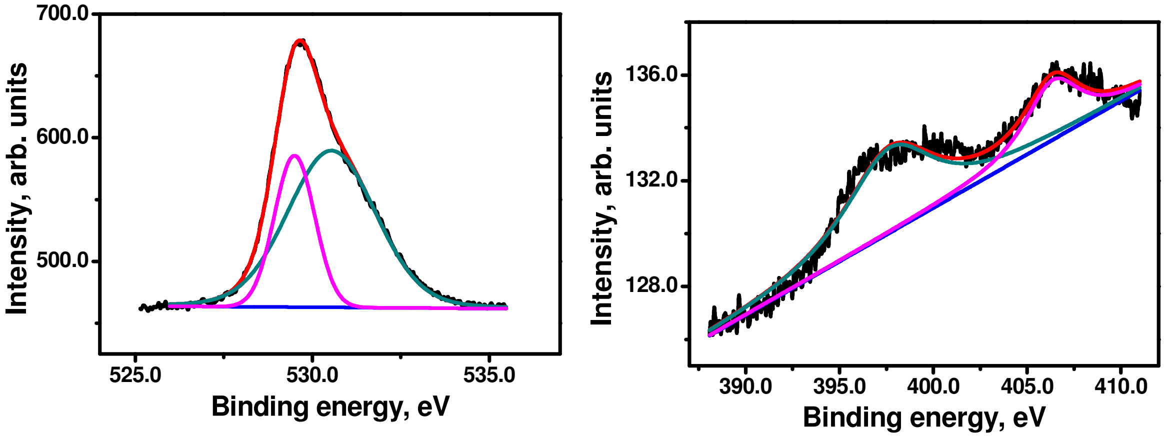

(a) (b)

Fig. 6.8. (a) XPS spectra of O 1s and (b) XPS spectra of nitride / nitrate.

CHAPTER 7: H_2S SENSING STUDIES ON DOPED ZNO FILMS

Hydrogen Sulfide is a toxic and flammable gas, usually generated in sewages, swamps, mines, etc. It is also used in laboratories, industries and in heavy water plants as a process gas for producing heavy water (D_2O). Hydrogen sulfide reacts strongly with living tissues and attacks the central nervous system. Its characteristic rotten-egg smell can be easily detected at low concentrations, but at higher concentrations, H_2S paralyzes the sense of smell. Table 7.1 lists the concentration levels of H_2S and the effects on human health. According to the Occupational Safety & Health Administration (OSHA, USA), the acceptable concentration

Table 7.1. H_2S Concentration levels and effects [138].

Concentration, ppm	**Symptoms / Effects**
0.00011 - 0.00033	Typical background concentrations.
0.01 1.5	Odor threshold (when rotten egg smell is first noticeable).
2 - 5	Prolonged exposure may cause nausea, tearing of the eyes, headache. Airway problems (bronchial constriction) in some asthma patients.
20	Headache, irritability, possible fatigue, loss of appetite, poor memory, dizziness.
50 - 100	Slight respiratory tract irritation after 1 hour exposure.
100	Eye irritation, coughing, loss of sense of smell after 2-15 minutes. Breathlessness, pain in the eyes, and drowsiness after 15-30 minutes followed by throat irritation after 1 hour. Several hours exposure may lead to death within the next 48 hours
200 - 300	Severe respiratory tract irritation after 1 hour of exposure. Possible pulmonary edema (fluid in the lungs).
500 - 700	Loss of consciousness and possibly death in 30 minutes to 1 hour.
700 - 1000	Immediate unconsciousness, loss of respiration, and death within 2 - 5 minutes.
1000 - 2000	Unconsciousness at once, loss of respiration and death in a few minutes. Death may occur even if individual is removed from the site at once and givenoxygen.

limit for exposure to H_2S is 10 ppm for an 8-hour period. Thus, it is imperative that the gas must be detected at ppm levels in air by selective and sensitive sensors, especially when it is encountered in the presence of other gases in a wide variety of industrial and environmental situations. This chapter elaborates the H_2S sensing studies carried out on the CZO, GZO and NZO based gas sensors.

7.1 Gas sensor parameters

The sensing mechanism of MOX gas sensors is based on change in conductivity when exposed to the analyte gas. Increase or decrease in conductance depends on the type of metal oxide (n or p) and the nature of test gas (reducing or oxidizing). Typical response curve showing the variation of conductance with time on exposure and withdrawal of analyte gas is shown in Fig. 7.1. Figure of merit of chemiresistive gas sensor is characterised by four important parameters – sensitivity, speed, selectivity and stability.

Sensitivity is a measure of change in conductivity when exposed to the target gas. It is expressed as the percentage change in conductance as per analyte concentration unit or as the ratio of resistance before and after exposure to analyte gas:

$$\text{Sensitivity (S)} = (|R_a - R_g| / R_a) * 100 \quad \text{or} \quad \text{Sensitivity} = R_a / R_g \qquad (7.1)$$

where, R_a and R_g are resistances in air and test gas, respectively.

Selectivity refers to the ability of the sensor to detect the test gas of interest in the presence of interfering gases, which may hamper the sensor response. It is usually expressed by:

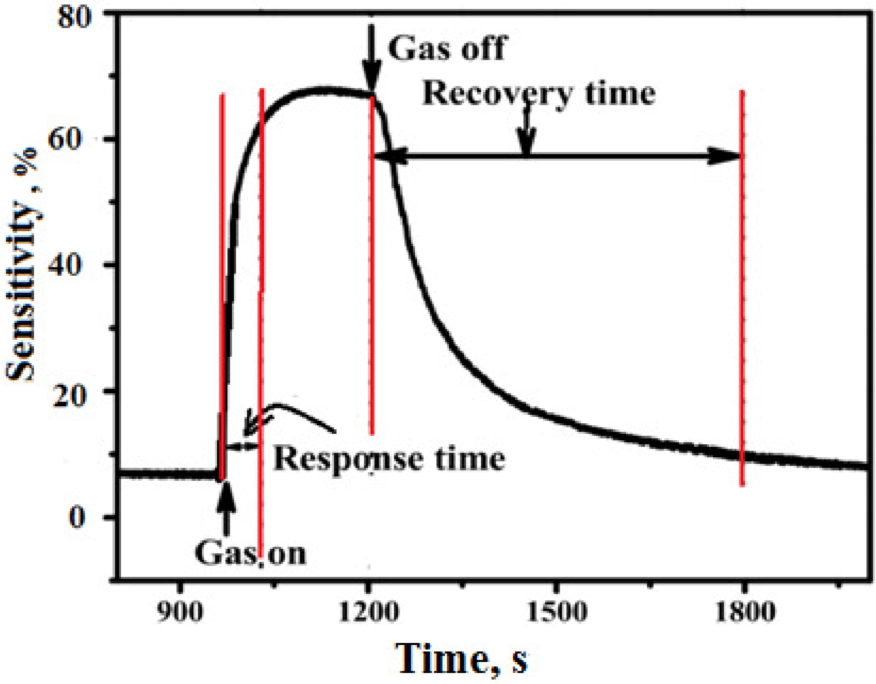

Fig. 7.1. Typical response curve of metal oxide gas sensor.

Selectivity = Sensitivity towards the desired gas / Sensitivity for interfering gas

Speed or Response time is the time required for sensor to reach 90% of the steady-state signal for a step concentration change from zero to a certain concentration value of analyte gas. Often 'speed' includes '*recovery time*' also, which is the time taken for the sensor signal to return to its initial value after the test gas is removed or the sensor is exposed to fresh air.

Stability refers to the degree to which the sensor baseline and response to a given environment drift with time. It is a measure of the ability to give reproducible results during the life time of a sensor. This includes maintaining the sensitivity, selectivity, response, and recovery time of the sensor within the tolerance limits.

7.2 Methods of measurement

The response of a metal oxide gas sensor is determined by measuring the resistance or conductance of the sensor with time in air and in the presence of a known amount of the analyte gas. Either one of the following two methods are used for the measurements.

7.2.1 Flow Through method

In this method (Fig. 7.2), the response of the sensor is recorded under a continuous flow of a known amount of test gas. Desired concentration of the test gas is achieved by mixing it with a carrier gas using MFCs. During recovery measurements, the MFC of analyte gas is switched off while the carrier gas continues to flow.

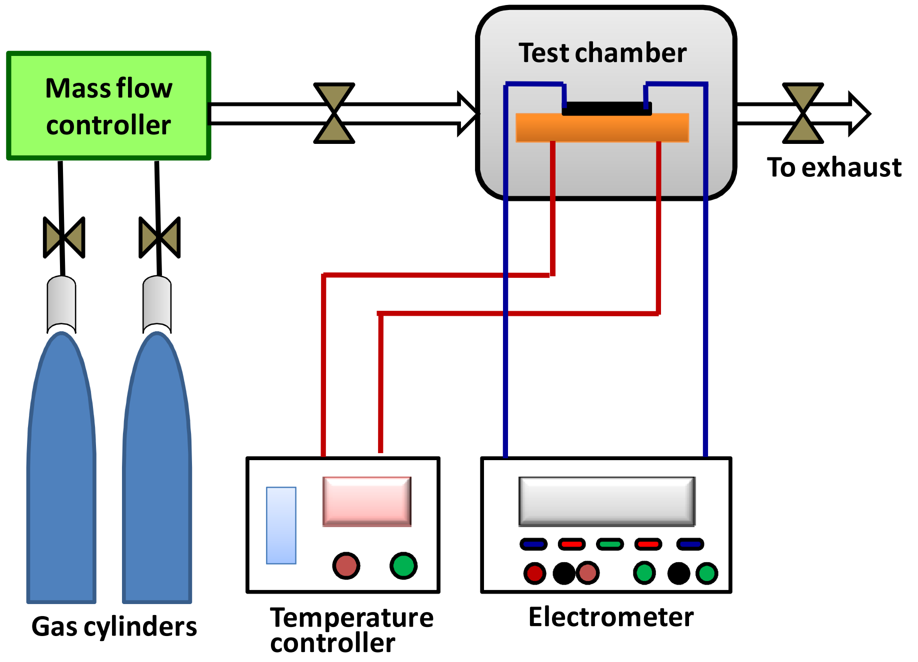

Fig. 7.2. Schematic of flow through method.

7.2.2 Static Environment method

Schematic of static environment method is shown in Fig. 7.3. The gas sensor is mounted in an airtight chamber of known volume. A known amount of analyte gas is injected into the housing using a syringe. The conductivity of the sensor as a function of time is measured till the steady state is achieved. The recovery of the sensor is studied by removing the sensor from housing and exposing to air.

In this project work, the gas sensing response characteristics i.e. change in conductance of the film with time were recorded as a function of temperature and gas concentration on exposure to different reducing gases (i.e. H_2S, CO, NH_3, H_2 and SO_2) in a static gas sensing setup as

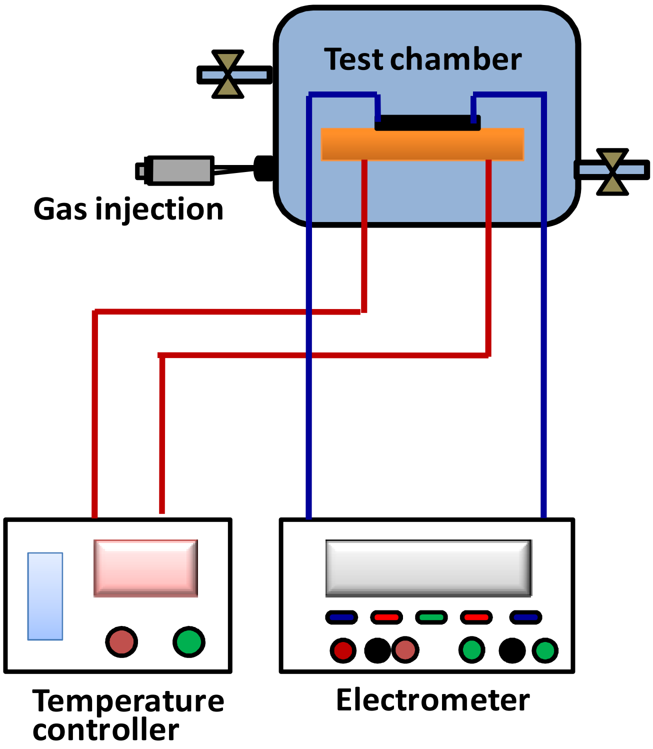

Fig. 7.3. Schematic of static environment method.

depicted in Fig. 7.4 (a). An SS test chamber was designed and fabricated for this purpose as shown in Fig. 7.4 (b). PC based measurement system was developed in virtual instrumentation platform for automated data acquisition. Gas sensors were fabricated by thermal evaporation of gold, forming interdigitated electrodes on the sputtered films, using a shadow mask (inset of Fig 7.4 (b)). The sensor was mounted on a heating stage fixed in the SS chamber (volume = ~ 1 litre). Heating stage temperature was precisely controlled by a PID programmer / controller. The sensor resistance was stabilized at each operating temperature for about 30 minutes prior to test gas exposure. All the gases were commercially procured locally. The gas canisters contained pressurized gas (20 - 40 kg/cm^2) at ~1000 ppm concentration. Using a gas tight syringe, measured quantity of gas was introduced in the chamber so as to yield the desired gas concentration. The response curves were measured by applying a fixed bias across the electrodes and recording time dependence of current using an electrometer or source - measure unit. After steady-state was achieved, recovery in response was studied by exposing the sensor to fresh air. From the response curves, the sensitivity (S) was calculated using the relation:

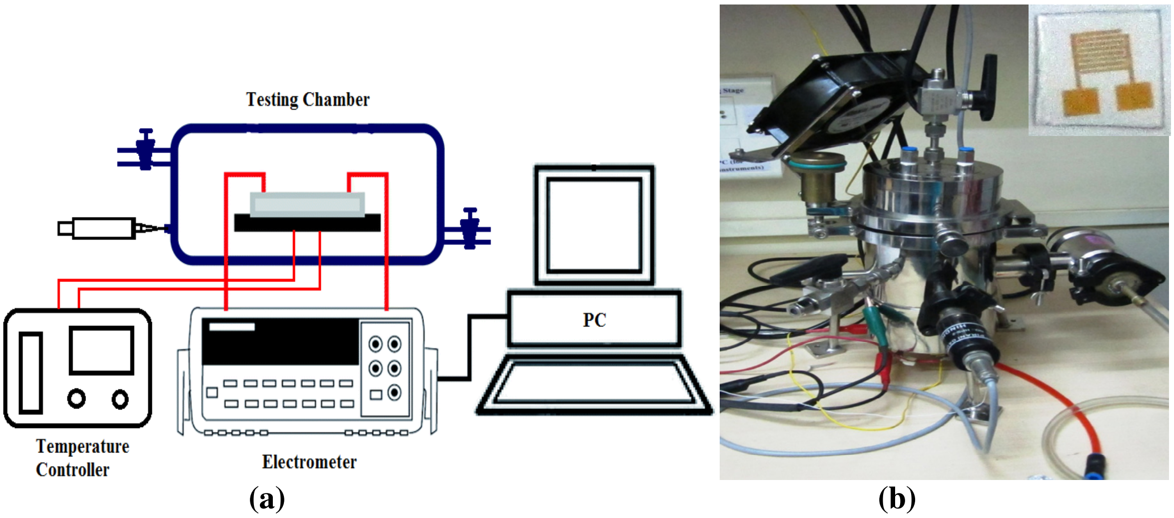

Fig. 7.4. (a) Schematic of gas sensing setup, (b) SS gas test chamber; inset shows the gas sensor with gold electrodes.

$$\text{Sensitivity (S)} = ((I_g - I_a) / I_a) * 100 \qquad (7.2)$$

where, I_a and I_g were the sensor current in air and test gas, respectively.

7.3 H_2S sensing studies of CZO films

Metal oxides used for gas sensing conduct by electrons and in general, the conduction electrons come from the non-stoichiometry due to excess metal ions in the metal oxide frame work. The deviation in stoichiometry results in shallow states made up of oxygen vacancies, which act as n-type donors. Atmospheric oxygen molecules are ionosorbed on metal oxide surface by capturing the conduction electrons and are held to the surface by electrostatic attraction. Depending on the operating temperature, they can exist as O_2^-, O^- or O^{2-}. Below 150°C, molecular oxygen adsorption is dominant in ZnO and it can be expressed as follows,

$$O_2 \text{ (atmosphere)} + e^- \text{ (ZnO surface)} \rightarrow O_2^- \text{ (ZnO surface)} \qquad (7.3)$$

At higher temperature (200 – 400 °C), the superoxide ion O_2^-dissociates to the peroxide form O^-, which is the most reactive species among O_2^-, O^- and O^{2-} [30, 139]. Above 400 °C, O^{2-} forms which is not very stable. The exposure of metal oxide surface to reducing gases such as CO, H_2, H_2S etc., leads to partial consumption of the adsorbed oxygen, resulting in a decrease in resistance, while the exposure to oxidizing agents (NO_2, O_2 etc.) increases the surface oxygen coverage and hence the resistance. Thus the extent of adsorbed oxygen is affected by the partial pressure of the reducing / oxidizing agents in surrounding atmosphere, which accordingly alters the surface conductivity [29, 140]. This change strongly depends on the chemical composition and grain size of interconnected particles of the metal oxide thin film.

In addition, the working temperature has a strong influence on the reaction rate of all surface processes as well as the interpenetration of the gas molecules into the porous sensing layer.

In order to determine the optimum operating temperature for the H_2S detection, a systematic investigation of temperature effects on gas sensing properties of CZO sensors is performed. Fig. 7.5 shows the plot of sensor response as a function of operating temperature towards 5 ppm of H_2S. Up to 100 °C, the sensor response is low for all samples, suggesting that the activation of H_2S reaction with adsorbed oxygen on the surface require slightly higher temperatures. While undoped ZnO does not show measurable response, all doped samples show better sensitivity above 100 °C. Among them, 2% CZO exhibits maximum sensitivity at 250 °C, suggesting that it is the optimum doping concentration [141].

Fig. 7.6 illustrates the typical response–recovery curve of the gas sensors to 5 and 10 ppm concentration of H_2S at 250 °C. It can be seen that the response increases rapidly and reaches its equilibrium. Once the source is removed, the response decreases quickly to the baseline. Again 2% CZO show the maximum sensitivity and fast response among all the sensors.

As described earlier, the adsorbed oxygen (O_2^-) dissociates to O^- ions at 250 °C. At this temperature, H_2S gas molecules get sufficiently high thermal energy to react with the O^- ions by the following reaction:

$$H_2S\ (g) + 2O^-_{ads} \rightarrow H_2\ (g) + SO_2\ (g) + 2e^- \tag{7.4}$$

This interaction between target gas and ionosorbed oxygen on ZnO surface re-injects the electrons into conduction band, which leads to increase in conductivity with reference to baseline. It is seen from Fig. 7.5 that the sensitivity tends to decrease beyond 250 °C. This

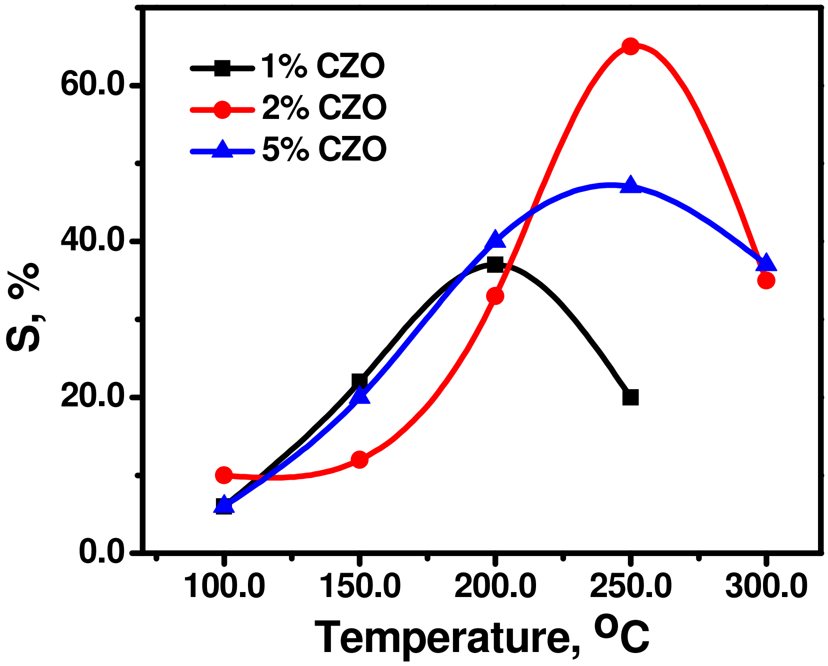

Fig. 7.5. CZO sensor response to 5 ppm H_2S as a function of temperature (■ – 1%, ● – 2% and ▲ – 5%).

can be attributed to the promotion of the reaction between H_2S and O_2 in air, which in turn reduces the gas flow diffusion towards the sensor surface [142].

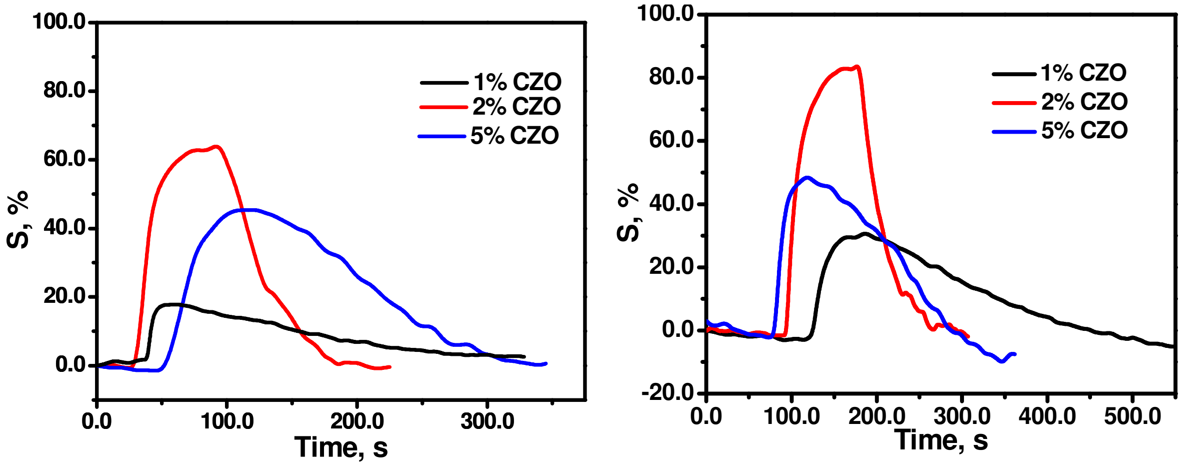

(a)

(b)

Fig. 7.6. Response and recovery characteristics of CZO sensors for (a) 5 ppm and (b) 10 ppm H_2S at 250°C.

The response and recovery characteristics of 2% CZO at 250 °C are shown in Fig. 7.7 for three different concentrations of H_2S. The response time is the time taken by the sensor to reach from 10% to 90% of the saturation value of the sensitivity after the surface has come in contact with the test gas. Similarly, recovery time is the time taken by the sensor to reach the initial value when re-exposed to ambient air at the operating temperature. As illustrated in Fig. 7.7, both response time and recovery time are of the order of few 10's of seconds for 2% CZO, suggesting that the sensors are very fast compared to most of the commercially available H_2S sensors.

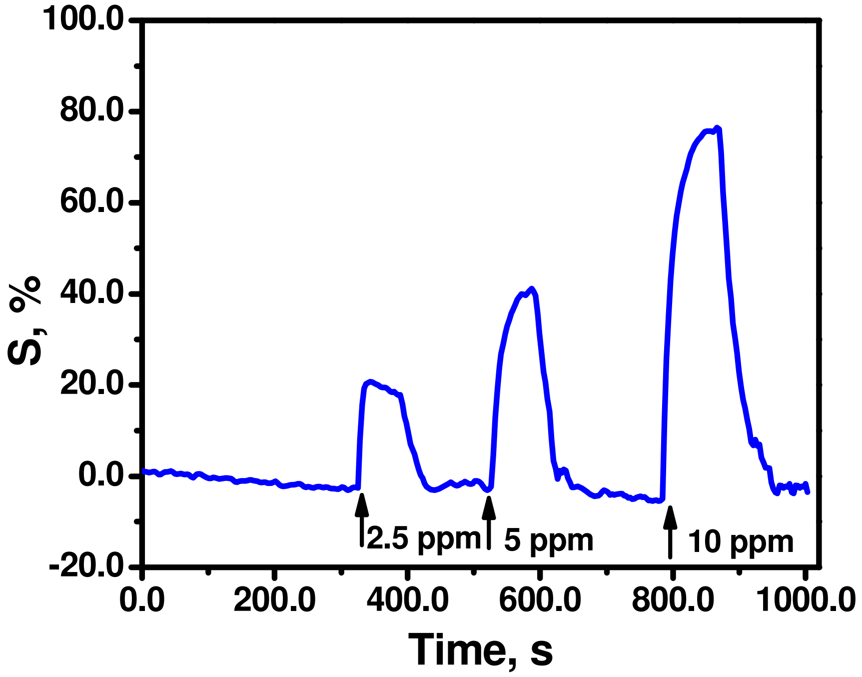

Fig. 7.7. Response of 2% CZO sensor at 250 °C for various concentrations of H_2S.

Selectivity is an important parameter for sensors to distinguish between different kinds of target gases. To determine the selectivity, cross response of CZO sensor is tested by exposing the sensor to various kinds of potentially interfering gases at an operating temperature of 250 °C. The results of successive injection of 10 ppm of CO, 10% H_2, 10 ppm of NH_3, 10 ppm of SO_2 and 2.5 ppm of H_2S are shown in Fig. 7.8. As can be seen from Fig. 7.8, the sensor shows miniscule response to other gases and a large response for H_2S, indicating excellent selectivity.

It has been reported that H_2S molecules dissociatively chemisorb on the surface of ZnO nanostructures as H and SH [143]. XRD results of CZO films confirmed the substitution of Cu into the ZnO lattice. Cu has higher attraction towards H_2S than Zn for the initial bridge-top (H–SH) configuration [144]. Thus, the high selectivity for H_2S could be attributed to the combined effect between Cu and H_2S in CZO nanostructures, which enhances the adsorption of H_2S molecules and facilitates reaction with oxygen species compared to undoped ZnO.

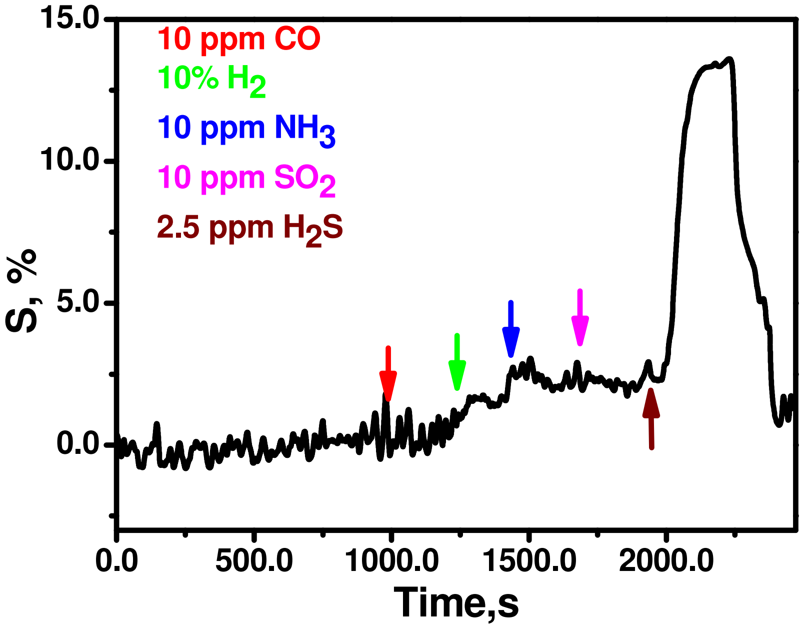

Fig. 7.8. Relative response of 2% CZO sensor for various reducing agents at 250°C. Arrow indicates the time of injection of test gas.

7.4 H_2S Gas sensing properties of GZO films

As discussed in the previous section, every analyte gas exhibits a specific temperature of maximum sensitivity which depends on its surface coverage and the conversion rate of ionosorbed oxygen. At this favourable temperature the relative cross sensitivity towards other gases is suppressed to its lowest level, thereby improving the selectivity for the target gas [16].

To evaluate the appropriate working temperature for GZO sensors, the H_2S sensing characteristics are studied as a function of temperature. Fig. 7.9 shows the plot of sensor response as a function of operating temperature towards 5 ppm of H_2S. It is evident that all the GZO films require above 200 ^{0}C working temperature for showing appreciable response. Also, the optimum working temperature is susceptible to doping concentration. It can be seen

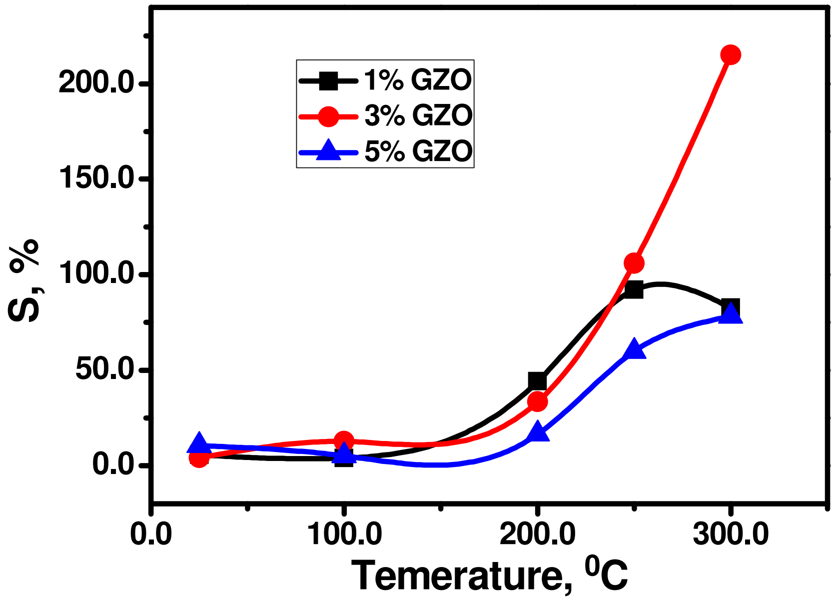

Fig. 7.9. GZO sensor response to 5 ppm H_2S as a function of temperature and doping concentration.

from Fig. 7.10 that 3% GZO exhibits maximum sensitivity at 300 °C, indicating that it is the optimum doping concentration [127,145]. Hence detailed investigations are carried out with 3% GZO films at an operating temperature of 300 °C.

Fig. 7.10 (a) illustrates the typical response–recovery curve of 3% GZO film as a function of H_2S concentration at 300 °C. It can be seen that the response increases rapidly and reaches its equilibrium. Once the source is removed, the response decreases quickly to the baseline. The estimated response time (T_{90}) and recovery time (T_{10}) are 50 s and 175 s respectively at 300 ºC. Inset in Fig. 7.10 (a) shows the linearity of response with the concentration of H_2S. A comparison of response plots for H_2S (at 1, 2, 3 and 5 ppm) from room temperature to 300 ºC is depicted in Fig. 7.10 (b). Up to 100 °C, the sensor response is low, suggesting that the activation of H_2S reaction with adsorbed oxygen on the surface require higher temperatures. In compliance with ionosorption model, 3% GZO shows better kinetics and sensitivity at 300 ºC. This can be attributed to the faster adsorption and desorption rates of oxygen at

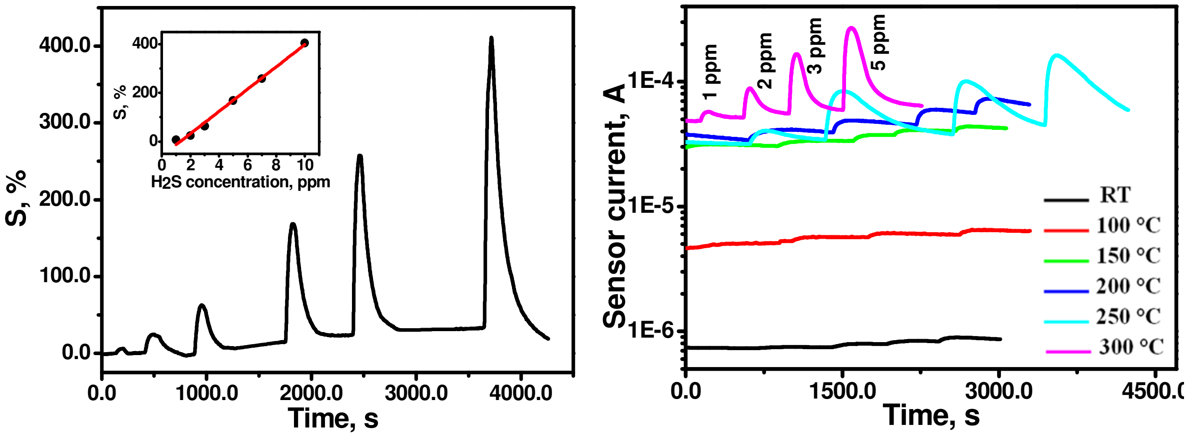

(a) (b)

Fig. 7.10. (a) Response of 3% GZO sensor at 300°C for various concentrations of H_2S; inset shows the linearity of sensor response with H_2S concentration; (b) Response and recovery characteristics of 3% GZO sensor for 1, 2, 3, and 5 ppm of H_2S as a function of temperature.

higher temperatures, resulting in a greater response (sensitivity) and a lower response time. However, the physical properties of the metal oxides place an upper limit on the temperatures that can be used. If the temperature is too high, the stability and reliability of the sensors deteriorates because of possible coalescence and structural changes [146]. In addition, as temperature increases, the charge carrier concentration increases and the Debye length, L_D, decreases, resulting in less sensitivity. In most cases, the optimum temperature for MOX gas sensors is between 200 °C and 500 °C [147].

Gas-sensing mechanism of ZnO-based sensors is surface sensitive, i.e. the conductivity is controlled by the analyte gas and the amount of chemisorbed oxygen on the surface. An increase in concentration of oxygen vacancies can improve the sensing properties. As described earlier, the adsorbed oxygen (O_2^-) dissociates to O^- ions at temperature > 200 °C. At this temperature, H_2S gas molecules get sufficiently high thermal energy to react with the O^- ions by the reaction (7.4). This interaction between target gas and ionosorbed oxygen on ZnO surface re-injects the electrons into conduction band, which leads to increase in conductivity with reference to baseline. Upon exposure to fresh air, adsorbed oxygen is restored and the baseline resistance is re-established. An additional chemical reaction can also take place simultaneously between the target gas and ZnO as given below:

$$\mathrm{ZnO\,(s) + H_2S\,(g) \rightarrow ZnS\,(s) + H_2O\,(g)} \tag{7.5}$$

However, conversion of ZnS to ZnO is a slow process and this reaction is marked by significant increase in recovery time. At intermediate concentrations of H_2S (< 20 ppm), reaction with adsorbed oxygen is dominant and the electrical conductivity is solely governed by potential barrier formed due to adsorbed oxygen [148]. Beyond 300 ºC, reaction between

H_2S and O_2 in air dominates, which in turn reduces the gas flow diffusion towards the sensor surface [149]. Hence the maximum operating temperature is restricted to 300 ºC in the present work. At this temperature the sensor shows excellent selectivity towards H_2S compared to other reducing gases like NH_3, CO, H_2 and SO_2 (Fig. 7.11).

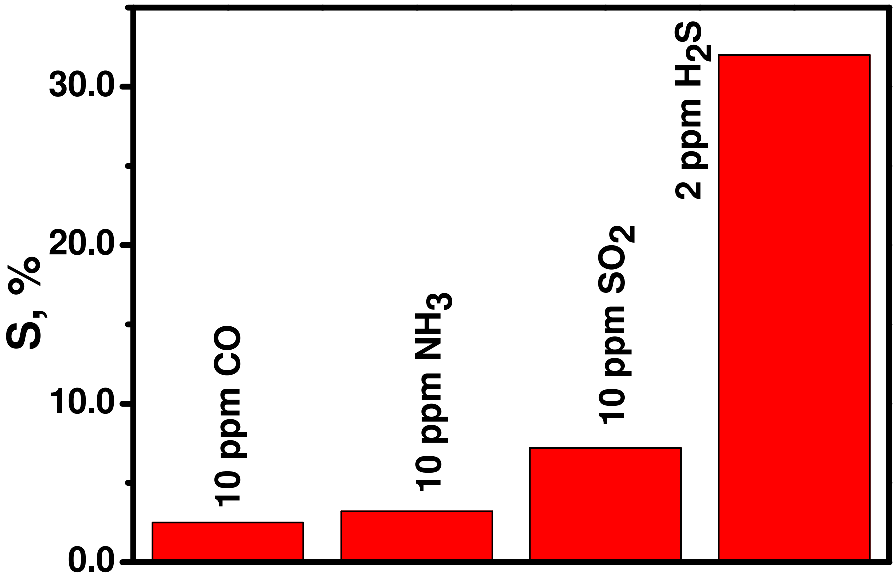

Fig. 7.11. Relative response of 3% GZO sensor for various reducing agents at 300 °C.

From the above discussion it is evident that the overall surface stoichiometry has a significant influence on the surface conductivity of metal oxide sensors, which in turn determines the gas sensing performance. In case of GZO, the replacement of the Zn^{2+} cation by the Ga^{3+}, which acts as donor, leads to the formation of active adsorption sites (Ga atoms and oxygen vacancies) and favor the adsorption of oxygen species [145]. Sharma *et al.* have studied the adsorption kinetics of H_2S on undoped and doped graphene [150]. They concluded that while H_2S molecules weakly bind to pure graphene with small adsorption values, Gallium doped graphene shows large adsorption energies and binding distances typical for the chemisorptions. Similarly, in the case of GZO, Ga^{3+}cations are more favourable for H_2S dissociation than Zn^{2+} cations on the surface sites [151]. Thus, the enhanced sensitivity of GZO for H_2S could be attributed to the combined effect of excess oxygen vacancies due to Ga^{3+} substitution and the large adsorption energy of Ga for H_2S.

7.5 H_2S Gas sensing properties of NZO films

Fig. 7.12 shows the dynamic response – recovery characteristics of the NZO gas sensor at various concentrations of H_2S at 300 °C. This optimum temperature is arrived at by systematic investigation of H_2S sensitivity of NZO films as a function of operating temperature. It is evident from Fig. 7.12 that the response of the sensor increases linearly with increase in H_2S concentration. When exposed to fresh air, the response quickly drops to the base line, indicating the reversibility and reproducibility of sensor.

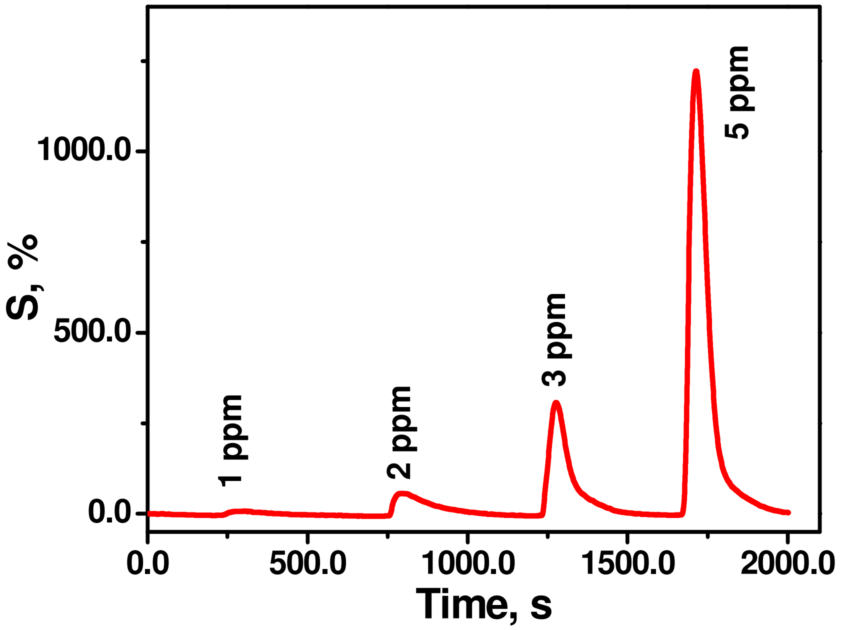

Fig. 7.12. Response of NZO sensor at 300°C for various concentrations of H_2S.

Selectivity is one of the most important parameter for sensors to distinguish between various kinds of potentially interfering gases. Fig. 7.13 shows the results of exposure to 5ppm of NH_3, 5 ppm of CO, 5 ppm of SO_2, 0.1% H_2, and 5 ppm of H_2S at an operating temperature of 300 °C. As seen in Fig. 7.13, the NZO shows miniscule response to gases other than H_2S, indicating excellent selectivity.

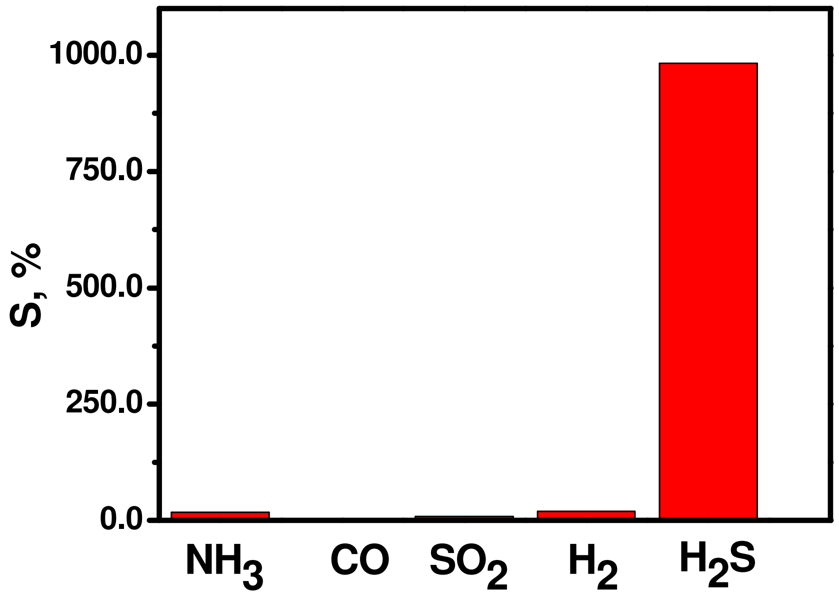

Fig. 7.13. Relative response of NZO sensor for various reducing agents at 300°C.

It is known that nitrogen can substitute the oxygen sites of ZnO in two forms: atomic nitrogen on oxygen sites (N_O) acting as acceptors and molecular nitrogen on oxygen sites $(N_2)_O$ acting as donors. As the formation enthalpy of $(N_2)_O$ is lower than (N_O), it is hypothesized that the molecular nitrogen in NZO leads to additional donor defects [134]. Kouser *et al.* have reported that the adsorption of H_2S on pristine 2D-ZnO is weak due to the Vander Waals interaction [152]. They observed that the H_2S molecule prefers to occupy the site at the center of the hexagonal ring with the H atoms pointing towards the oxygen atoms of the substrate. However, substitutional nitrogen doping in 2D-ZnO leads to a drastic increase in the adsorption energy (E_A = -152 kJ mol^{-1}) resulting in effective dissociation of H_2S molecules. This is attributed to the strong covalent bonding interaction between an unpaired electron in the p-orbital of nitrogen and an electron in the s-orbital of H. Hence, it is hypothesized that the excess donor defects and the large adsorption energy could be responsible for the high sensitivity of NZO for H_2S.

7.6 Discussion on H_2S sensing properties of doped ZnO films

The fundamental sensing mechanism of MOX gas sensors is based on the deviation of equilibrium of surface chemisorbed oxygen due to the reaction with target gas. This sensing mechanism is mainly described by two popular models - ionosorption model and oxygen-vacancy model. The first model considers the space charge effects or the changes in the electric surface potential resulting from the gas adsorption, ionization and redox reactions [29]. The ionosportion model is widely accepted even though spectroscopic evidence for negatively charged oxygen species are not studied well. The second model is based on the reaction between oxygen vacancies and gas molecules and the variation of the amount of the sub-surface / surface oxygen vacancies and their reduction – re-oxidation mechanism which leads to changes in the oxygen stoichiometry. The oxygen-vacancy model is not discussed as widely as the ionosorption model even though this model predicts the same changes in electrical conductivity.

Based on the ionosorption model, the probable sensing mechanism of ZnO sensor is pictorially depicted in Fig. 7.14. When the temperature of the sensing film reaches the operation temperature, the surface is quickly filled with chemisorbed oxygen atoms due to the ionization of oxygen adatoms (i.e. electron trapping). This results in the widening of depletion layer (for n-type semiconductors) thereby increasing the surface potential. Thus, a potential barrier is formed between adjacent grains, which hinders the migration of electrons form one grain to another. On exposure to H_2S, the oxygen species are consumed, leading to a decrease in potential barrier height, facilitating the electron transport between grains. As discussed earlier, the MOX sensor performance is strongly influenced by the morphological structure which is determined by the synthesis procedure and addition of foreign elements. In the present study, RF sputtering yielded nanostructured ZnO films, resulting in large surface to volume ratio. In addition, the dopants (Cu, Ga and N) increased the number of oxygen vacancies and provided large adsorption energy to H_2S. Thus, all the films showed high sensitivity and selectivity to H_2S. Table 7.2 shows the comparison of sensor characteristics of all the doped ZnO films for an exposure of 5 ppm H_2S at the optimum operating temperature. It is seen from the table that, though 2% CZO has the lowest sensitivity, it has better kinetics as well as the lowest operating temperature. Both GZO and NZO showed high

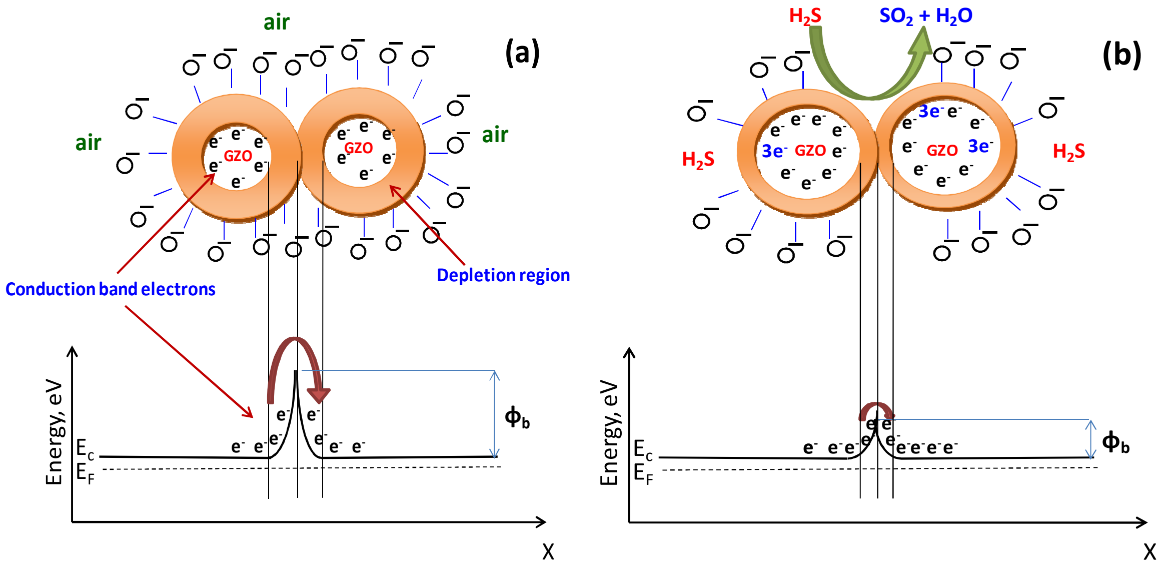

(a) (b)

Fig. 7.14. Structural and energy band models of H_2S sensing mechanism when exposed to (a) air and (b) H_2S.

sensitivity though their recovery time was of the order of few hundred seconds. It was observed that while CZO and GZO films were stable even after one year (under ambient conditions) with < 20% reduction in sensitivity, NZO films showed ~30% reduction in sensitivity after about eight months. Thus, among the three doped systems GZO is preferable due to the optimum sensor performance with better stability.

Table 7.2. Comparison of sensor characteristics of CZO, GZO and NZO films for 5 ppm H_2S.

Material	% doping	Sensitivity, %	Response time, s	Recovery time, s	Operating temperature, °C
CZO	2	70	20	50	250
GZO	3	200	50	175	300
NZO	1:4 (N_2:Ar)	1200	30	200	300

CHAPTER 8: CONCLUSIONS AND FUTURE WORK

8.1 Summary and conclusions

The motivation behind this thesis work was to develop microelectronics devices and highly selective metal oxide materials using CMOS compatible post processing methods for realizing microelectronic devices based H_2S sensors. Extensive literature survey on the current status of solid state gas sensors, specifically MOX sensors and the role of MEMS technology on the gas sensing applications were carried out. ZnO was chosen for further studies as it is one of the most promising gas sensor materials owing to its easy synthesis procedure, good electrical properties and in particular its compatibility with Si leading to MEMS based chemical sensors. MUMPs was adapted for the design and fabrication of the MEMS structures. Based on this process, the following MEMS structures were chosen for the design and simulation studies.

(i) Microhotplates with different membrane size and embedded heater
(ii) Microcantilever of various shapes, sizes with or without heater and piezo resistor

The layouts and the FEM analysis were carried out using commercial software available for MEMS systems.

Various heater structures viz., serpentine, spiral, fan and S - shape MHPs were designed to heat membranes of different sizes. Electro-thermal simulations were carried out to optimize the heater design by spatially varying the heater current density to achieve uniform temperature distribution over the sensing area. Spiral type heater was found to the best choice as far the power consumption and temperature homogeneity was concerned. Analytical calculations showed that the heat loss through conduction in the membrane is <10% of the total power supplied.

Microcantilevers of various shapes and sizes were designed based on MUMPs process. Some of the cantilevers were designed with embedded heater or both embedded heater and piezo resistor. FEM simulations showed that the deflection sensitivity increased linearly with applied load, as long as ($\Delta z \ll l$). Electro-thermal analysis showed good temperature uniformity on the microcantilever surface. Thermo-mechanical analysis indicated that as the applied load increased, the displacement tended to become non-linear with temperature for all the cantilevers. Piezo resistive simulations showed that the percentage change in current increased linearly with the deflection of the cantilever.

Based on the simulation results, layouts for six mask levels were carried out. The complete design was submitted to foundry, where the microstructures were fabricated and diced. Optical microscopy, SEM and WLI measurements verified that the geometries matched very well with the designed X-Y-Z dimensions for all the microstructures. In order to carry out the electrical characterization and thermal imaging, some of the (300 µm × 300 µm) MHP chips were packaged and wirebonded on a PCB. From electro-thermal characterisation, TCR of the polysilicon was determined as ~2.6×10^{-3} / °C. Thermal efficiency of the microhotplates was experimentally estimated as ~10 ºC / mW. It was observed that the temperature of MHP increased linearly with applied heater power. Thermal imaging by IR camera showed that complete MHP was heated uniformly. Other than the suspended MHP, the remaining substrate stayed nearly at room temperature, resulting in localised heating at low heater power.

Magnetron sputtering technique was adopted for the synthesis of sensing layers and thermal evaporation method for the deposition of contact electrodes. For this purpose, installation of customized two target magnetron system and thermal evaporation system was carried out. RF sputtering process was optimized for the deposition of ZnO thin films using sintered and powder targets. XRD studies showed a single peak corresponding to (002) orientation for all the films. AFM measurements confirmed that the films were homogeneous with good connectivity between the adjacent particles.

With the optimized parameters, Cu, Ga and N doped ZnO films were synthesized using powder targets at various doping concentration and characterized for structural and morphological properties. XRD patterns showed that all the films were polycrystalline with a hexagonal wurtzite crystal structure, having preferential orientation along c-axis. AFM showed fully coalesced, uniformly distributed ZnO grains that showed columnar growth perpendicular to the substrate**.** XPS measurements demonstrated the existence of +2 oxidation valence state of Cu in CZO films and +3 in case of GZO films. In case of NZO, formation of N-Zn bonds due to the substitution of oxygen atoms by nitrogen atoms as well as substitution of molecular N for O sublattice that acted as double donor were observed. In all doped films an enhancement in the number of oxygen vacancies was evident from the O 1s spectra.

Gas sensors were fabricated by depositing interdigitated gold electrodes on the sputtered films. Gas sensing studies on CZO, GZO and NZO films were carried out in a home-made automated setup as a function of temperature and gas concentration. Among the Cu doped films, 2% CZO gave the highest sensitivity for H_2S at an operating temperature of 250 °C. In case of GZO, 3% GZO exhibited the highest sensitivity for H_2S at an operating temperature of 300 °C. NZO film grown with 1:4 ratio of N_2 : Ar showed the highest sensitivity at 300 °C among all the doped systems. All the sensors showed high selectivity to H_2S with fast response and recovery characteristics. This was mainly attributed to the large surface to volume ratio of the nanocrystalline films. In addition, the dopants (Cu, Ga and N) increased the number of oxygen vacancies and provided large adsorption energy to H_2S. It was observed that among the three doped systems, GZO was preferred due to the optimum sensor performance with better stability.

Summary of the important results of this thesis work is given below:

(i) Design, simulation and fabrication of microhotplates (MHP) and microcantilever were carried out based on cost effective MetalMUMPs process flow. Structural and optical characterizations confirmed that the fabricated devices were as per the designed geometries.

(ii) IR thermal imaging of the MHP confirmed the temperature homogeneity of the suspended membrane and the thermal efficiency was estimated as ~ 10 °C / mW. A temperature of 450 °C was obtained at ~45 mW power (heater voltage = 10 V and heater current = 4.6 mA).

(iii) Deposition of highly oriented, nanocrystalline films of Cu, Ga and N_2 doped ZnO (CZO, GZO and NZO respectively) could be achieved by RF magnetron sputtering technique using powder targets.

(iv) All three doped systems showed high sensitivity and selectivity towards H_2S, which could be attributed to the increased the number of oxygen vacancies and the large adsorption energy of the dopant atoms to H_2S.

(v) Among the doped systems, NZO showed the highest sensitivity to H_2S (three orders of conductance change for 10 ppm H_2S at 300°C) and GZO showed the optimum sensor performance with better stability (< 20% reduction in sensitivity after about a year).

8.2 Future work

This thesis opens up following future work:

(i) Only preliminary studies on gas sensing performance were carried out by depositing SnO_2 thin film (without any mask or patterning) on the MHP. The sensors could not be tested at higher temperature (above 100 °C) due to the interference of heater supply. To further assess the sensor performance, suitable pattering method could be adapted to deposit ZnO sensing layer only on IDE and systematic studies could be carried out.

(ii) Among the systems studied, NZO films gave the highest sensitivity and selectivity. In order to improve the stability of this system, further optimization of gas composition, post annealing, co-doping, etc., could be carried out.

(iii) To understand the microscopic gas sensing mechanism and the role of dopants in ZnO based systems, in-depth studies using advanced measurement techniques such as reflectance mode FTIR, in-situ Raman etc. could be carried out.

(iv) As on date, SnO_2 based systems dominate the commercial market of MOX gas sensors. However, lack of selectivity and inferior recovery of SnO_2 based sensors still remain as challenging issues. ZnO based systems explored in this research work offer high selectivity and excellent recovery for H_2S. Hence these systems can be further evaluated for long term stability, life time, detection range etc. and assessed for the possibility of commercialization.

(v) Low power microhotplates (<40 mW for 450°C) with excellent temperature homogeneity could be realized during this thesis work. Hence a complete, portable gas sensing system consisting of MEMS based H_2S sensor (ZnO sensing layer on IDE of MHP) and an integrated interface (including read-out electronics and closed loop temperature control circuit) could be realized on the same chip.

(vi) The present research can be further extended to study the effect of other suitable dopants, surface morphology, grain size reduction, etc., on the gas sensing properties of ZnO based systems. These studies may further lead to an integrated MEMS based gas sensor array, associated with pattern recognition techniques, to achieve high selectivity even at ppb concentrations, which otherwise is not possible with discrete gas sensors.

References

1. K. Arshak, E. Moore, G.M. Lyons, J. Harris and S. Clifford, A review of gas sensors employed in electronic nose applications, Sensor Review, 24 (2004) 181.

2. D.-D. Lee and D.-S. Lee, Environmental gas sensors, IEEE Sensors J., 1(2001) 214.

3. N. Yamazoe and K. Shimanoe, New perspectives of gas sensor technology, Sens. Actuators, B, 138 (2009) 100.

4. C. Di Natalea, R. Paolesseb, E. Martinellia, and R. Capuanoa, Solid-state gas sensors for breath analysis: A review, Anal. Chim. Acta, 824 (2014) 1.

5. G. Eranna, Metal oxide nanostructures as gas sensing devices, CRC Press, Taylor & Francis Group, 2012

6. S. Capone, A. Forleo, L. Francioso, R. Rella, P. Siciliano, J. Spadavecchia, D. S. Presicce and A.M. Taurino, Solid state gas sensors: State of the art and future activities, J. Optoelectron. Adv. Mater., 5 (2003) 1335.

7. X. Liu, S. Cheng, H. Liu, Sha Hu, D. Zhang and H. Ning, A Survey on Gas Sensing Technology, Sensors, 12 (2012) 9635.

8. P. Grundler, Chemical Sensors: An Introduction for Scientists and Engineers, Springer, Berlin, 2007

9. G. Korotcenkov and B.K. Cho, Chemical sensor selection and application guide, Vol.6, G. Korotcenkov (ed), Chemical sensors: comprehensive sensor technologies, Momentum Press, New York, 2011.

10. S. Fanget, S. Hentz, P. Puget, J. Arcamone, M. Matheron, E. Colinet, P. Andreucci, L. Duraffourg, M. Ed and M.L. Roukes, Gas sensors based on gravimetric detection—a review, Sens Actuators B, 160 (2011) 804.

11. P. Bunyan, C. Baker and N. Rurner, Application of heat conduction calorimetry to high explosives, Thermochim. Acta, 401 (2003) 9.

12. F. Baldini, A.N. Chester, J. Homola, S. Martellucci (eds), Optical chemical sensors, Springer, Dordrecht, 2006.

13. J.R. Stetter, G. Korotcenkov, X. Zeng, Y. Tang and Y. Liu, Electrochemical gas sensors: fundamentals, fabrication and parameters, Vol.3, G. Korotcenkov (ed), Chemical sensors: comprehensive sensor technologies, Momentum Press, New York, 2011.

14. A. Gurlo, N. Bârsan, U. Weimar, Gas sensors based on semiconductiong metal oxides, J.L.G. Fierro (ed), Metal Oxides: Chemistry and Applications, CRC Press, Boca Raton, FL, USA, 2006

15. N. Barsan, D. Koziej and U. Weimar, Metal oxide-based gas sensor research: How to, Sens. Acutators B, 121 (2007) 18.

16. G. Eranna, B.C. Joshi, D.P. Runthala and R.P. Gupta, Oxide materials for development of integrated gas sensors—A comprehensive review, Critical Reviews in Solid State and Materials Sciences, 29:3 (2004) 111.

17. T. Seiyama, A. Kato, K. Fujushi and M. Nagatani, A new detector for gaseous components using semiconductive thin films, Anal. Chem.,34 (1962) 1502.

18. N. Taguchi, Japenese Patents 45-38200 and 47-38840; US Patent 3 644 795.

19. Hyo-Joong Kim and Jong-Heun Lee, Highly sensitive and selective gas sensors using p-type oxide semiconductors: Overview, Sens. Actuators B 192 (2014) 607.

20. H. Ogawa, M. Nishikawa and A. Abe, Hall measurement studies and an electrical conduction model of tin oxide ultrafine particle films, J. Appl. Phys., 53 (1982) 4448.

21. G. Korotcenkov, Gas response control through structural and chemical modification of metal oxide films: State of the art and approaches, Sens. Actuators B, 107 (2005) 209.

22. M.R. Mahmood, T. Soga, M.H. Mamat, Z. Khusaimi, A.M. Nor, A Review on zinc oxide nanostructures: Doping and gas sensing, Adv. Mater. Res., 667(2013) 329.

23. A. Tricoli, M. Righettoni, S.E. Pratsinis, Minimal cross-sensitivity to humidity during ethanol detection by SnO_2-TiO_2 solid solutions, Nanotechnology, 20 (2009) 315502.

24. A. Hoel, L.F. Reyes, S. Saukko, P. Heszler, V.Lantto and C.G. Granqvist, Gas sensing with films of nanocrystalline WO_3 and Pd made by advanced reactive gas deposition, Sens. Actuators B, 105 (2005) 283.

25. Il-Doo Kim, A. Rothschild and H.L. Tuller, Advances and new directions in gas-sensing devices, Acta Materialia, 61 (2013) 974.

26. G. Neri, First fifty years of chemoresistive gas ensors, Chemosensors, 3 (2015) 1.

27. A. Cabot, J. Arbiol, J.R. Morante, U. Weimar, N. Barsan and W. Gopel, Analysis of the noble metal catalytic additives introduced by impregnation of as obtained SnO_2 sol-gel nanocrystals for gas sensors, Sens. Actuators B, 70 (2000) 87.

28. K. Arshak, E. Moore, G.M. Lyons, J. Harris and S. Clifford, A review of gas sensors employed in electronic nose applications, Sensor Review, 24 (2004) 181.

29. M.J. Madou, S.R. Morrison, Chemical Sensing with Solid State Devices, Academic Press, London, 1989.

30. H. Chon and J. Pajares, Hall effect studies of oxygen chemisorption on zinc oxide, J. Catal., 14 (1969) 257.

31. S. Roy and C.K. Sarkar, MEMS and nanotechnology for gas sensors, CRC Press, Taylor & Francis Group, FL, USA, 2016.

32. R.E. Cavicchi, J.S. Suehle, K.G. Kreider, M. Gaitan and P. Chaparala, Optimized temperature-pulse sequences for the enhancement of chemically specific patterns from micro-hotplate gas sensors, Sens. Actuators, B, 33 (1996) 142.

33. M. Li, W. Yan, H. Zhu, Z. Guoa and Z. Tanga, Fabrication and characterization of a low power consumption ethanol gas sensor based on a suspended micro-hotplate, RSC Adv., 5 (2015) 51953.

34. B. Jayaraman, V.R. Singh, A. Asundi, N. Bhat and G.M Hegde, Thermo-mechanical characterization of surface-micromachined microheaters using in-line digital holography, Meas. Sci. Technol., 21 (2010) 015301.

35. J.H. Zhao, S.J. Yu, K. Li, Y. Dong, Q. Zhou and Z. You, A Micro-resonant gas sensor with nanometer clearance between the pole plates, Sensors, 18 (2018) 362.

36. M. Afridi, A. Hefner, D. Berning, C. Ellenwood, A. Varma, B. Jacob and S. Semancik, MEMS - based embedded sensor virtual components for system-on-a-chip (SoC), Solid-State Electron., 48 (2004) 1777.

37. J.G. Korvink and O. Paul, MEMS: a practical guide to design, analysis and applications, William Andrew Publishing, 2006.

38. A. Cowen, R. Mahadevan, S. Johnson and B. Hardy, MetalMUMPs Design Handbook, MEMSCAP, (2002 – 2012).

39. Figaro Products Catalogue, Figaro gas sensors 2000-series.

40. I. Simon, N. Barsan and M. Bauer, Micromachined metal oxide gas sensors: opportunities to improve sensor performance, Sens. Actuators B, 73 (2001) 1.

41. W.J. Hwang, K.S. Shin, J.H. Roh, D.S. Lee, and S.H. Choa, Development of micro-heaters with optimized temperature compensation design for gas sensors, Sensors, 11 (2011) 2580.

42. J.O. Dennis, A. Yousif and M.N. Mohamad, Design, simulation and modeling of a micromachined high temperature microhotplate for application in trace gas detection, Int. J. Engg. & Tech., 10 (2010) 67.

43. V.K. Khanna, M. Prasad, V.K. Dwivedi, Chandra Shekar, A.C. Pankaj and J. Basu, Design and electro-thermal simulation of a polysilicon microheater on a suspended membrane for use in gas sensing, Indian J. Pure & Appl. Phys., 45 (2007) 332.

44. S. Semancik, R.E. Cavicchi, M.C. Wheeler, J.E. Tiffany, G.E. Poirier, R.M. Walton, J.S. Suehle, B. Panchapakesan and D.L. DeVoe, Microhotplate platforms for chemical sensor research, Sens. Actuators B, 77 (2001) 579.

45. S. M. Sze, Physics of Semiconductor Devices, John Wiley and Sons, 1981.

46. D. Briand, Micromachined Semiconductor Gas Sensors, R. Jaaniso and O.K. Tan (eds), Semiconductor Gas Sensors, Woodhead Publishing Limited, 2013.

47. M.Y. Afridi, J.S. Suehle, M.E. Zaghloul, D.W. Berning, A.R. Hefner, R.E. Cavicchi and C.J. Taylor, A monolithic CMOS microhotplate based gas sensor system, IEEE Sensors J., 2 (2002) 644.

48. P. Bhattacharyya, Technological journey towards reliable microheater development for MEMS gas sensors: A review, IEEE Trans. Device and Mater. Reliab., 14 (2014) 589.

49. G. Korotcenkov and B.K. Cho, Engineering approaches to improvement of conductometric gassensor parameters. Part 2: Decrease of dissipated (consumable) power and improvement stability and reliability, Sen.Actuators B, 198 (2014) 316.

50. M. Baroncini, P. Placidi, G.C. Cardinali and A. Scorzoni, Thermal characterization of a microheater for micromachined gas sensors, Sens.Actuators A, 115 (2004) 8.

51. F. Samaeifar, H. Hajghassem, A. Afifi and H. Abdollahi, Implementation of high-performance MEMS platinum micro-hotplate, Sensor Review, 35 (2015) 116.

52. F.M. Battiston, J.-P. Ramseyer, H.P. Lang, M.K. Baller, Ch. Gerber, J.K. Gimzewski, E. Meyer and H.-J. Gu Èntherodt, A chemical sensor based on a microfabricated cantilever array with simultaneous resonance-frequency and bending readout, Sens.Actuators B, 77 (2001) 122.

53. N.V. Lavrik, M.J. Sepaniak, and P.G. Datskos, Cantilever transducers as a platform for chemical and biological sensors , Rev. Sci. Instrum., 75 (2004) 2229.

54. C. Ziegler, Cantilever-based biosensors, Anal. Bioanal. Chem., 379 (2004) 946.

55. X. Li and D-.W. Lee, Integrated microcantilevers for high-resolution sensing and probing, Meas. Sci. Technol., 23 (2012) 022001.

56. E. Finot, A. Passian and T. Thundat, Measurement of mechanical properties of cantilever shaped materials, Sensors, 8 (2008) 3497.

57. P.A. Rasmussen, A.V. Grigorov and A.J. Boisen, Double sided surface stress cantilever sensor, Micromech. Microeng., 15 (2005) 1088.

58. P. Lu, H.P. Lee, C. Lu, and S.J. O'Shea, Surface stress effects on the resonance properties of cantilever sensors, Phys. ReV. B, 72 (2005) 085405.

59. H. Ibach, The Role Surface Stress in Reconstruction, Epitaxial Growth and Stabilization of Mesoscopic Structures, Surf. Sci. Rep., 29 (1997) 193.

60. W. Haiss, Quantitative surface stress measurements on Au (111) electrodes by scanning tunneling microscopy, Langmuir, 12 (1996) 4311.

61. E.P.M. Leiva, M.G. Del Popolo, and W. Schmickler, Changes in surface stress caused by the adsorption of an epitaxial metal monolayer, Chem. Phys. Lett., 320 (2000) 392.

62. K.M. Goeders, J.S. Colton, and L.A. Bottomley, Microcantilevers: Sensing chemical interactions via mechanical motion, Chem. Rev., 108 (2008) 522.

63. N. Lobontiu, Dynamics of microelectromechanical systems, Springer Science, 2007.

64. A.W. McFarland, M.A. Poggi, L.A. Bottomley and J.S. Colton, Injection moulding of high aspect ratio micron-scale thickness polymeric microcantilevers, Nanotechnology, 15 (2004) 1628.

65. G.G. Stoney, Tension of metallic films deposited by electrolysis, Proc. Royal Soc. London, 82 (1909) 172.

66. M.Z. Ansari and C. Cho, A Study on Increasing sensitivity of rectangular microcantilevers used in biosensors, Sensors, 8 (2008) 7530.

67. J.E. Sader, Surface stress induced deflections of cantilever plates with applications to the atomic force microscope: Rectangular plates, J. Appl. Phys., 89 (2001) 2911.

68. X.L. Feng, R.R. He, P.D. Yang and M.L. Roukes, Very high frequency silicon nanowire electromechanical resonators, Nano Lett., 7 (2007) 1953.

69. A. Boisen, S. Dohn, S.S. Keller, S. Schmid and M. Tenje, Cantilever-like micromechanical sensors, Rep. Prog. Phys., 74 (2011) 036101.

70. F. Lochon, I. Dufour and D. Rebiére, An alternative solution to improve sensitivity of resonant microcantilever chemical sensors: comparison between using high-order modes and reducing dimensions, Sens. Actuators B, 108 (2005) 979.

71. B. Ilic, D. Czaplewski, M. Zalalutdinov, H.G. Craighead, P. Neuzil, C. Campagnolo and C. Batt, Single cell detection with micromechanical oscillators, J. Vac. Sci. Technol., B19 (2001) 2825.

72. G. Y. Chen, T. Thundat, E.A. Wachter, and R.J. Warmack, Adsorption-induced surface stress and its effects on resonance frequency of microcantilevers, Journal of Applied Physics, 77 (1995) 3618.

73. A.W. McFarland, M.A. Poggi, M.J. Doyle, L.A. Bottomley and J.S. Colton, Influence of surface stress on the resonance behavior of microcantilevers, Appl. Phys. Lett., 87 (2005) 053505.

74. M. Chaudhary and A. Gupta, Microcantilever-based Sensors, Defence Science Journal, 59 (2009) 634.

75. Z. Long, L. Kou, M.J. Sepaniak and X. Hou, Recent advances in gas phase microcantilever based sensing, Rev. Anal. Chem., 32 (2013) 135.

76. A.S. Sarathi Vasan, D.M. Mahadeo, R.I. Doraiswami, Y. Huang and M. Pecht, Point-of-care biosensor system, Front. Biosci., 5 (2013) 39.

77. T. Ono, X. Li, H. Miyashita and M. Esashi, Mass sensing of adsorbed molecules in sub-picogram sample with ultrathin silicon resonator, Rev. Sci. Instrum., 74 (2003) 1240.

78. X. Li and D.W. Lee, Integrated microcantilevers for high-resolution sensing and probing, Meas. Sci. Technol., 23 (2012) 022001.

79. C. Pang, Z. Zhao, L. Shi**,** L. Du and Z. Fang**,** An excellent platinum piezoresistive pressure sensor using adhesive bonding with SU-8, Adv.Mater. Res., 60-61 (2009) 68.

80. S. Beeby, G. Ensell, M. Kraft and N. White (eds), MEMS mechanical sensors, Artech House, Inc., MA, USA, 2004**.**

81. M. Napoli, B. Bamieh and K. Turner, A capacitive microcantilever: Modeling, validation, and estimation using current measurements, J. Dyn. Syst. Meas. Contr., 126 (2004) 319.

82. L. Almeida, R. Ramadoss, R. Jackson, K. Ishikawa and Q. Yu, Study of the electrical contact resistance of multi-contact MEMS relays fabricated using the MetalMUMPs process, J. Micromech. Microeng., 16 (2006) 1189.

83. R.I. Shakoor, S.A. Bazazb, M. Burniec, Y. Laic and M.M. Hasan, Electrothermally actuated resonant rate gyroscope fabricated using the MetalMUMPs, Microelectronics Journal, 42 (2011) 585.

84. L. Li and D. Uttamchandani, Monolithic RF MEMS inductor using silicon MEMS foundry process, Micro and Nano Lett., 1 (2006) 5.

85. I. Zine-El-Abidine and M. Okoniewski, A tunable radio frequency MEMS inductor using MetalMUMPs, J. Micromech. Microeng., 17 (2007) 2280.

86. M. Bakri-Kassem and R. R. Mansour, Two movable-plate nitride-loaded MEMS variable capacitor, IEEE Trans. Microwave Theory Tech., 52 (2004) 831.

87. M. Esashi, Revolution of Sensors in Micro-Electromechanical Systems, Jap. J. Appl. Phys., 51 (2012) 080001.

88. P.C. Chan, G. Yan, L. Sheng, R.K. Sharma, Z. Tang, J.K. Sin, I-Ming Hsing and Y. Wang, An integrated gas sensor technology using surface micro-machining, Sens. Actuators B, 82 (2002) 277.

89. S. Sharma and M. Madou, A new approach to gas sensing with nanotechnology, Phil. Trans. R. Soc. A, 370 (2012) 2448.

90. M. Graf, D. Barrettino, K. Kirstein and A. Hierlemann, CMOS microhotplate sensor system for operating temperatures up to 500 °C, Sens. Actuators B, 117 (2006) 346.

91. J. Puigcorbe, D Vogel, B. Michel, A. Vila, I. Gracia, C. Cane and J.R. Morante, Thermal and mechanical analysis of micromachined gas sensors, J. Micromech. Microeng. 13 (2003) 548.

92. R. Inglés, J. Pallares, I. Gràcia, A. Marié Gué and J.L. Ramírez, Electrothermal simulations to improve heater design in preconcentration membranes, Therminic Proc., 2010.

93. Q. Zhu, Microcantilever sensors in biological and chemical detections, Sens. and Transducers, 125 (2011) 1.

94. R. Nuryadi, Modeling of I-, T- and V-shaped microcantilevers for environmental monitoring, Mater. Sci. Forum, 737 (2013) 119.

95. J. Lee, T. Beechem, T.L. Wright, B.A. Nelson, S.Graham, and W.P. King, Electrical, thermal, and mechanical characterization of silicon microcantilever heaters, J. Microelectromech. Syst., 15 (2006) 1644.

96. S.U. Jen, C.C. Yu, C.H. Liu, and G.Y. Lee, Piezoresistance and electrical resistivity of Pd, Au, and Cu films, Thin Solid Films, 434 (2003) 316.

97. Y. Kanda, Piezoresistance effect of silicon, Sens.Actuators, A: Physical, 28 (1991) 83.

98. A. Loui, F.T. Goericke, T.V. Ratto, J. Lee, B.R. Hart and W.P. King, The effect of piezoresistive microcantilever geometry on cantilever sensitivity during surface stress chemical sensing, Sens. Actuators A, 147 (2008) 516.

99. E. Lawrence, Optical measurement techniques for dynamic characterization of MEMS devices, Polytec Inc., 2012.

100. C. Gong, Characterization of the digital micromirror devices, IEEE Trans. Electron Devices, 61 (2014) 4210.

101. L.L.R. Rao, M.K. Singha, K.M. Subramaniam, N. Jampana and S. Asokan, Molybdenum microheaters for MEMS-based gas sensor applications: fabrication, Electro-Thermo- Mechanical Response Characterization, IEEE Sens. J., 17 (2016) 22.

102. B.H. Weiller, P.D. Fuqua and J.V. Osborn, Fabrication, characterization, and thermal failure analysis of a micro hot plate chemical sensor substrate, J. Electrochem. Soc. 151 (2004) H59.

103. K. Wasa, M. Kitabatake and H. Adachi, Thin film materials technology - Sputtering of compound materials, William Andrew Inc., 2004.

104. P.T. Moseley and B.C. Tofield (eds), Solid state gas sensor, Adam Hilger, Bristol and Philedelphia, 1987.

105. K.B. Sundaram and A. Khan, Characterization and optimization of zinc oxide films by r.f. magnetron sputtering, Thin Solid Films 295 (1997) 87.

106. D.A. Skoog, F.J. Holler, S.R. Crouch, Principles of Instrumental Analysis, Thomson Brooks, Cole, 2007.

107. G. Korotcenkov, The role of morphology and crystallographic structure of metal oxides in response of conductometric-type gas sensors, Mater. Sci. Eng., R 61 (2008) 1.

108. Evaporation Sources & Heating Methods, Technical notes, Kurt J. Lesker Company.

109. R. Kumar, G. Kumar, O. Al-Dossary and A. Umar, ZnO nanostructured thin films: Depositions, properties and applications—A review, Mater. Express, 5 (2015) 3.

110. P. Bhattacharyya, P.K. Basu, B. Mondal and H. Saha, A low power MEMS gas sensor based on nanocrystalline ZnO thin films for sensing methane, Microelectron. Reliab., 48 (2008) 1772.

111. M. Willander, O. Nur, Q.X. Zhao, L.L. Yang, M. Lorenz and B.Q. Cao, Zinc oxide nanorod based photonic devices: recent progress in growth, light emitting diodes and lasers, Nanotechnology, 20 (2009) 332001.

112. D.T. Phan and G.S. Chung, Effects of different morphologies of ZnO films on hydrogen sensing properties, J. Electroceramics, 32 (2014) 353.

113. H. Gong, J.Q. Hu, J.H. Wang, C.H. Ong and F.R. Zhu, Nano-crystalline Cu-doped ZnO thin film gas sensor for CO, Sens. Actuators B: Chem., 115 (2006) 247.

114. H.S. Kim, E.S. Jung, W.J. Lee, J.H. Kim, S.O. Ryu and S.Y. Choi, Effects of oxygen concentration on the electrical properties of ZnO films, Ceram. Int., 34 (2009) 1097.

115. H. Nanto, T. Minami and S. Takata, Zinc-oxide thin film ammonia gas sensor with high sensitivity and excellent selectivity, J. Appl. Phys., 60 (1986) 482.

116. G.K. Mani and J. Rayappan, Facile synthesis of ZnO nanostructures by spray pyrolysis technique and its application as highly selective H_2S sensor, Materials Letters, 158 (2015) 373.

117. Z. Banu Bahşi and A. Yavuz Ora, Effects of Mn and Cu doping on the microstructures and optical properties of sol–gel derived ZnO thin films, Opt. Mater., 29 (2007) 672.

118. Y.S. Sonawane, K.G. Kanade, B.B. Kale, R.C. Aiyer, Electrical and gas sensing properties of self-aligned copper-doped zinc oxide nanoparticles, Mater. Res. Bull., 43 (2008) 2719.

119. L. Ma, S. Ma, H. Chen, X. Ai and X. Huang, Microstructures and optical properties of Cu-doped ZnO films prepared by radio frequency reactive magnetron sputtering, Appl. Surf. Sci., 257 (2011) 10036.

120. O. Lupan, T. Pauporté, B. Viana and P. Aschehoug, Electrodeposition of Cu-doped ZnO nanowire arrays and heterojunction formation with p-GaN for color tunable light emitting diode applications, Electro chim. Acta., 56 (2011) 10543.

121. D. Chakraborti, J. Narayan and J.T. Prater, Room temperature ferromagnetism in Zn1-xCuxO thin films, Appl. Phys. Lett., 90 (2007) 062504.

122. Z. Xu, G. Duan, Y. Li, G. Liu, H. Zhang, Z. Dai and W. Cai, CuO–ZnO Micro/Nanoporous Array-Film-Based Chemosensors: New Sensing Properties to H_2S, Chem. Eur. J., 20 (2014) 6040.

123. B. Behera and S. Chandra, Synthesis and characterization of ZnO nanowires and ZnO-CuO nanoflakes from sputter-deposited brass (Cu0.65-Zn0.35) film and their application in gas sensing, J. Mat. Sci. & Tech., 31 (2015) 1069.

124. D. Das and P. Mondal, Low temperature grown ZnO:Ga films with predominant c-axis orientation in wurtzite structure demonstrating high conductance, transmittance and photoluminescence, RSC Adv., 6 (2016) 6144.

125. Sheng-Joue Young, Chih-Chiang Yang, and Lin-Tzu Lai,Growth of Al-, Ga-, and In-doped ZnO nanostructures via a low-temperature process and their application to field emission devices and ultraviolet photosensors, J. Electrochem. Soc., 164 (2017) B3013.

126. M. Hjiri, R. Dhahri, L. El Mir, A. Bonavita, N. Donato, S.G. Leonardi and G. Neri, CO sensing properties of Ga-doped ZnO prepared by sol–gel route, J. Alloys Compd., 634 (2015) 187.

127. Y. Hou and A.H. Jayatissa, Low resistive gallium doped nanocrystalline zinc oxide for gas sensor application via sol–gel process, Sens. Actuators B, 204 (2014) 310.

128. T. Zhao, Y. Fu, Y.Zhao, L. Xing and X. Xue, Ga-doped ZnO nanowire nanogenerator as self-powered/active humidity sensor with high sensitivity and fast response, J. Alloys. Compd., 648 (2015) 571.

129. L. Gong, Y.-Z. Liu, F,-Y. Liu and L.-X. Jiang, Room-temperature deposition of flexible transparent conductive Ga-doped ZnO thin films by magnetron sputtering on polymer substrate, J. Mater. Sci. - Mater. Electron., 28 (2017) 6093.

130. G.C. Park, S.M. Hwang, J.H. Choi, Y. H. Kwon, H.K. Cho, S.-W. Kim, J.H. Lim and J. Joo, Effects of In or Ga doping on the growth behavior and optical properties of ZnO nanorods fabricated by hydrothermal process, Phys. Status Solidi A, 210 (2013) 1552.

131. M. Laurenti, S. Stassi, M. Lorenzoni, M. Fontana, G. Canavese, V. Cauda and C.F. Pirri, Evaluation of the piezoelectric properties and voltage generation of flexible Zinc Oxide thin films, Nanotechnology, 26 (2015) 215704.

132. Ali Khorsand Zak, Nur Suhaili Abd Aziz, Abdul Manaf Hashim and Frouzan Kordi, XPS and UV–vis studies of Ga-doped zinc oxide nanoparticles synthesized by gelatin based sol-gel approach, Ceram. Int., 42 (2016) 13605.

133. L. Liu, J. Xu, D.Wang, M. Jiang, S. Wang, B. Li, Z. Zhang, D. Zhao, C-X Shan, B. Yao and D. Z. Shen, p-Type conductivity in N-doped ZnO: the role of the N(Zn)-V(O) complex, Phys. Rev. Lett., 108 (2012) 215501.

134. J. Karamdel, C.F. Dee and B. Y. Majlis, Characterization and aging effect study of nitrogen-doped ZnO nanofilm, Appl. Surf. Sci., 256 (2010) 6164.

135. A. Ievtushenko, O. Khyzhun, I. Shtepliuk, V. Tkach, V. Lazorenko and G. Lashkarev X-Ray Photoelectron Spectroscopy Study of Nitrogen and Aluminum_Nitrogen Doped ZnO Films, Acta Physica Polancia, 124 (2013) 858.

136. L. Wang, B. Lin, L. Zhou, Y.X. Shang, G.N. Panin and D. Fu, Nitrogen-doped ZnO nanorods prepared by hydrothermal diffusion, Mater. Lett., 85 (2012) 171.

137. Z.W. Wang, Y. Yue and Y. Cao, Influence of annealing temperature on properties of nitrogen-doped zinc oxide films deposited by magnetron sputtering, Superlattices Microstruct., 65 (2014) 7.

138. https://www.osha.gov/SLTC/hydrogensulfide/standards.html

139. T. Lin, X. Lv, S. Li and Q. Wang, The Morphologies of the Semiconductor Oxides and Their Gas-Sensing Properties, Sensors, 17 (2017) 2779.

140. C. Wang, L. Yin, L. Zhang, D. Xiang and R. Gao, Metal Oxide Gas Sensors: Sensitivity and Influencing Factors, Sensors, 10 (2010) 2088.

141. L. Chow, O. Lupan, G. Chai, H. Khallaf, L.K. Ono, B. Roldan Cuenya, I.M. Tiginyanu, V.V. Ursaki, V. Sontea and A. Schulte, Synthesis and characterization of Cu-doped ZnO one dimensional structures for miniaturized sensor applications with faster response, Sens. Actuators A, 189 (2013) 399.

142. P.S. Shewale, V.B. Patil, S.W. Shin, J.H. Kim and M.D. Uplane, H_2S gas sensing properties of nanocrystalline Cu-doped ZnO thin films prepared by advanced spray pyrolysis, Sens. Actuators B, 186 (2013) 226.

143. K.J. Iversen and M.J.S. Spencer, Effect of ZnO Nanostructure Morphology on the Sensing of H_2S Gas, J. Phys. Chem. C, 117 (2013) 26106.

144. Y. Fu, Y. Zhao, P. Wang, L. Xing and X. Xue, High response and selectivity of a Cu–ZnO nanowire nanogenerator as a self-powered / active H_2S sensor, Phys. Chem. Chem. Phys., 17 (2015) 2121.

145. R. Dhahri , M. Hjiri, L.El. Mir, A. Bonavita, D. Iannazzo, S.G. Leonardi and G. Neri, CO sensing properties under UV radiation of Ga-doped ZnOnanopowders, Appl. Surf. Sci., 355 (2015) 1321.

146. N. H. Al-Hardan, M. J. Abdullah, A. Abdul Aziz, H. Ahmad and L.Y. Low, ZnO thin films for VOC sensing applications, Vacuum, 85 (2010) 101.

147. S. Capone, A. Forleo, L. Francioso, R. Rella, P. Siciliano, J. Spadavecchia, D.S. Presicce and A.M. Taurino, Solid state gas sensors: state of the art and future activities, J. Optoelect. Adv. Mater., 5 (2003) 1335.

148. M. Kaur, S. Kailasaganapathi, N. Ramgir, N. Datta, Sushil Kumar, A.K. Debnath, D.K. Aswal and S.K. Gupta, Gas dependent sensing mechanism in ZnO nanobelt sensor, Appl. Surf. Sci., 394 (2017) 258.

149. Z. Liu, T. Fan, D. Zhang, X. Gong and J. Xu, Hierarchically porous ZnO with high sensitivity and selectivity to H_2S derived from biotemplates, Sens. Actuat. B 136 (2009) 499.

150. S. Sharma and A.S. Verma, A theoretical study of H_2S adsorption on graphene doped with B, Al and Ga, Physica B, 427 (2013) 12.

151. C.-H. Chung, S.I. Yi and W.H. Weinberg, Dissociative and selective adsorption of H_2S on the GaAs (001)-(4×2) surface, Appl. Phys. Lett, 69 (1996) 3369.

152. S. Kouser, U.V. Waghmare and N. Tit, Adsorption and splitting of H_2S on 2D-$ZnO_{1-x}N_y$: first-principles analysis, Phys. Chem. Chem. Phys., 16 (2014) 10719.